UiO : Department of Mathematics
University of Oslo

Measurement of Wave Properties with a Custom Built Sensor System as Part of the One Ocean Expedition (2021-2023)

Technical Aspects and Post Processing of Field Data

Fabian Knoblauch

Master's Thesis, Spring 2022

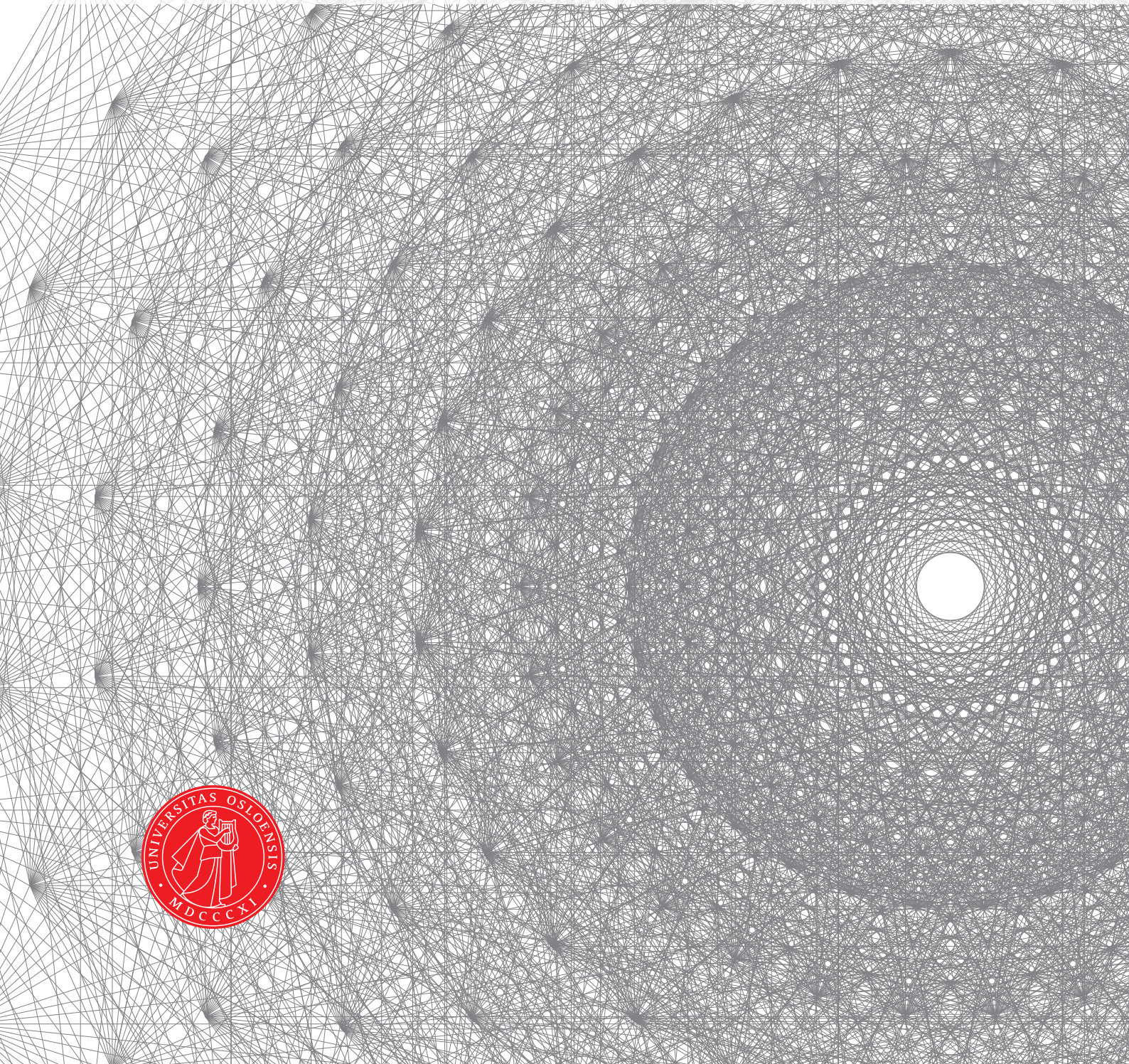

This master's thesis is submitted under the master's programme *M.Sc. Fluid Mechanics*, with programme option *Energy, Environment and Safety*, at the Department of Mathematics, University of Oslo. The scope of the thesis is 60 credits.

Acknowledgements

First and foremost, I would like to thank my supervisors Atle Jensen and Jean Rabault, for their continuous help and support during this project, and for the realisation of the project in the first place.

I would also like to thank Lars R. Hole for the creation of this project as a part of the One Ocean Expedition.

Huge thanks also to Patrik Bohlinger for providing the model and satellite data used in this thesis.

Thanks to Olav Gundersen for providing help with the construction of parts and letting me use the department's workshop.

Last but not least, I would like to thank the Statsraad Lehmkuhl and its crew, for the help with mounting the sensor system and for the voyage in general.

Abstract

In-situ measurement data of ocean waves is important for the validation and tuning of several types of numerical models. A recent inexpensive alternative to the widely used buoy measurements is given by a wave sensor system based on an altimeter and an inertial measurement unit (IMU). This project's goal is to determine the applicability of such a system on a ship, not designed for research purposes, in order to investigate if such a system is suited for wide usage. The aim is to prove that such a system combines low cost in production with practicality and reliability, while delivering quality wave data. Therefore, a custom wave sensor system is designed, built and installed on board the Statsraad Lehmkuhl as part of the One Ocean Expedition. The measured raw data is post processed to receive the water surface elevation as a time series. Resulting wave properties are compared to model and satellite data. Further, the influence of the Doppler Effect on the measured data is investigated. The results show, that an altimeter and IMU based wave sensor system is capable of reliably measuring wave data. Imprecise motion measurement leads to bias for higher waves. The ship's hull may falsify the measurements, depending on the probes location and the angle of the incoming waves. The Doppler Effect has a significant effect on the measured wave spectra, but a correction can be applied easily, if the ship's velocity and the angle of the incoming waves to midships are known. These results suggest, that wave sensor systems based on altimeters and IMUs pose a widely applicable possibility for open ocean wave measurements. Challenges, which are faced in further development of the system, are the concrete positioning of the altimeters and IMUs, as well as the availability of the ship's speed and the angle of the incoming waves for the Doppler Effect correction.

Contents

List of Figures

List of Tables

CHAPTER 1

Introduction

Ocean waves, more precisely wind generated surface gravity waves, are a major factor in marine engineering. Many forces acting on marine structures are wave induced (Newman, 2018). Furthermore, ocean waves also have a significant impact on meteorological dependencies and are therefore included in forecasting models. (Christensen et al., 2013; ECMWF, 2016). Therefore an increased demand for ocean wave measurement data is given, especially for model validation (Christensen et al., 2013).

Wave measurements in the open ocean are currently mainly realised by the usage of earth observation satellites and drifting buoys. The number of satellites measuring wave data is limited and satellite development and production is highly expensive. Buoys are a cheaper alternative, but they have either a rather limited lifetime as drifters, or are only able to gather local data as stationary buoys.
Therefore, the idea of a cheap and robust wave sensor system, which could be mounted on most types of ships, was formed by Christensen et al. (2013). The system developed by Christensen et al. (2013) used an ultrasonic altimeter to measure the distance to the water surface and an inertial measurement unit to correct for the motion of the ultrasonic probe itself. The system was tested by Christensen et al. (2013) in three measurement campaigns during which it performed well. It was furthermore used by Løken et al. (2021) for surface wave measurements in the Arctic region. During the campaigns undertaken by Christensen et al. (2013), the ship was halted and orientated with the bow facing the incoming waves. Data sets of up to a day in length were measured. During the campaign undertaken by Løken et al. (2021), the waves were measured continuously for two weeks, also when the ship was at speed. The ship used for the second campaign had a stabilising system to minimise the ship's motion (J. Rabault, personal communication, April 2022).

The project discussed in this thesis is a wave sensor system, similar to the one used by Christensen et al. (2013), which is installed in the bow of the Statsraad Lehmkuhl as part of the One Ocean Expedition. The One Ocean Expedition is a 20 month long research expedition, which is part of the UN Decade of Ocean Science for Sustainable Development (One-Ocean-Expedition-website, 2022). Due to the emphasis on sustainability, a sailing ship was chosen as the research vessel. This is the 98 m long Norwegian Barque Statsraad Lehmkuhl. The sailing route is planned as a circumnavigation, to cover a vast range of different areas of interest for ocean research around the globe. Instruments of several Norwegian Universities and Institutes are installed on the Statsraad Lehmkuhl, related mainly to meteorological, oceanographic and biological interests.
The idea of the wave sensor project on board the Statsraad Lehmkuhl is, to pursue the initial idea by Christensen et al. (2013), of a cheap and robust wave measurement system, which can be mounted on most types of ships. It's purpose is to measure the water surface elevation as a time series, from which the wave spectra and the wave heights can be gained. In contrast to the previous campaigns by Christensen et al. (2013) and Løken et al. (2021), where similar systems were used on research ships for short campaigns, the novelty of this project is the installation of the wave sensor system on a ship, which has not been designed for research purposes. The altimeter probes and inertial measurement units (IMUs) can therefore not be placed in their ideal positions, but their mounting locations are adapted to the ship's design. Also the system developed for this project is demanded to be reliable, to operate for over 20 months and to withstand harsh weather conditions. Furthermore, the system cannot interfere with the sailing or maintenance work done aboard the ship. Also, during the long operational duration, the system will operate under situations with a way larger motion of the ship's hull, then in any of the previous campaigns.

The questions that shall be viewed upon are about the realisability of the installation and operation of a wave sensor system on board the Statsraad Lehmkuhl, about the reliability and durability of the system in various sailing conditions, about the practical aspects of the post processing of the collected data especially regarding the raised complexity based on the ship type, about the quality of the measured wave properties, about the usability of the data and about possible improvements or corrections.
The thesis presents the design of the system (chapter 2), the data acquisition (chapter 3), the post processing (chapter 4), and the important aspects of the resulting data (chapter 5) in great detail, to serve as an instruction and foundation for further steps, to enable the installation of cheap and durable wave sensor systems on various ship types. The investigation for possible shortcomings of the system (chapter 6) shall give the possibility for improvement and further development of the system.

CHAPTER 2

The System

2.1 The Overall Setup

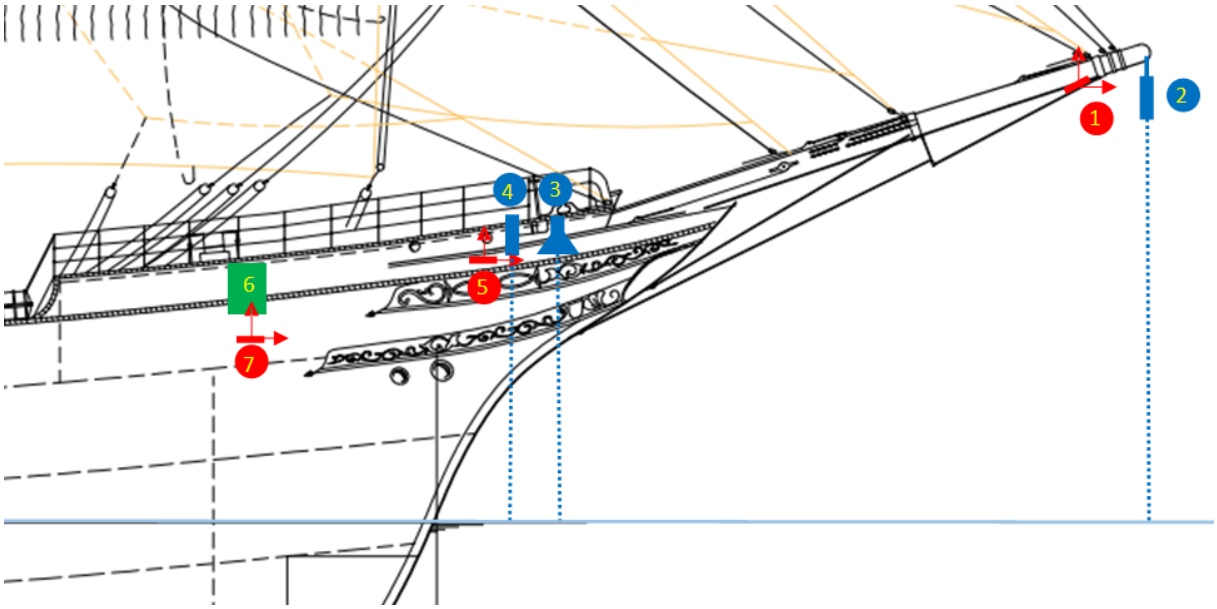

Figure 2.1: Locations of the system's components: (1) additional IMU at the bowsprit (extra IMU 1), (2) ultrasonic probe at the bowsprit (ultrasonic gauge 1), (3) radar probe at the starboard side of the bow, (4) ultrasonic probe at the starboard side of the bow (ultrasonic gauge 2), (5) additional IMU at the starboard side of the bow (extra IMU 0), (6) processing unit including the Raspberry Pi and the Arduino Board, (7) main IMU VN100 at the processing unit (IMU).

The wave measurement system described, was developed and built by Jean Rabault from the Meteorological Institute of Norway. Its purpose is to measure the punctual water surface elevation η as a time series. The processing unit of the system is composed of a Raspberry Pi 4 personal computer, running the scripts and saving the resulting data, and an Arduino Due board, used to evaluate the analogue output signals of the sensors.
To measure the elevation of the water surface, three altimeters are used. Two are based on ultrasound, while the third one operates by radar waves. The radar probe and one of the ultrasound probes are mounted on the starboard side of the bow, while the third probe is mounted on the tip of the bowsprit (see figure 2.1). To later compensate the measurements for the motion of the ship, that varies the position of the probes relative to the water surface, three inertial measurement units (IMUs) are used to measure the ship's acceleration as a time series. The main IMU of the system is a VN100 by VectorNav and located in the casing for the Raspberry Pi and the Arduino board. The other two IMUs are placed near the altimeters (see figure 2.1).

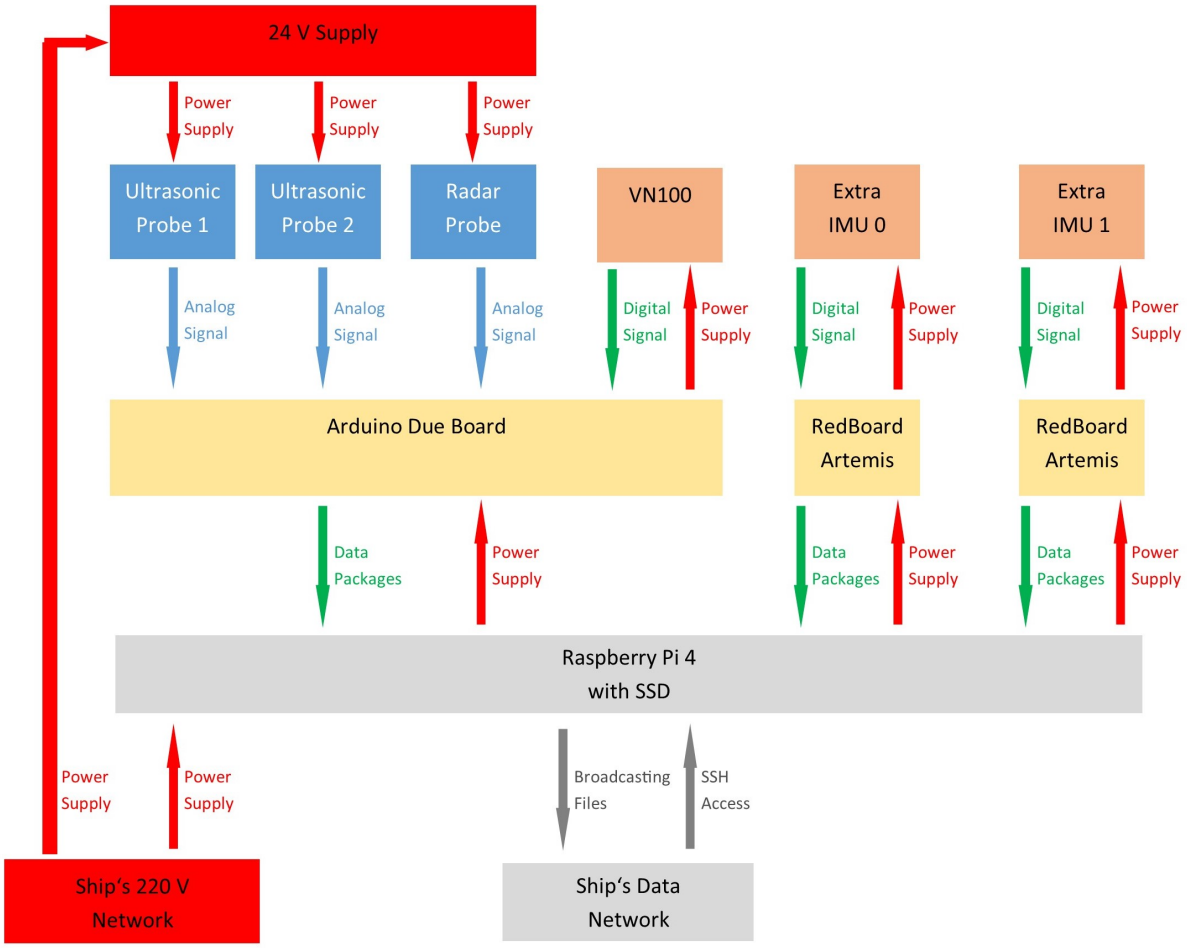

Figure 2.2: Schematics of the system's data flow and power supplies.

The altimeter probes and the VN100 are connected to the Arduino board and form the main system. The additional IMUs are operating independent of the main system, by using their own RedBoards (see figure 2.2). The purpose of the separating the probes connected to the Arduino board from the additional IMUs, is to guarantee the functionality of the main system in the case of a failure of one of the extra IMUs. For the same reason the Raspberry Pi is programmed to continue recording the measurements received from the main system in case of a failing extra IMU, but to reboot in case of problems with the main system. All parts of the system are set to operate at a frequency of 10 Hz, as this is the maximal operating frequency of the ultrasonic probes. Illustrations of all the system's components can be found in appendix 7.

2.2 The Distance Measurement Probes

2.2.1 Ultrasonic Probes IRU-3433-C60

The ultrasonic probes used are the model IRU-3433-C60 by Automation Products Group Inc (APG, 2019b). They run on 24 V direct current. The measuring range is between 0.4 m and 15.2 m. They give an analogue output in amperage ranging from 4 mA to 20 mA, corresponding to the measured distance. Their accuracy is given by ± 0.25 % of the measured distance and their resolution is given as 2.54 mm (APG, 2019b). The operating temperature of the ultrasonic probes ranges from -40 $^{\circ}C$ to 60 $^{\circ}C$ and the featured internal temperature compensation is applied. With a minimal response time of 100 ms, the maximal operating frequency of the ultrasonic probes is 10 Hz, at which they are set to operate in the system. The ultrasonic beam widens with an angle of 9 $^{\circ}$ to its middle axis, resulting in a minimal footprint with a diameter of 0.20 m at the minimal distance of 0.4 m and of and a maximal footprint with a diameter of 4.89 m at the maximal distance of 15.2 m.

2.2.2 The Radar Probe True Echo™Pulse Radar Level Transmitter

As radar probe the model PRL-050-V024-C4-SS-S6-BF-F by Products Group Inc. (APG, 2019a) with stainless steel horn antenna is used. It runs on 24 V direct current. The radar probe's operating range is between 0 m an 15 m. The output is analogue and given in amperage ranging from 4 mA to 20 mA, corresponding to the measured distance. The radar probe's accuracy is ± 0.25 % of the measured distance and the resolution is 6.1 μA (APG, 2019a). Its transducer frequency is 6.3 MHz. The operating temperature of the radar probe ranges from -40 $^{\circ}C$ to 60 $^{\circ}C$. The radar beam widens with an angle of 3 $^{\circ}$, resulting in a maximal footprint with a diameter of 1.57 m at the maximal distance of 15 m.

2.3 The Inertial Measurement Units

2.3.1 The VN100 Main IMU

The VN100 made by VectorNav Technologies (VectorNav, 2017) is the main inertial measurement unit (IMU) of the system and is therefore often just referred to as IMU, while the additional IMU systems are referred to as extra IMUs. The VN100 runs on 5 V direct current. The unit features 3-axis acellerometers, 3-axis magnetometers and 3-axis gyroscopes. It also features on board Attitude-Heading-Reference-System computation, allowing to receive the attitude parameters yaw, pitch and roll, as well as the accelerations in a North-East-Down frame. A quaternion based Extended Kalman Filter is used to gain yaw pitch and roll by comparison to the expected magnitude and direction of the gravitational acceleration vector. As the Kalman filter is based on the assumption that the acceleration vector, gained from the accelerometers, solely consists of the gravity vector, an implemented velocity aiding algorithm is used by the VN100 to avoid significant errors in pitch and roll. Therefore the assumption is made, that the overall acceleration due to motion over a long time period equals zero. As this assumption fits to the oscillatory motion of a ship, the velocity aiding algorithm of the VN100 fulfils the needs for this system. The Extended Kalman Filter uses furthermore integrated data gained from the 3-axis gyroscopes, which are compensated for drift bias, by usage of accelerometer and magnetometer measurements. The VN100 therefore reaches a resolution of 0.5 $^{\circ}$ for determining pitch and roll and a resolution of 2.0 $^{\circ}$ for the heading (VectorNav, 2022). The VN100's accelerometer's operating range goes from -16 g to 16 g, while its gyroscope is capable to measure in a range from -2000 $^{\circ}/s$ to 2000 $^{\circ}/s$. The VN100's sensors operate at 800 Hz, while the Kalman Filter operates at a rate of 400 Hz. The output parameters transmitted by the VN100 are set to be the attitude and the accelerations given in a North-East-Down frame. The output data is broadcast in binary. It is worth mentioning, that the coordinate system of the VN100 is a right handed Cartesian system with the z-axis facing downwards (see figure 2.3)

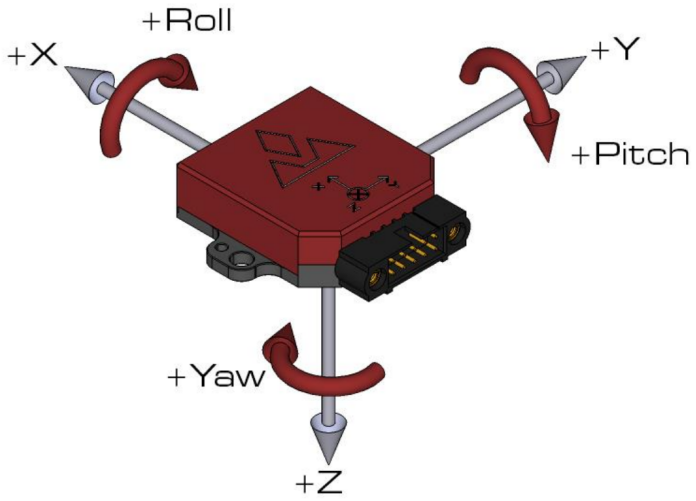

Figure 2.3: Coordinate system definition of the VN100 by VectorNav Technologies (VectorNav, 2017).

2.3.2 The additional IMU systems

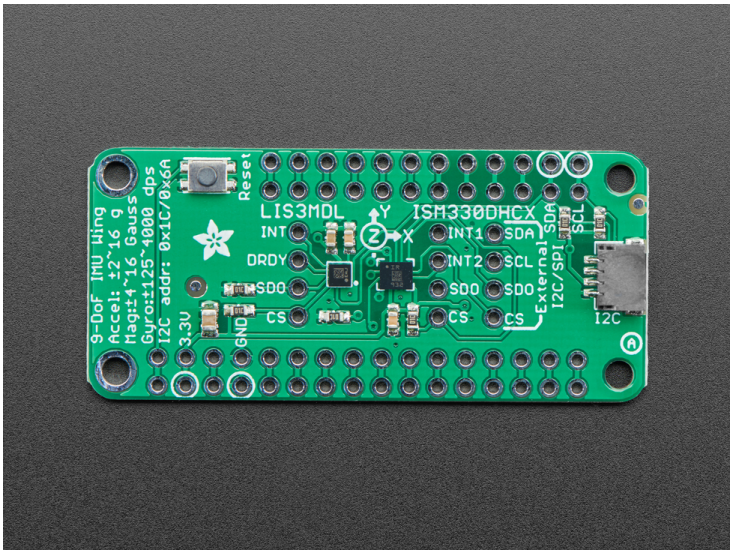

Figure 2.4: The Adafruit ISM330DHCX + LIS3MDL FeatherWing - High Precision 9-DoF IMU (Adafruit, 2022).

The two additional IMUs consist of ISM330DHCX + LIS3MDL FeatherWing - High Precision 9-DoF IMUs produced by Adafruit (Adafruit, 2022), which are each connected to a separate RedBoard Artemis, made by SparkFun Electronics (SFE, 2022). The additional IMU systems are also often referred to as extra IMUs, while the system's main IMU, the VN100 is referred to as IMU. Extra IMU 1 is hereby the name given to the additional IMU located on the bowsprit, while the extra IMU 0 is located on the starboard side of the bow. It is worth mentioning, that the coordinate systems of the extra IMUs are right handed Cartesian systems, with the z-axis pointing upwards (see figure 2.4), this is unlike the VN100s coordinate system, which z-axis faces downwards (figure 2.3).
Like the VN100 in section 2.3.1, these IMUs consist of a 3-axis accelerometer, a 3-axis gyroscope and a 3-axis magnetometer. Also they are able to estimate pitch, roll and yaw in real time and give the acceleration in a North-East-Down frame. The extra IMUs are connected to the RedBoards, processing the signals, by Qwiic cables. Both components are located in the same waterproof casing. The RedBoards are linked to the Raspberry Pi via USB connection from which they receive their power and which is used to send binary data packages of the measurements to the Raspberry Pi. The parameters saved are the pitch, the roll and the downwards acceleration.
The additional IMU systems are not a part of the main measurement system and not used for permanent data collection. They are used to realise the reconstruction of the ship motions at the altimeters' locations with the data measured by main IMU. Therefore the additional IMU systems are not designed to withstand too strong impact by the waves, even though extra IMU 1 is situated in an exposed location (see figure 2.1). Furthermore they have not been part of the system since the start of the One Ocean Expedition in Arendal on the 20.08.2021, but have been installed on the 11.10.2021, after the stay in Las Palmas de Gran Canaria.
The cases containing the additional IMUs and their RedBoards are located close to the distance measurement probes. USB-cables with signal amplifiers are used to establish the USB connection between the Raspberry Pi and the additional IMU systems over a distance of 25 m or 15 m respectively. Extra IMU 1 had initial operational problems until the 21.10.2022 and was destroyed on the 17.01.2022 during a storm in the North Atlantic (see chapter 3).

2.4 The Processing Unit

2.4.1 The Raspberry Pi

The Raspberry Pi 4 Model B 8GB (Raspberry-Pi, 2021) serves as the main controlling and data saving unit. It receives its power via USB-C from a converter plugged into a 220 V socket. The Raspberry Pi is

set to start the python scripts controlling the system when booting, and reboots in the case of a system failure. It is cased in an Argon One M.2 housing unit by Sertronics, which shall protect the Raspberry Pi board from physical harm and furthermore provides fan cooling which shall prevent overheating in warmer regions. The Raspberry Pi is connected to a SSD, located in the Argon One M.2 housing, from which it boots and on which it saves the measurement data files. The SSD has a high memory capacity and therefore allows a local storage of the data. The Raspberry Pi is linked to the local ship network via an Ethernet cable and continuously broadcasts data to the ship's research servers. It is furthermore possible to access the Raspberry Pi via SSH connection.
The launch scripts for the several parts of the system are executed one after another by the main launching script and the output is copied to a local text file, allowing a detailed analysis of component failures and a fast development of fixing methods. The system reboots automatically in case of a failure of any of the components managed by the Arduino Board, namely the altimeters and the VN100 IMU. The system continues its operating cycle in case of a missing signal from the additional IMUs as this data is not regarded to be crucial.
A system cycle lasts for 30 *minutes*. At the end of a system cycle, the data measured during the cycle is saved in a compressed lzma file on the local SSD of the Raspberry Pi. At the beginning of a cycle the scripts are relaunched. If any of the additional IMUs lost connection during the last cycle, the connection is tried to be reestablished at the beginning of the next cycle.
The Raspberry Pi is linked to the Arduino Board and the additional IMUs via USB connection. The operating scripts of the Arduino Board and the additional IMUs are programmed on them locally and start, once they receive power from the Raspberry Pi via the USB connection. The Arduino Board and the additional IMUs send their data package via a bitwise serial connection to the Raspberry Pi. The incoming messages are stored by the Raspberry Pi in a text file and receive a time stamp based on the time of the Raspberry Pi. As the Raspberry Pi 4 Model B does not feature an on-board real time clock, an additional real time clock is fitted to the Raspberry Pi via pin connection. The used clock is the the DS1307 RTC by Seeed Studio, which is powered by its own lithium cell and therefore independent from the Raspberry Pi's power connection.

2.4.2 The Arduino Due

The Arduino Due, made by Arduino AG (Arduino, 2022) is used to process the incoming signals of the altimeter probes and the VN100 IMU and send them to the Raspberry Pi as binary data packages via a serial connection. The Arduino board is fully programmable and allows for 512 KB of code on its flash memory. It runs on a 32-bit core, operating at 84 MHz and features 96 KB of SRAM.
As the altimeter probes output an analogue signal in amperage (section 2.2.1, 2.2.2), but the analogue reading pins of the Arduino Due are made to measure Voltage, resistors are used, to transfer the signals from amperage to voltage. The output signal of the probes ranges from 4 mA to 20 mA. The measuring range of the Arduino board's analogue read pins goes from 0 V to 3.3 V. To not exceed the Voltage limit of the Arduino board, resistors of 160 Ω are used resulting in a maximal Voltage of $0.02\ A\ \cdot\ 160\ \Omega\ = 3.2\ V$. The maximal resolution of the Arduino Due's analogue read pins is 12 *bits*, allowing to have 4096 different values over the measuring range from 0 V to 3.3 V, resulting in a theoretical measurement resolution of 0.0008 V.
The output signal of the VN100 IMU is digital bitwise. The VN100 operates at 5 V and receives its power from the 5 V power output pin of the Arduino Due. As the digital output signal of the VN100 is also given in 5 V, but the Arduino Due is running on 3.3 V, a circuit is needed to shift the signal voltage from 5 V down to 3 V. This is realised by usage of a MAX3323EEPE transceiver produced by Maxim Integrated. The voltage shifting circuit, as well as the resistors for amperage to voltage transformation of the probes signals, are located on an electric circuit shield, pinned on top of the Arduino Due. Also, the power distribution for the three altimeter probes is located on this shield. The probes take a voltage input of 24 V, which is delivered by a converter plugged into a 220 V socket. The circuit shield features one common ground connecting all the groundings of the different circuits. The entire circuitry is shown in figure 2.5.

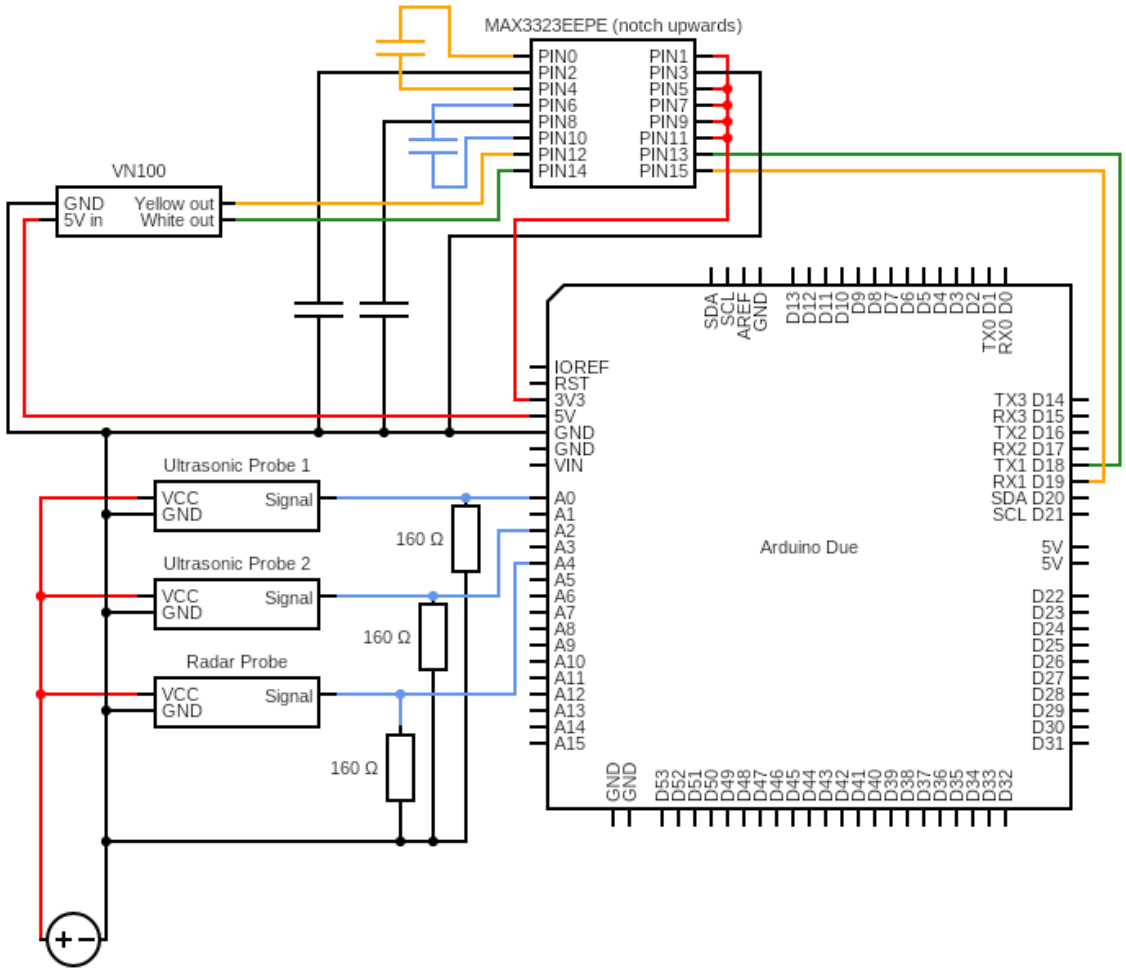

Figure 2.5: Circuit diagram of the connections between the probes, the VN100 and the Arduino Due.

CHAPTER 3

Data Acquisition

Figure 3.1: Mounting of the ultrasonic altimeter probe 1 under the bowsprit tip on the 16.06.2021 in Bergen/ Norway (Picture by Marita Aarekol).

The main system, described in section, 2 was developed and built by Jean Rabault during April and May 2021. It was mounted on the Statsraad Lehmkuhl on the 16.06.2021 in Bergen (see figure 3.1). This system did not include the two extra IMUs yet. After it became clear, that the possibilities of measuring the spatial relationships between the probes and the VN100 are insufficient, it was decided, that two extra IMUs should be built and placed near the probes, to allow an insight on the motion behaviour of the probes locations. These two additional IMUs were designed by Jean Rabault and built by him and me in September 2021. During September, 2021 I furthermore set up an additional Raspberry Pi 4 unit, an additional Arduino Due Board and three more ultrasonic distant measurement probes to serve as spare parts. These parts are all identical to the ones of the original system, as described in the sections 2.4.1, 2.4.2 and 2.2.1 respectively. In addition, I built a slightly adapted version of the original circuit shield (see figure 2.5). During the mounting of the system, a Voltage peak, caused by plugging in one of the probes, burned a pin of the first Arduino board, which was replaced on the same day. The spare circuit shield therefore features resistors of 130 Ω ,instead of 160 Ω resistors show in figure 2.5. Furthermore, 4.7 $k\Omega$ resistors are connected in series to the analogue measuring pins of the Arduino board to protect them from burning. The newer shield has not been installed, but serves as a spare part in case another Arduino board is damaged by a voltage peak, which is regarded to be unlikely with the currently installed parts.

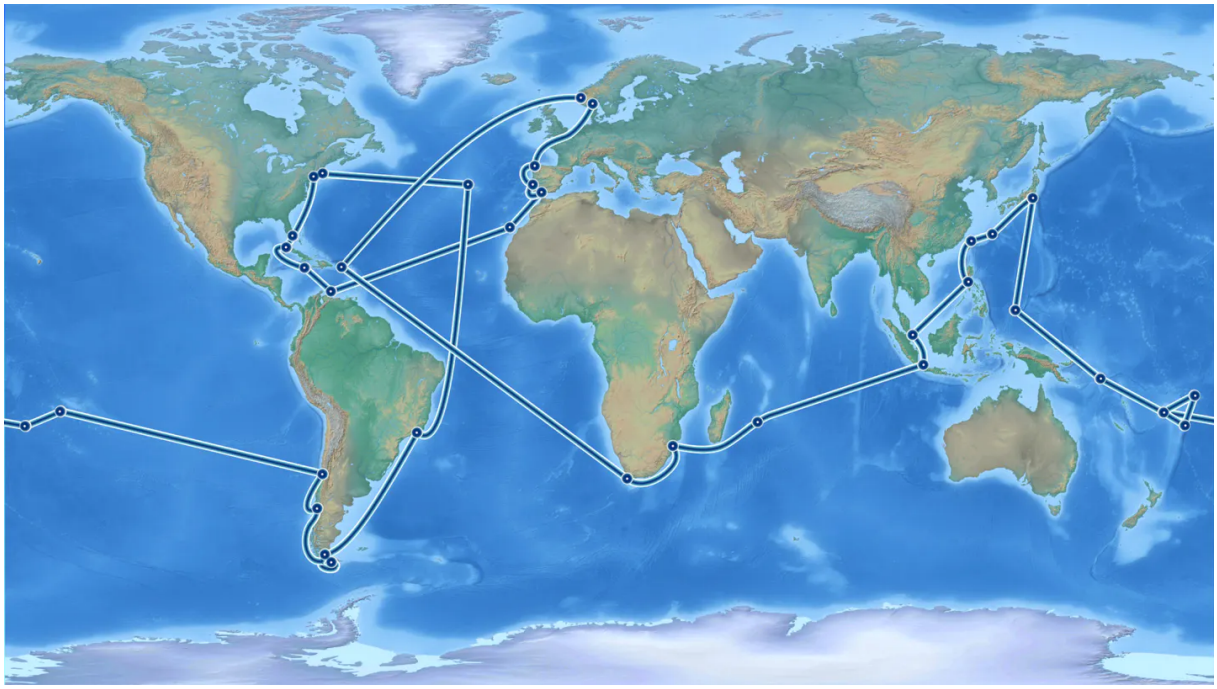

Figure 3.2: Planned sailing route of the One Ocean Expedition (2021-2023) (One-Ocean-Expedition-website, 2022).

The One Ocean Expedition is planned as a circumnavigation from 2021 to 2023 (see figure 3.2). The Expedition started, when the Statsraad Lehmkuhl set sail from Arendal/ Norway to La Corunña/ Spain on the 20.08.2021. I boarded the ship on the 2.10.2021 in Las Palmas de Gran Canaria and sailed with it until the 27.11.2021 to Havanna/ Cuba (see figure 3.3). My main task for the project of the wave measurement system, was to ensure that the system continues working, to mount and install the extra IMUs and to monitor the systems behaviour. Until then, the system had operated flawlessly, while the ship sailed down Europe and North-Africa. It was in question what would happen to the system when the Statsraad Lehmkuhl sails across the Atlantic and into the Caribbean during the Hurricane season.

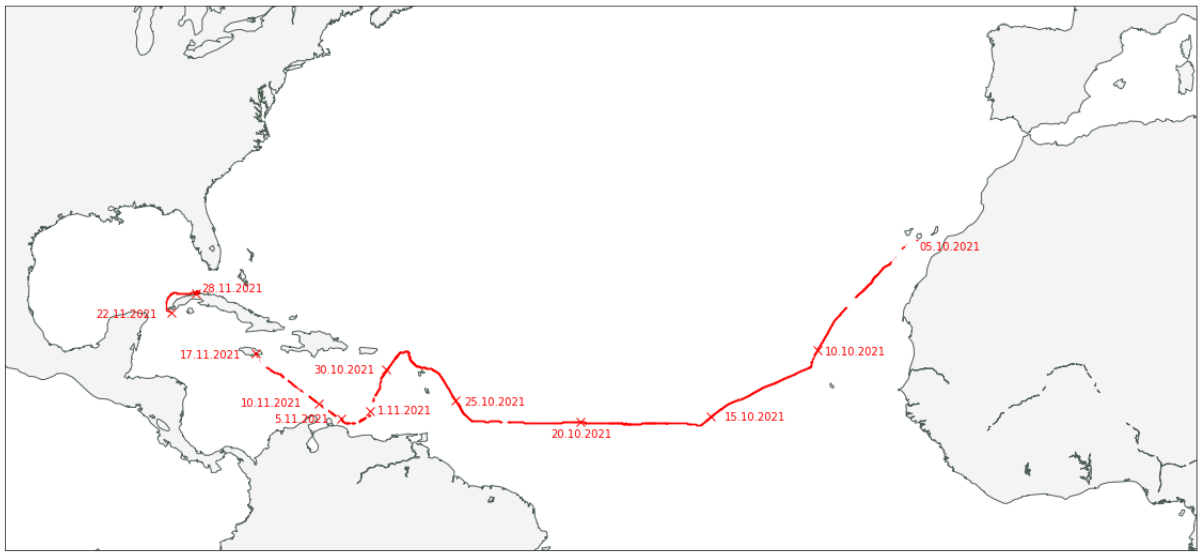

Figure 3.3: Leg from Las Palmas de Gran Canaria to Havanna/ Cuba via Willemstad/ Curacao and Port Royal/ Jamaica during October and November 2021 (position data originates from NORCE (2022)).

I mounted the extra IMUs in their designated locations on the 11.10.2021. During the following days the extra IMU 1 at the bowsprit proved itself to be rather unreliable, as it frequently lost connection after recording data for the first few minutes of a semi-hourly measuring period. The system would then reboot itself after half an hour to regain connection and then the additional IMU would record again for some minutes, before losing connection. After some consideration, I found the error in the power supply of the extra IMU 1. As described in section 2.3.2, a 25 m long USB-cable is used to connect the extra IMU 1to the Raspberry Pi, which also serves as its power supply. The 25 m cable was not plugged directly into the Raspberry Pi, but into a shorter USB-cable glued into the watertight plastic casing of the processing unit, that was then plugged into the Raspberry Pi inside the casing. It appears, that this small intersection, from the outside to the inside of the watertight casing, increased the resistance to a point, where the extra IMU 1 did not receive enough power. I therefore removed the intersection and drilled a hole in the watertight casing to plug the 25 m USB-cable directly into the Raspberry Pi and to create a direct end-to-end connection with the extra IMU 1. I sealed the hole watertight with silicone again. I undertook this fix on the 21.10.2021. After this the extra IMU 1 worked reliable until the 17.01.2022, when it was destroyed during a strong cyclone in the North Atlantic. During its time of operation the extra IMU 1 already collected enough data, which is used in section 4.1.5.
Until I left the ship on the 27.11.2022, the wave sensor system continued working without any problems and does so ever-since. Only the destruction of the extra IMU 1 on the 17.01.2022 created an error in the system, which was fixed remotely, by advising the student research assistants of this leg to unplug the USB-connection to the extra IMU 1 and reboot the system.

Figure 3.4: Research instruments and system installed on board the Statsraad Lehmkuhl for the One Ocean Expedition (2021-2023) (One-Ocean-Expedition-website, 2022).

To receive the needed time on board the ship, I filled in one of the student research assistant positions on the One Ocean Expedition for the leg from Las Palmas de Gran Canaria to Havanna/ Cuba. For every leg of the One Ocean Expedition two student research assistants cover tasks of maintaining the measurement systems of the different scientific projects (see figure 3.4), as well as operating some of them and taking samples for the biological projects on board. The working routine for the student research assistants is therefore strictly scheduled, as especially the projects which rely on manual sampling have the demand for the maximal possible sampling frequency, to gain the best spatial resolution. My tasks on board the ship, which I was occupied with most of the time, were therefore micro-plastic filtration, and eDNA sampling and analysis. The project by NORCE, concerning it self with environmental DNA traces (eDNA), had provided laboratory supplies for PCR-tests on board of the ship, allowing the on

board processing of the eDNA samples gained by the filtration of sea water and additionally the storage of extracted DNA in a freezer. Besides the sampling, the cleaning and repairing of various autonomous measuring systems (see figure 3.4) and the processing of observations made by the crew into files on the ships server, took up most of my time. In regular time intervals the ship was stopped to lower a CTD-probe and a plankton net. The CTD-probe should measure the conductivity, temperature and pressure of the sea water as a time series while it was lowered down to a depth of 700 m and heaved back up again. The plankton net was lowered down to 200 m of depth and then dragged up again. During this process zoo-plankton was collected by the net and flushed into a container at its bottom. Back on board the ship the zoo-plankton was stored in ethanol and stored in a fridge. Due to the full time work schedule as a student research assistant on board the Statsraad Lehmkuhl and a limited internet connection, it was not possible for me to start post processing or analysing any of the data measured by our wave sensor system while being on board the ship from 02.10.2021 to 27.11.2021.
In addition to the time series of data recorded autonomously by the wave sensor system, I wrote daily notes about my visual observations regarding the waves. The notes are mainly used in this thesis for section 5.4, to find specific wave types of interest for detailed spectral analysis.

CHAPTER 4

Methods

4.1 Post Processing of the Raw Data

4.1.1 Time Synchronisation

Since the maximal operating frequency of the ultrasonic probes is 10 Hz (section 2.2.1), the entire system is designed to operate at 10 Hz. The data from the altimeter probes, the VN100 and the additional IMUs is therefore taken every 0.1 s and sent in a data package to the Raspberry Pi, which marks it with a timestamp based on its time of receiving. The different system components are however not working synchronous. Data from the probes, the VN100 and both additional IMUs are sent after each other. In order to connect a distance measurement from an altimeter probe to the data of an IMU and thereby with the relative position of the altimeter, the data from the different system components needs to be synchronised. Therefore, a common time base is defined, ranging from the first time when data from all system components has been received in a 30 minute data set, until the earliest of the last data packages received by the Raspberry Pi. The time steps between two time points is chosen to be 0.1 s. The 30 minute data sets of each of the systems components are interpolated linear over the defined common time base. As all components operate as a frequency of 10 Hz, the maximal difference between the time of measurement and the time of the common time base, that is interpolated upon is $0.05s$. In case of a failure of one of the additional IMUs, they are excluded from the generation of the common time base.

4.1.2 Determining the Spatial Orientations of the IMUs

Determining the IMUs' Default Pitch and Roll Offsets

At the IMU locations, a perfectly horizontal mounting of the IMUs is almost impossible. Therefore the default offset values of pitch and roll, for when the ship is steady, must be determined for each IMU, to be later subtracted from the measured values for pitch and roll. For the determination of the default pitch and roll offsets, data sets are used, from when the ship was moored fast in harbour with minimal motion. The used intervals are from 06.11.2021 to 07.11.2021, when the ship was moored in Willemstad/ Curacao and from 25.11.2021 to 27.11.2021, when the ship was moored in Havanna/ Cuba. The period when the ship was in Port Royal, Jamaica is not used, as there it wasn't made fast to a steady harbour wall, but under anchor and tied to a swimming platform, allowing free motion of the ship's hull. The default offset pitch and roll values are computed as the mean pitch and roll over the taken data sets and are given in table 4.1. It has to be mentioned, that the ship's position in the water changes slightly with different loading states. Especially the levels in the fuel tank and the wastewater tank can shift the ship's gravitational centre, resulting in a small change of the default pitch and roll values for the specific loading situation.

	default pitch offset	default roll offset
VN100	-1.762 °	-0.245 °
extra IMU 0	-7.948 °	11.420 °
extra IMU 1	-31.047 °	10.627 °

Table 4.1: Default pitch and roll offset values for the different IMUs after the 11.10.2021.

Only these two harbour periods are used for the determination of the default offset values, as the data from later harbour states of the ship is not yet accessible at this stage of the post processing, and as earlier harbour stays were before the 11.10.2021, on which the extra IMUs were fitted, as well as the

VN100 was reoriented slightly.
As data before the 11.10.2021, data sets from the ship's harbour stays in Lisbon/ Portugal from 03.09.2021 to 04.09.2021 and in Cadiz/ Spain from 10.09.2021 to 14.09.2021 are used to determine the VN100's default offset values for this period. They are given in table 4.2.

	default pitch offset	default roll offset
VN100	−2.465 °	0.508 °

Table 4.2: Default pitch and roll offset values for the VN100 before the 11.10.2021.

It is worth mentioning, that the coordinate system definition of the VN100 differs to the one of the additional IMUs, as can be seen in the figures 2.3 and 2.4. The z-axis of the VN100 is facing downwards and the y-axis pointing toward starboard side resulting in the pitch being positive in counterclockwise direction, when viewing at the ship from starboard to portside. The z-axis of the extra IMUs however is facing upwards and the y-axis is pointing towards portside, resulting in the pitch being positive in clockwise direction, when viewing at the ship from starboard to port-side. This fact is taken account for in section 4.1.2.

Determining the IMUs' Default Yaw Offsets

Not only are the IMUs not perfectly orientated horizontally, but also are their x-axes not perfectly aligned with the midships-axis of the ship, due to a lack of reference at the mounting positions. This results in a falsification of the measured pitch and roll values, which can be compensated, if the yaw offsets of the IMUs, meaning the angles between the IMUs' x-axes and midships, are known.
To determine the yaw offsets, it is assumed, that the main motion axes of the ship lie along its geometrical axes, especially, that the largest motion of the ship happens along its y-axis, as the c_{ii} coefficient (Newman, 2018) should be minimal along this axis, regarding the ship's geometry. As the c_{ii} coefficient (Newman, 2018) should be largest along the ship's x-axis, the ship's motion should be minimal along its x-axis. Therefore, Principal Component Analysis is used to analyse the ship's motion in the pitch-roll plane, as it is measured by the individual IMUs.

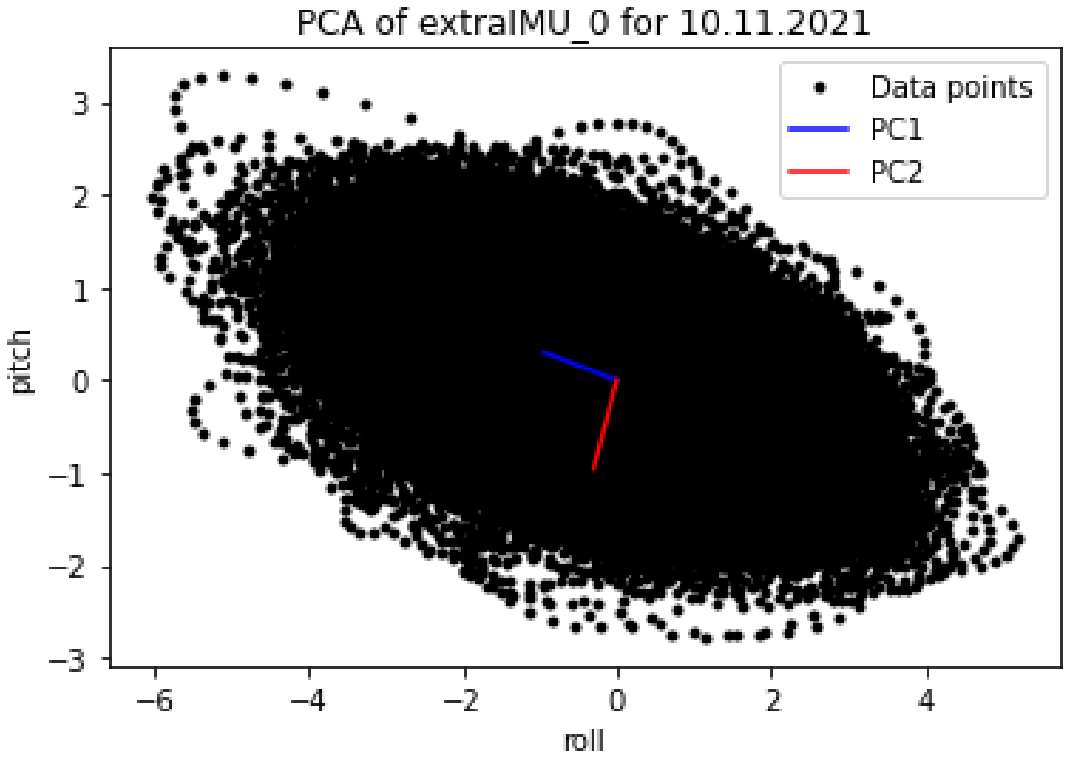

Figure 4.1: Principal Component Analysis of the pitch and roll data measured by extra IMU 0 on the 10.11.2021.

Figure 4.1 shows the measured pitch and roll values during the 10.11.2021. PC1 and PC2 are the first and second principle component vectors, both are of length 1. PC1 hereby lies on the axis along which the data points show the largest variance. PC2 stands perpendicular to PC1 and shows the direction of minimal variance in the data points. Under the assumption that the ship's motion is largest along its y-axis and minimal along its x-axis, the first principle component PC1 should represent the ship's y-axis, while the second principle component PC2 represents its x-axis.
It can however be seen in figure 4.2, that the principle components for the individual IMUs are not constant over the data sets, but differ in direction over time.

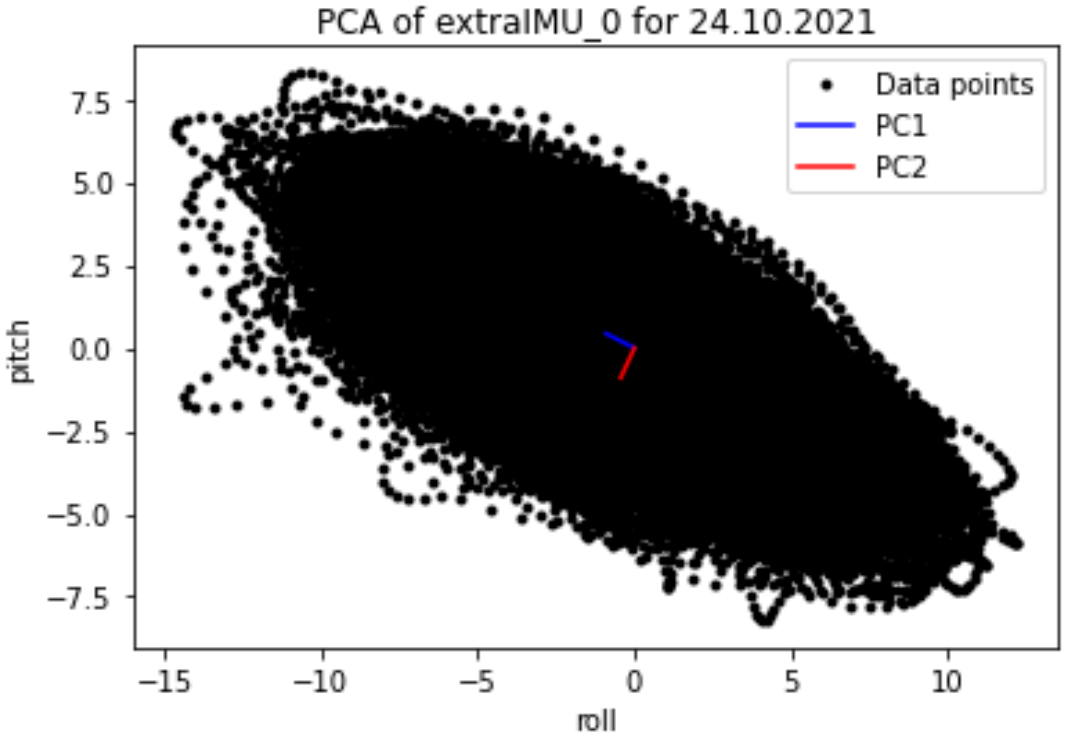

Figure 4.2: Principal Component Analysis of the pitch and roll data measured by extra IMU 0 on the 24.10.2021.

To evaluate the behaviour of the principle components for different data sets and to find a reason for the directional differences, the Principle Component Analysis is applied to data sets of different length, over the time period from 22.10.2021 to 24.11.2021 (see figure 4.3).

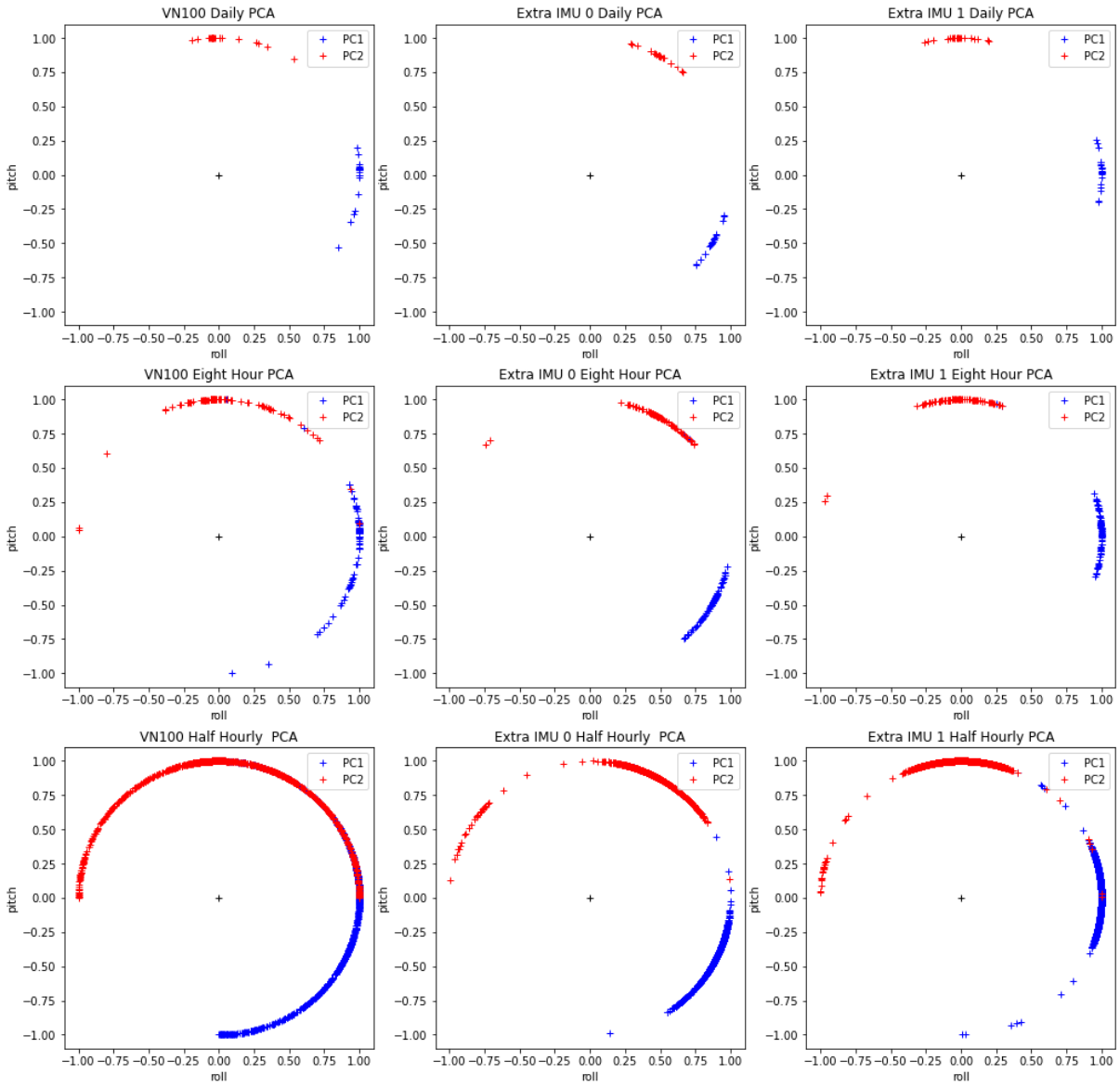

Figure 4.3: Principal Component Analysis of the pitch and roll data over different time lengths for the period from 22.10.2021 to 24.11.2021.

It can be seen in figure 4.3, that though the principle components wander in time, clusters can be seen around certain points. Also the variance in the principle components seem to decrease strongly if the Principle Component Analysis is applied to data sets of a longer time period. Therefore the hypothesis is made, that the changes in the directions of the principle components are random. In that case the empirical distribution functions should have the shape of a Gaussian bell function. The maxima of the function should then correspond to the direction of the ship's y-axis in relation to the y-axes of the IMUs. In addition to the Principle Component Analysis applied on the data set of the mentioned period, also another specific data set is viewed upon. From time to time the ship was "heaved to", meaning that the sails of Foremast and Mainmast were braced perpendicular towards each other, so that the sails on one mast catch the wind from the front while the sails on the other mast are filled by the wind from the back. The forces on the masts then counteract each other, resulting in the ship positioning itself perpendicular to the wind direction and having no speed despite a small drift sideways. As the waves were almost exclusively coming in from the same direction as the wind during the period from 22.10.2021 to 24.11.2021, the wave direction during the "heaved to" events is mostly perpendicular to the ship's heading and the data set of the "heaved to" events should be free of any influence by a changing wave direction. The data set built up by only these "heaving to" events is therefore additionally chosen for the Principle Component Analysis with a 30 *min* duration, to examine, whether the wave direction in relation to the

ship's heading has a significant influence on the results of the Principle Component Analysis by it's effect on the ship's motion.

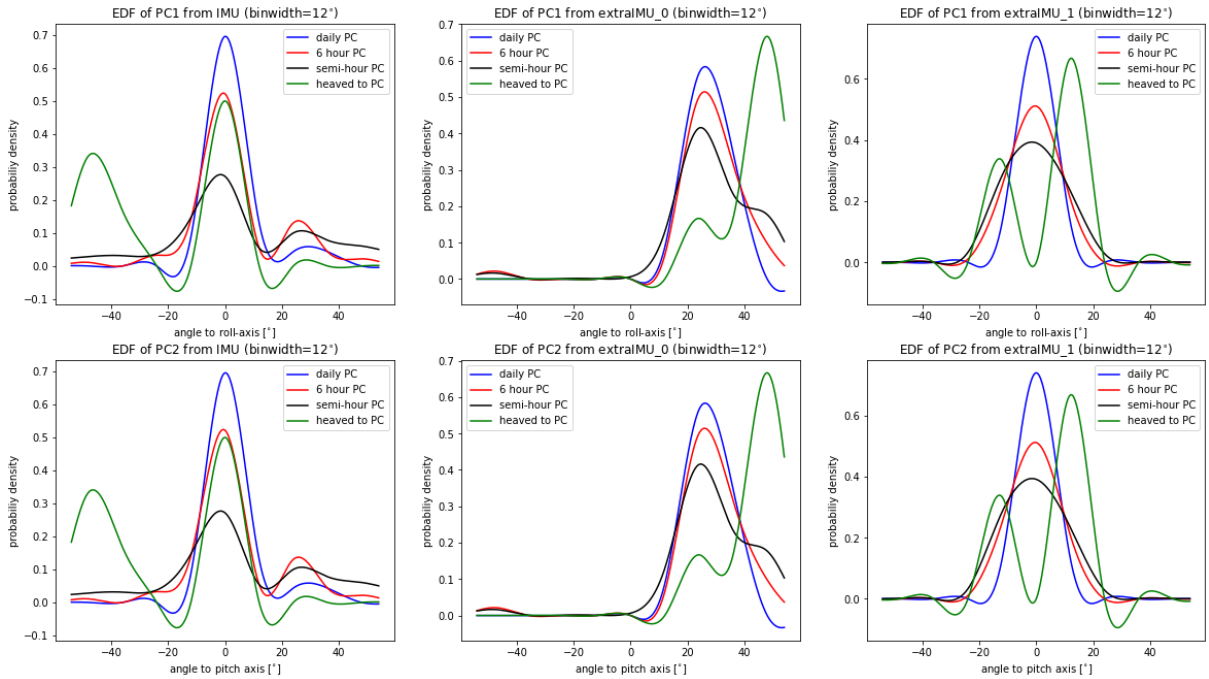

Figure 4.4: Empirical Distribution Function with a bin-width of 12 ° for Principle Component Analyses over different time intervals for the period from 22.10.2021 to 24.11.2021.

The angles in figure 4.4 are defined as the angle between the roll-axis and the vector PC1, as it is shown in figure 4.3 and as the angle between the pitch-axis and PC2, as it is shown in figure 4.3. The Empirical Distribution Function used for figure 4.4 used a bin-width of 12 °. The values depicted in figure 4.4 however result from a cubic interpolation between the bins mid points, which the bin values were assigned to. The resolution of figure 4.4 therefore lies at 0.01 °.
It can be seen in figure 4.4, that the Empirical Distribution Function of the principle components indeed resembles a Gaussian shape to a certain degree. Furthermore it can be seen, that the principle component distribution for the "heaved to" data set does not show a smaller variance, but rather seems to be subject to more uncertainty, than the distributions of larger data sets. It is also recognisable, that the peaks of the different time lengths used for the Principle Component Analyses align with each other and that the peak is more distinct when a longer time interval is used for the PCA. It is therefore assumed, that the variance of the distribution is of random nature and not caused by the ship's course to the waves.
Observation of Empirical Distribution Functions of the Principle Components with a smaller bin-width in figure 4.5 show a clearer peak, but also more disturbance on its sides.

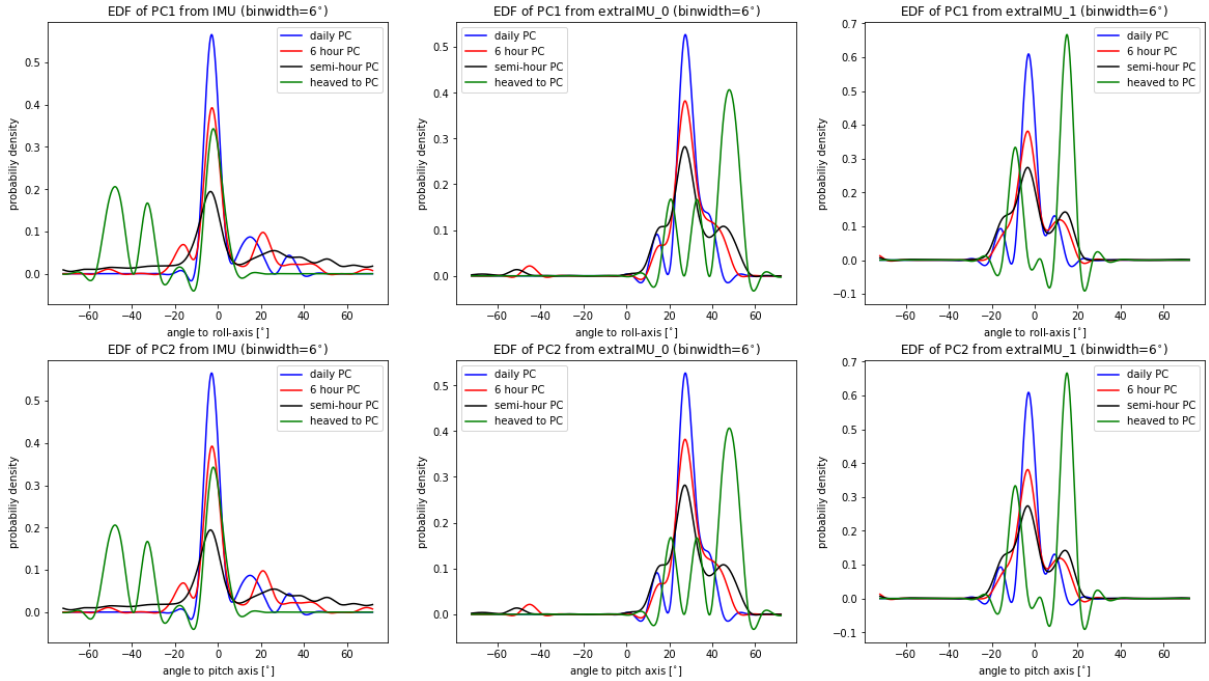

Figure 4.5: Empirical Distribution Function with a bin-width of 6 ° for Principle Component Analyses over different time intervals for the period from 22.10.2021 to 24.11.2021.

As the peak probability of the daily Principle Component Analysis is over 50 % (see figure 4.5) and has a mostly symmetrical shape, the angle of the peak probability is defined as the yaw offset of the individual IMUs. The angle is hereby taken from the cubic interpolation of the Empirical Distribution Function of a 6 ° bin-width , with a resolution of 0.01 °. The resulting yaw offsets are given in table 4.3.

	yaw offset
VN100	−2.7 °
extra IMU 0	30.1 °
extra IMU 1	10.6 °

Table 4.3: Yaw offset values for the different IMUs after the 11.10.202.1

The relation between the yaw offsets as seen in table 4.3 and the orientations of the IMUs to the ship's coordinate system is discussed in section 4.1.3. As mentioned in section 4.1.2, the orientation of the VN100 was changed on the 11.10.2021. The yaw offset for the VN100 before the 11.10.2021 is determined by the same method and given in table **??**.

	yaw offset
VN100	3.7 °

Table 4.4: Yaw offset value for the VN100 before the 11.10.2021

4.1.3 Correcting the IMUs' Readings for Their Spatial Orientation

The first step in correcting the IMUs' pitch and roll readings is to subtract the default offsets, which have been computed in section 4.1.2 and are given in the tables 4.1, 4.2.

$$pitch_{corr1} = pitch_{raw} - pitch_{offset} \tag{4.1}$$

$$roll_{corr1} = roll_{raw} - roll_{offset} \tag{4.2}$$

The offset corrected pitch and roll values now reflect an IMU orientation, in which the IMUs are aligned horizontally. To find the real pitch and roll values corresponding to the ships motion, The x-axes of the IMUs must be virtually aligned with the x-axis of the ship, which is defined by midships. therefore the yaw offset, which has been computed in section 4.1.2 and is given in the tables 4.3 and **??**, is used. The yaw offsets in section 4.1.2 are evaluated by the positions of the Principle Components in relation to pitch and roll as they are defined by the IMUs. Therefore, the yaw offsets correspond to the angles from the IMUs' x-axes to the ship's x-axis. This angle shall further be denoted as α (see figure 4.6, 4.7).
An important circumstance, that has to be accounted for in the correction of the pitch and roll parameters, is, that the coordinate systems of the extra IMUs differ from the one of the VN100, as it can be seen in the figures 2.3, 2.4 and is illustrated in the figures 4.6, 4.7. The yaw offset, as it has been determined in section 4.1.2, corresponds to the coordinate system of the extra IMUs. To have only one universal coordinate system for the entire ship, which will be used for all computations and definitions in the following, the coordinate system of the extra IMUs chosen. The upwards-facing z-axis of this coordinate system seems more natural. The readings of the VN100 are transferred into this coordinate system further on in this section.

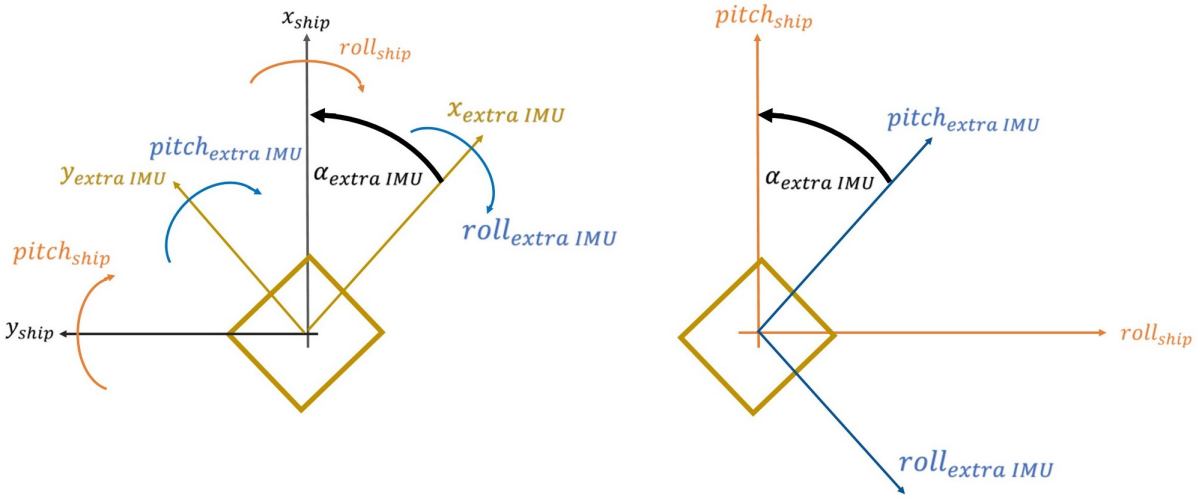

Figure 4.6: *Left*: Coordinate system of the ship as it is defined by the extra IMUs, with an extra IMU orientated at a yaw offset α and the resulting coordinate system for the extra IMU.
Right: Pitch over roll plane as it is defined by the ship's coordinate system, with an extra IMU orientated at a yaw offset α and the resulting pitch over roll plane for the extra IMU.

The correction of the pitch and roll values measured by the extra IMUs is realised by usage of the two dimensional Rotation Matrix. For the rotation of a vector in a right-handed coordinate system, the two dimensional Rotation Matrix is given as:

$$R_\alpha = \begin{pmatrix} cos(\alpha) & -sin(\alpha) \\ sin(\alpha) & cos(\alpha) \end{pmatrix} \tag{4.3}$$

For the case of a coordinate system that is rotated, the vector in the rotated coordinate system is gained by multiplication of the vector given, in the original coordinates, with the inverse of the Rotation Matrix.

$$\begin{pmatrix} roll_{corr2} \\ pitch_{corr2} \end{pmatrix} = \begin{pmatrix} cos(\alpha) & sin(\alpha) \\ -sin(\alpha) & cos(\alpha) \end{pmatrix} \begin{pmatrix} roll_{corr1} \\ pitch_{corr1} \end{pmatrix} \tag{4.4}$$

For the extra IMUs, the pitch over roll plane, as it is given by their coordinate system (see figure 4.6) follows the same definition as the one used to determine the yaw offsets (section 4.1.2). This allows the

direct use of equation 4.4, to gain the pitch and roll values for the ship's motion from the measured and offset-corrected pitch and roll values.

$$roll_{ship} = roll_{extraIMU,corr2} \tag{4.5}$$
$$pitch_{ship} = pitch_{extraIMU,corr2} \tag{4.6}$$

As the VN100 has a different coordinate system defined for its measurements, it has to be treated separately.

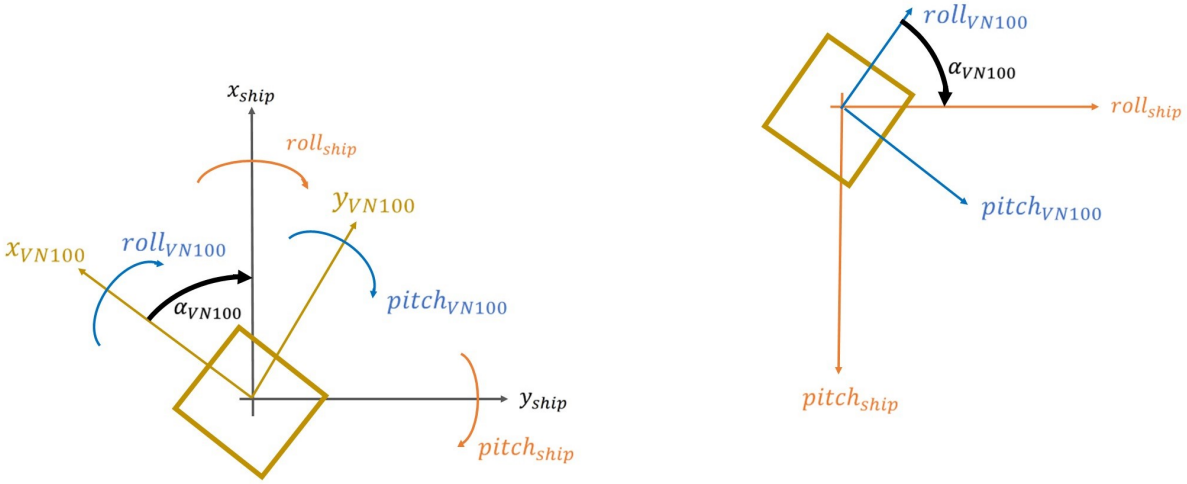

Figure 4.7: *Left*: Coordinate system of the ship as it would be defined by the VN100, with the VN100 orientated at a yaw offset α and the resulting coordinate system for the VN100.
Right: Pitch over roll plane as it would be defined by the ship's coordinate system from the VN100, with the VN100 orientated at a yaw offset α and the resulting pitch over roll plane for the VN100.

As it can be seen in figure 4.7, the pitch and roll plane defined by the VN100's coordinate system is mirrored around the roll-axis in comparison to the pitch and roll plane which was used in section 4.1.2 to determine the yaw offset for the VN100. From this follows, that the yaw offset of the VN100 must change sign in order to correspond to the rotation angle α_{VN100} in the VN100's coordinate system.

$$\alpha_{VN100} = -yaw_{offset,VN100} \tag{4.7}$$

As the pitch and roll plane of the VN100 is a right-handed coordinate system, equation 4.3 and 4.4 can be used. The corrected pitch value for the VN100 must be converted into the pitch value for the ship. As the x-axes of both coordinate systems are the same, the roll is also the same. As the y-axes of the coordinate systems are opposite, the pitch by the VN100's definition changes sign.

$$roll_{ship} = roll_{VN100,corr2} \tag{4.8}$$
$$pitch_{ship} = -pitch_{VN100,corr2} \tag{4.9}$$

4.1.4 Determining the Vertical Position of the IMUs

The vertical position of the IMUs serves to determine the vertical position of the altimeter probes, which is used for the computation of the water surface elevation. Hereby the total vertical position is not important. The value of interest is the sensors' vertical position in relation to its position of rest. This vertical position z shall be defined as increasing upwards opposite to the gravitational acceleration vector $\vec{g}$. As it is described in section 2.3.1 and section 2.3.2, the IMUs are able to output the acceleration in a North-East-Down framework, where north and east are determined by the magnetometers and down is defined by the vector of the gravitational force. The measured downwards acceleration minus the gravitational acceleration g therefore corresponds to the negative acceleration of z.

$$acceleration_{Down,IMU} - g = -\ddot{z}_{IMU} \tag{4.10}$$

To receive the vertical position of an IMU z_{IMU}, its acceleration $\ddot{z}_{IMU}$ must be integrated twice. To realise this, it is assumed that the motion of the ship ,and thereby the vertical motion of the IMUs and probes, resembles an oscillating motion. In this case the vertical acceleration $\ddot{z}_{IMU}$ and the vertical position z_{IMU} can be Fourier transformed.
In Fourier Space the following relationship for derivatives can be found:

$$\mathcal{F}[\dot{f}(t)](\omega) = i\omega\mathcal{F}[f(t)](\omega) \tag{4.11}$$

The integration of the vertical acceleration can thus be realised by multiplication with $\frac{-1}{\omega^2}$ in Fourier Space.

$$z(t) = \mathcal{F}^{-1}\left[\frac{-1}{\omega^2}\mathcal{F}[\ddot{z}(t)](\omega)\right](t) \tag{4.12}$$

It has to be mentioned, that the integration in Fourier space does not account for constants, that would be added to a regular integration and is therefore invalid if any constants are added. As $z(t)$ describes the oscillation of the vertical position around the position of rest, it is assumed to oscillate around 0 and therefore cannot be subject to constants.
The transformation into Fourier space and back might cause errors at the beginning and end of a data file. Therefore the first and last 3000 data points (or $\approx 5min$) of each 30 min data file are cut off, after the IMU's vertical positions are computed. The Fourier transform and inverse Fourier transform are realised by Fast Fourier Transformation.

4.1.5 Emulating of the Motion of the Gauges with the VN100 Measurements

As it can be seen in figure 2.1, the systems main IMU (VN100) is located at a significant distance from the altimeter probes. To evaluate the motions of the sensors corresponding to the values measured by the VN100, the additional IMUs were mounted close to the sensor positions. The parameter of interest is the vertical position z, as it is described in section 4.1.4. The parameters pitch and roll are theoretically equal for all IMUs and probes regardless of their location.
In the following section, the focus is put upon emulating the motion of the ultrasonic probe at the bowsprit, which is measured by extra IMU 1. The analysis of the motion relationship between the extra IMU 0 and the VN100 works analogue and is therefore not discussed, to avoid unnecessary repetition. The results for the motion emulation of the extra IMU 0 are given in table 4.8.

Geometric Approach

The spatial distances between the VN100 and the extra IMU 1 are given by the vector 4.13, when the ship is at rest.

$$\Delta\vec{x}_{extraIMU1} = \begin{pmatrix}\Delta x\\ \Delta y\\ \Delta z\end{pmatrix} \tag{4.13}$$

The motion of the ship's hull is described by three significant degrees oft freedom: pitch, roll and z. For the IMUs, the lateral motion of the entire ship hull is the same, regardless of their position. Differences in the IMUs relative positions occur due to their different distances to the pivot point of the ship in combination with its pitch and roll. The motion of the extra IMU 1 is therefore given by the motion of the VN100 plus a term depending on the pitch and roll and the spatial distances between the sensors $\Delta\vec{x}_{extraIMU1}$. This term can be found by multiplication of $\Delta\vec{x}_{extraIMU1}$ with a three dimensional Rotation Matrix, depending on the pitch and roll of the ship.

$$\vec{\tilde{x}}_{extraIMU1} = \vec{x}_{VN100} + R(pitch, roll)\Delta\vec{x}_{extraIMU1} \tag{4.14}$$

The Rotation Matrix is composed of the Rotation Matrix around the x-axis in the y-z plane $R_x(roll)$ and the Rotation Matrix around the y-axis in the x-z plane $R_y(pitch)$.

$$R(pitch, roll) = R_y(pitch)R_x(roll) \tag{4.15}$$

$$R_x(roll) = \begin{pmatrix}1 & 0 & 0\\ 0 & cos(roll) & -sin(roll)\\ 0 & sin(roll) & cos(roll)\end{pmatrix} \tag{4.16}$$

$$R_y(pitch) = \begin{pmatrix}cos(pitch) & 0 & sin(pitch)\\ 0 & 1 & 0\\ -sin(pitch) & 0 & cos(pitch\end{pmatrix} \tag{4.17}$$

$$R_{xy}(pitch, roll) = \begin{pmatrix}cos(pitch) & sin(pitch)sin(roll) & sin(pitch)cos(roll)\\ 0 & cos(roll) & -sin(roll)\\ -sin(pitch) & sin(roll)cos(pitch) & cos(roll)cos(pitch)\end{pmatrix} \tag{4.18}$$

As only the vertical position is of interest, equation 4.14 and 4.18 are simplified as:

$$\tilde{z}_{extraIMU1} = z_{VN100} - sin(pitch)\Delta x + sin(roll)cos(pitch)\Delta y + cos(roll)cos(pitch)\Delta z \tag{4.19}$$

Here $\tilde{z}_{extraIMU1}$ denotes the vertical Position of the extra IMU 1 seen from the z definition of the VN100 orientated around its position of rest. As the value wanted is the vertical position of the extra IMU 1 orientated around its own position of rest, the distance between the points of rest must be subtracted.

$$z_{extraIMU1} = \tilde{z}_{extraIMU1} - \Delta z \tag{4.20}$$

$$z_{extraIMU1} = z_{VN100} - sin(pitch)\Delta x + sin(roll)cos(pitch)\Delta y + cos(roll)cos(pitch)\Delta z - \Delta z \tag{4.21}$$

The three unknown parameters in equation 4.21 are the constants Δx, Δy and Δz. These can be approximated from the construction plans of the ship (Underhill, n.d.). As the elements on which the VN100 and the extra IMU 0 are mounted can not to be seen in the construction plans, the thereby determined spatial distances are not exact.

	from VN100 to extra IMU 0	from VN100 to extra IMU 1
Δx_{approx}	4.412 m	19.855 m
Δy_{approx}	0.960 m	-1.918 m
Δz_{approx}	0.979 m	4.816 m

Table 4.5: Distances between the VN100 and the additional IMUs approximated by the ship's construction plans (Underhill, n.d.)

With the spatial distances and equation 4.21, the vertical position of the extra IMU 1 $z_{extraIMU1}$ can be approximated by the vertical position of the VN100 z_{VN100} and the difference in vertical position between these two $z_{approx} \approx z_{extraIMU1} - z_{VN100}$, which is dependant on the pitch and roll values.

$$\begin{aligned} z_{GeoApprox} = &- sin(pitch)\Delta x_{approx} \\ &+ sin(roll)cos(pitch)\Delta y_{approx} \\ &+ (cos(roll)cos(pitch) - 1)\Delta z_{approx} \end{aligned} \tag{4.22}$$

The accuracy of this approximation is tested for the data set from 22.10.2021 to 24.11.2021, when all IMUs were working reliably. The perfect value to be matched is hereby the measured difference in relative vertical position between the IMUs $z_{extraIMU1} - z_{VN100}$. The standard deviation of the error of z_{approx} is given by:

$$\sigma = \sqrt{\frac{\sum_{j=1}^{N}((z_{extraIMU1} - z_{VN100}) - z_{approx})^2}{N}} \tag{4.23}$$

The standard deviation over the data set from 22.10.2021 to 27.10.2021 is calculated to be $\sigma_{GeoApprox} = 0.176$ m

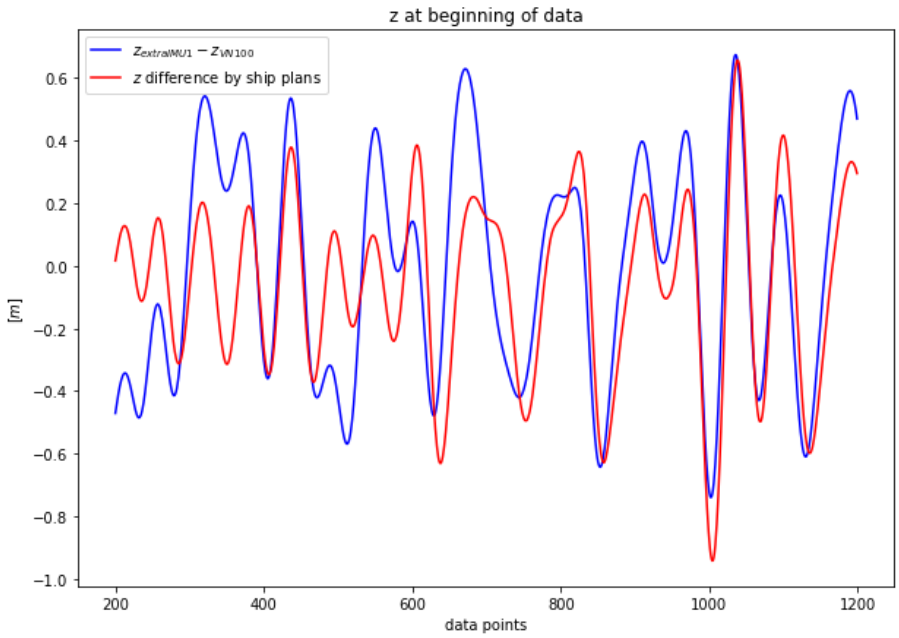

Figure 4.8: Comparison of the measured difference in vertical position between extra IMU 1 and the VN100 to the value gained from the approximation $z_{GeoApprox}$ (equation 4.22), which is based on the ship plans (Underhill, n.d.), for 1000 data points of the the data set from 22.10.2021 to 24.10.2021.

It can be examined by the example of figure 4.8, that $z_{GeoApprox}$ is able to recreate the desired difference in vertical position between the IMUs to some extend. It shows that the approximation follows

the same phase as the desired value, though the amplitude does not always fit. The mismatch may be further evaluated by the frequency of its occurrence. therefore the standard deviation defined by equation 4.23 is applied on the single 30 *min* data files of the data set.

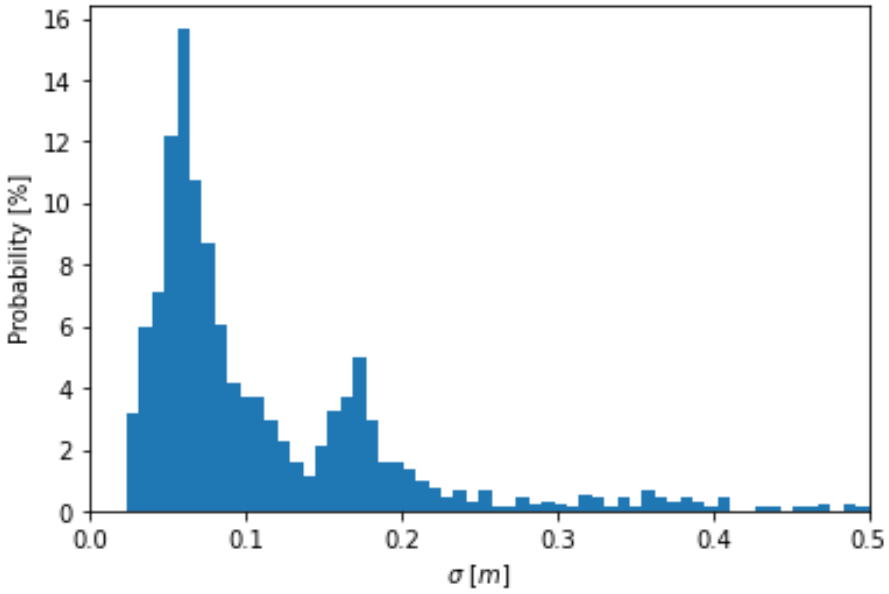

Figure 4.9: Probability of occurrence for different standard error deviations of $z_{GeoApprox}$ over 30 *min* files in the data set from 22.10.2021 to 24.11.2021 with bin-width≈ 0.008 *m*.

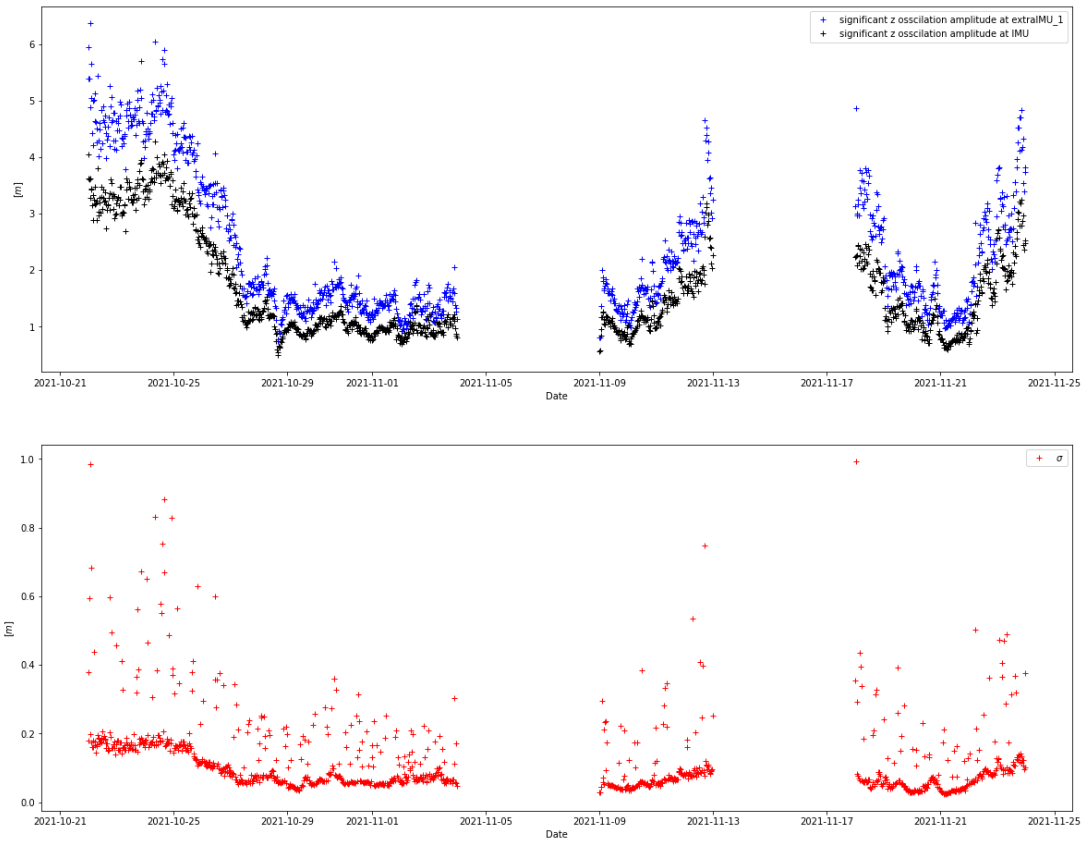

Figure 4.10: Comparison of the significant amplitude of the oscillation in z for the extra IMU 1 and the VN100 (top) to the standard error deviation for $z_{GeoApprox}$ (bottom) over the time span from 22.10.2021 to 24.11.2021

Figure 4.9 shows the probability distribution for the occurrence of standard error deviations of different sizes. It can be seen, that mismatches over 0.25 m are rare and can be categorised as occasional outliers. The two peaks in figure 4.9 might indicate a dependence of the approximation on the ships state of motion. Figure 4.10 shows that the standard deviation of the error of $z_{GeoApprox}$ is proportional to the significant amplitude of the oscillation of the vertical positions of the IMUs, defined as:

$$Z_s = 4\sqrt{\frac{\sum_{j=1}^{N} z^2}{N}} \tag{4.24}$$

This definition for the significant amplitude of the oscillation of the vertical position is chosen as an analogy to the definition of the significant wave height SWH (equation 4.46), as the oscillation of the ship is mainly wave induced. Figure 4.10 shows that the standard error deviation of $z_{GeoApprox}$ is relative to Z_s.

To gain the exact spatial distances, the advantage shall be exploited, that all time derivatives of z are available,because the measured instance is $\ddot{z}$. As the spatial distances are the unknowns in equation 4.21, while all other variables are known from measurements, three unknowns are present in the equation. therefore two more equations are needed to solve the system for all three unknowns. The idea is to take the first and second time derivative of equation 4.21 and thereby derive three linear independent equations to solve for the three unknown spatial distances for each single data point. It is expected that the gained spatial distances may vary between the data points and that the real distances may be gained as a mean over the data points. The three equations forming the equation system are:

$$z_{extraIMU1} = z_{VN100} + \begin{pmatrix} -sin(p) & sin(r)cos(p) & cos(r)cos(p) - 1 \end{pmatrix} \Delta\vec{x}_{extraIMU1} \tag{4.25}$$

$$\dot{z}_{extraIMU1} = \dot{z}_{VN100} + \begin{pmatrix} -cos(p)\dot{p} & cos(r)\dot{r}cos(p) & -sin(r)\dot{(r)}cos(p) \\ & -sin(r)sin(p)\dot{p} & -cos(r)sin(p)\dot{p} \end{pmatrix} \Delta\vec{x}_{extraIMU1} \tag{4.26}$$

$$\ddot{z}_{extraIMU1} = \ddot{z}_{VN100} + \begin{pmatrix} & cos(r)\ddot{r}cos(p) & 2sin(r)\dot{r}sin(p)\dot{p} \\ sin(p)\dot{p}^2 & -sin(r)\dot{r}^2cos(p) & -cos(r)\dot{r}^2cos(p) \\ -cos(p)\ddot{p} & -2cos(r)\dot{r}sin(p)\dot{p} & -sin(r)\ddot{r}cos(p) \\ & -sin(r)cos(p)\dot{p}^2 & -cos(r)cos(p)\dot{p}^2 \\ & -sin(r)sin(p)\ddot{p} & -cos(r)sin(p)\ddot{p} \end{pmatrix} \Delta\vec{x}_{extraIMU1} \tag{4.27}$$

Hereby r denotes the roll and p denotes the pitch. The vector $\Delta\vec{x}_{extraIMU1}$ is defined by equation 4.13. The time derivatives of pitch, roll and z are computed in Fourier space, as it is described in section 4.1.4. As pitch and roll are known, the row vectors contain known scalars for each data point and can be combined to a coefficient matrix C for each data point. The equation system for each data point is then linear and given by:

$$C\Delta\vec{x}_{extraIMU1} = \begin{pmatrix} z_{extraIMU1} - z_{VN100} \\ \dot{z}_{extraIMU1} - \dot{z}_{VN100} \\ \ddot{z}_{extraIMU1} - \ddot{z}_{VN100} \end{pmatrix} \tag{4.28}$$

When solving the equation system 4.28 for each data point, the values gained for the spatial distances differ extremely from point to point. The variance is large and the distances gained by taking the mean over all the distances from each single data point are unrealistic, as they lie outside of the ship's hull. This approach for finding the spatial distances between the IMUs is therefore discarded.

Function Fitting Approach

An alternative approach for finding the spatial distances between the IMUs is the application of a function fitting algorithm. The algorithm takes equation 4.21 as a function dependant on pitch, roll and z_{VN100} with Δx,Δy and Δz as coefficients that shall be determined. The algorithm determines the coefficients, which result in the best fitting approximation to the measured values of $z_{extraIMU1}$. The best fit is hereby defined as the minimal quadratic error sum between the measured $z_{extraIMU1}$ and the approximated z. The approximated spatial distances, gained from the ship's construction plans (table 4.5) hereby serve as

initial guesses for the coefficients.
The spatial distances Δx,Δy and Δz gained from this method are again not reasonable as they do not lie close to the approximated ones and Δz even has an opposite sign of the expectations.
The idea to find a definition for the motion of extra IMU 1 by the data from the VN100 and the geometrical relationship between the sensors is not longer followed, as its maximal accuracy is limited to the spatial distances between the sensors approximated from the ships construction plans, because no correction for the approximated values can be found from the measured data. It might be, that the failure of this analytical method is based on noise in either the VN100's measurements or the data gained from the extra IMU 1, which prevents a precise fit for the geometrical distances looked for.

As the geometrical approach to find a calculation method for the position of the extra IMU 1 by the data from the VN100 can not be conducted beyond the precision of the approximated geometric distances between the IMUs, it is tried to use the function fit algorithm to determine a calculation method by fitting other selected functions to the data measured by the VN100 and the extra IMU 1. The input parameters are hereby pitch, roll and z_{VN100}, while the output parameter shall be z_{approx}, which is defined as the difference in relative vertical position between the VN100 and the extra IMU 1 so that $z_{VN100} + z_{approx} \approx z_{extraIMU1}$.
Multiple functions have been tested or experimented with ranging from simple sines and polynomials to nonlinear combinations of trigonometrical and polynomial terms. The function with a best result is given by a linear combination of all possible multiplications of $cos(pitch)$, $sin(pitch$, $cos(roll)$ and $sin(roll)$.

$$\begin{aligned} z_{TrigApprox} =& c_0 sin(p) + c_1 cos(p) + c_2 sin(r) + c_3 cos(r) \\ &+ c_4 sin^2(p) + c_5 sin(p)cos(p) + c_6 sin(p)sin(r) + c_7 sin(p)cos(r) \\ &+ c_8 cos^2(p) + c_9 cos(p)sin(r) + c_{10} cos(p)cos(r) + c_{11} sin^2(r) \\ &+ c_{12} sin(r)cos(r) + c_{13} cos^2(r) + c_{14} z_{VN100} + c_{15} \end{aligned} \tag{4.29}$$

The multiplication of sin and cos terms is chosen because of the occurrence of such terms in the rotational matrix in equation 4.18, that describes the geometrical relationship between the vertical positions of the IMUs. The term $c_{14} z_{VN100}$ is integrated to compensate for a possible difference between the IMUs data, that is dependant on the amplitude of z, and c_{15} is integrated to compensate for a possible offset.
The values found by the function fitting algorithm are given in table 4.6:

constant	value determined by algorithm
c_0	$-2.36110177 \cdot 10^{+01}$
c_1	$5.75988174 \cdot 10^{+04}$
c_2	$5.79281452 \cdot 10^{+02}$
c_3	$2.28212869 \cdot 10^{+04}$
c_4	$-4.49619468 \cdot 10^{+03}$
c_5	$1.42082453 \cdot 10^{+00}$
c_6	$-8.75471293 \cdot 10^{+00}$
c_7	$3.29953406 \cdot 10^{+00}$
c_8	$-2.22659342 \cdot 10^{+04}$
c_9	$-5.68242427 \cdot 10^{+02}$
c_{10}	$-2.21480822 \cdot 10^{+04}$
c_{11}	$-1.12570715 \cdot 10^{+04}$
c_{12}	$-1.23549227 \cdot 10^{+01}$
c_{13}	$-1.15889189 \cdot 10^{+04}$
c_{14}	$-3.58857334 \cdot 10^{-02}$
c_{15}	$-2.44171350 \cdot 10^{+04}$

Table 4.6: Coefficients for the Trigonometry Approximation (equation 4.29) determined by a function fitting algorithm with data from 22.10.2021 to 24.11.2021 used for the fit.

The standard error deviation to the measured value over the data set from 22.10.2021 to 24.11.2021, defined in equation 4.23, is 0.167 m.

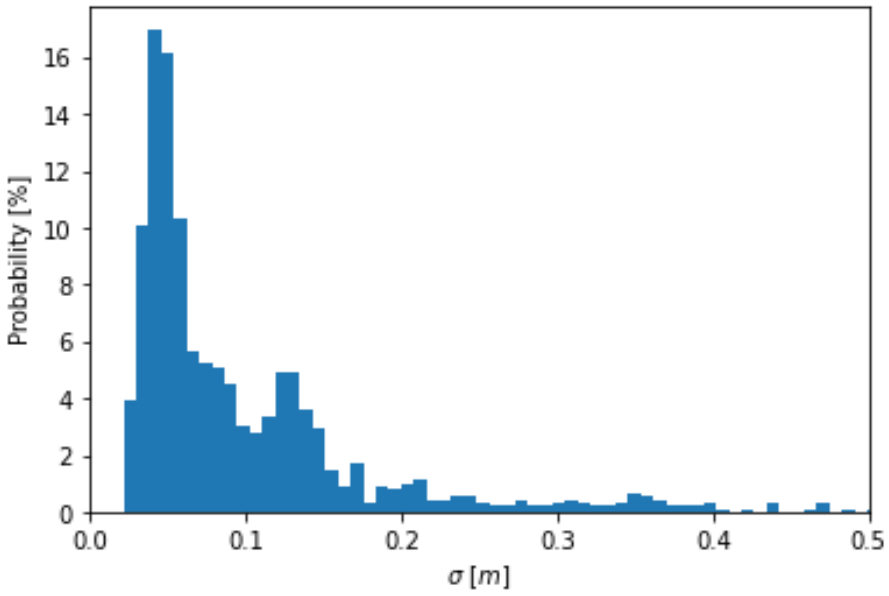

Figure 4.11: Probability of occurrence for different standard error deviations of $z_{TrigApprox}$ over 30 min files in the data set from 22.10.2021 to 24.11.2021 with bin-width$\approx$ 0.008 m.

By comparison of figure 4.11 with figure 4.9 can be seen, that the approximation based on the fitted function has a lower error than the approximation based on the ship's geometry. Again two peaks can be seen in figure 4.11, as already in figure 4.9.

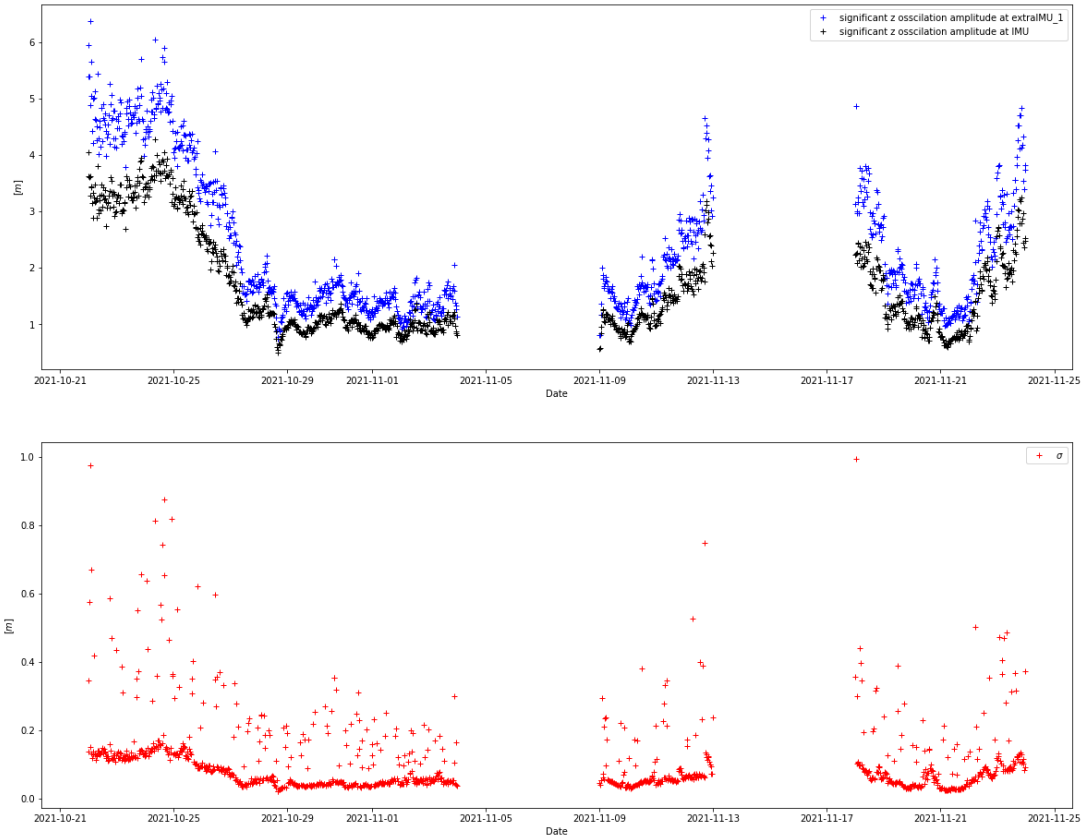

Figure 4.12: Comparison of the significant amplitude of the oscillation in z for the extra IMU 1 and the VN100 (top) to the standard error deviation for $z_{TrigApprox}$ (bottom) over the time span from 22.10.2021 to 24.11.2021.

Figure 4.12 shows, that the standard error deviation of $z_{TrigApprox}$ follows the same trend as the significant amplitudes of oscillation Z_s of the IMUs, as it is also the case for $z_{GeoApprox}$ in figure 4.10.

Though this approximation delivers the best fit, a function with less coefficients of lower order is wanted, as it is questionable, whether this function will also give adequate values outside the training data set, because some coefficients contribute at a high order (see table 4.6). Especially the high value of the constant c_{15} arises the doubt, that a function with that many constants might be over-fitted.
Therefore, a more simpler approach for an approximation function is chosen, which is only consisting of the possible basic trigonometrical terms $cos(pitch)$, $sin(pitch)$, $cos(roll)$ and $sin(roll)$ and a term linear in z_{VN100}.

$$z_{SimpleTrigApprox} = c_0 sin(p) + c_1 cos(r) + c_2 cos(p) + c_3 sin(r) + c_4 z_{VN100} \tag{4.30}$$

The coefficients found by the function fitting algorithm are given in table 4.7.

constant	value determined by algorithm
c_0	-18.68128014
c_1	13.61833253
c_2	-13.57785234
c_3	-1.21498561
c_4	-0.03734729

Table 4.7: Coefficients for the Simple Trigonometry Approximation (equation 4.30) determined by a function fitting algorithm with data from 22.10.2021 to 24.11.2021 used for the fit.

The standard error deviation over the data set from 22.10.2021 to 24.11.2021, defined in equation 4.23, is 0.167 m.

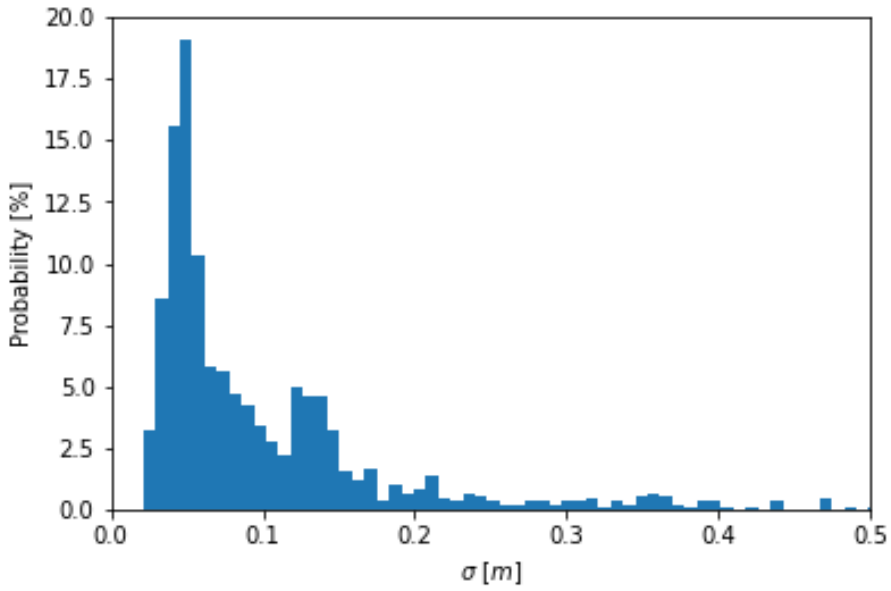

Figure 4.13: Probability of occurrence for different standard error deviations of $z_{SimpleTrigApprox}$ over 30 min files in the data set from 22.10.2021 to 24.11.2021 with bin-width≈ 0.008 m.

Figure 4.13 shows, that the simple trigonometrical approximation features errors comparable to the longer trigonometrical approximation (see figure 4.11). Therefore the simple trigonometrical approximation ($z_{SimpleTrigApprox}$, equation 4.30, table 4.7) is considered to be the best approach so far and shall be used to estimate the difference in vertical position between the extra IMU 1 and the VN100.

$$z_{extraIMU1} \approx z_{VN100} + z_{SimpleTrigApprox} \tag{4.31}$$

For the ultrasonic probe 2 and the radar probe, located in the same position, the same method is applied, using data from the extra IMU 0. The respective coefficients for the Short Trigonometry Approximation are given in table 4.8)

constant	value determined by algorithm
$c0$	3.84804107
$c1$	5.25491401
$c2$	−5.24400568
$c3$	−0.20843634
$c4$	−0.01711533

Table 4.8: Coefficients for the Simple Trigonometry Approximation (equation 4.30) to the position of extra IMU 0 determined by a function fitting algorithm with data from 22.10.2021 to 24.11.2021 used for the fit.

Figure 4.14 shows, that the standard error deviation for the fit to the position of extra IMU 0 is generally lower, than for the fit to the position of extra IMU 1. This was expected, as the extra IMU 0 is located closer to the VN100 than the extra IMU 1.

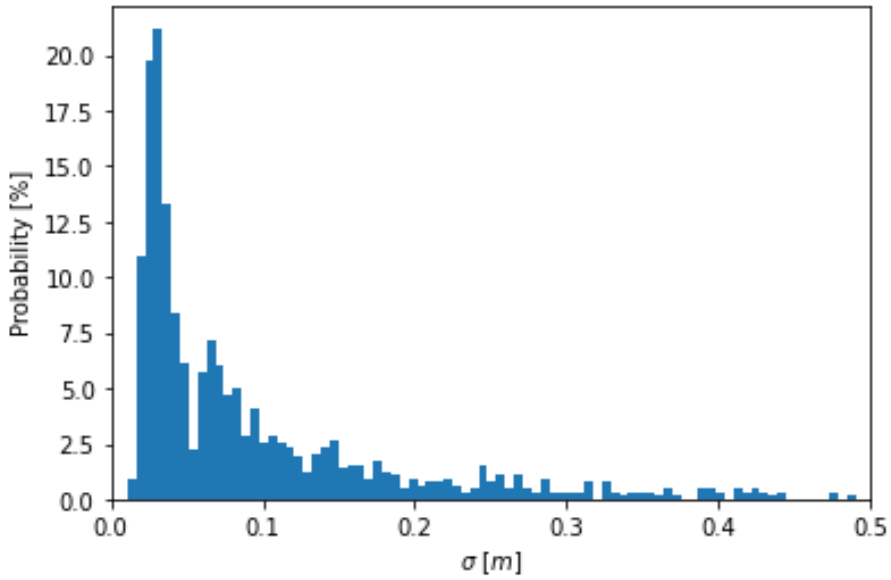

Figure 4.14: Probability of occurrence for different standard error deviations of $z_{SimpleTrigApprox}$ for the position of extra IMU 0 over 30 min files in the data set from 22.10.2021 to 24.11.2021 with bin-width$\approx 0.008\ m$.

Evaluation of Approximation Failure

To examine the cases in which the short trigonometry approximation $z_{SimpleTrigApprox}$ for the difference in vertical position between the IMUs fails critically, the largest discrepancy between the approximated vertical position of the extra IMU 1 and the measured value $z_{extraIMU_0}$ is viewed upon in figure 4.15.

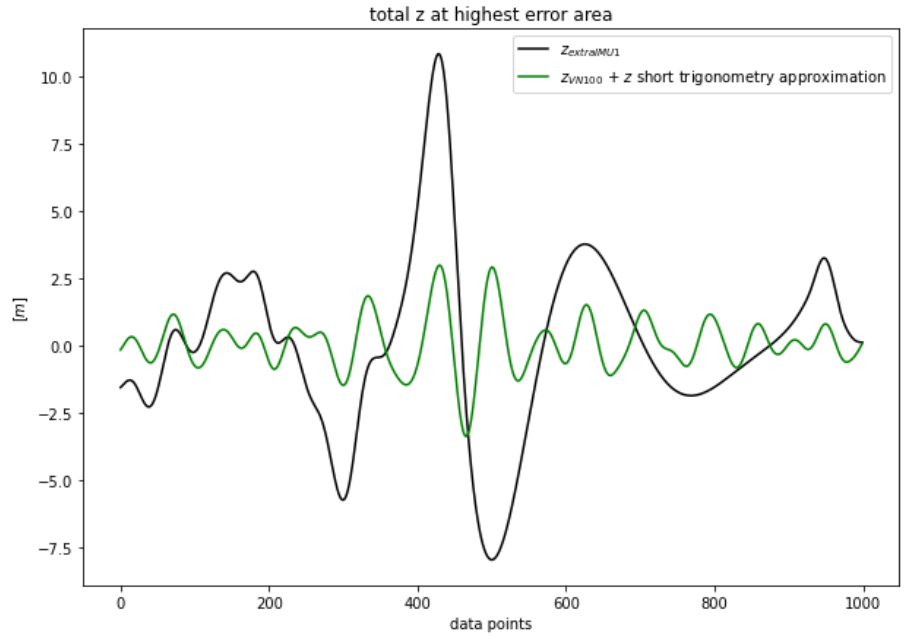

Figure 4.15: Maximal discrepancy between the vertical position at the extra IMU 1 gained from the short trigonometrical approximation $z_{VN100} + z_{SimpleTrigApprox}$ and the measured value $z_{extraIMU1}$ for the data set from 22.10.2021 to 24.11.2021.

It can be seen in figure 4.15, that the error is based on a major discrepancy in the measurements of the VN100 and the extra IMU 1. The difference in the vertical position of the extra IMU 1 $z_{extraIMU1}$ and the VN100 z_{VN100} suggest, that the data measured by one of the IMUs is wrong. The vertical positions of the IMUs are related by equation 4.21. By this not only the amplitude difference seen in figure 4.15 could only be caused by an unrealistic motion of the ships body, but the phase difference is mere impossibly by geometrical means. Also, investigation of the maximal errors of other approximations shows, that for all approximation methods the point of maximal error is the one depicted in figure 4.15, and that the differences between the approximated vertical positions are minimal compared to the error itself. From this follows, that the error does not result from the approximation. It is therefore deducted, that the vertical position measured by the extra IMU 1 $z_{extraIMU1}$ is wrong. This is further supported by the fact, that the amplitude in the oscillation of $z_{extraIMU1}$, as it is seen in figure 4.15 could only have been caused by waves of an enormous size, which didn't occur in the period of the data set from 22.10.2021 to 24.11.2021.

Although only the case of the highest error is shown here, the cases for the second, third and fourth highest error in the data set are similar. All these cases occurred on different dates and are therefore not from the same files. It is therefore deducted, that high discrepancies between the approximated vertical position of the extra IMU 1 $z_{VN100} + z_{approx}$ and the measured vertical position $z_{extraIMU1}$ are based on false data measured by the extra IMU 1, rather than deficiencies of the approximation. Even though a standard error of about 0.1 m between the approximation and the measured vertical position exists, as it is discussed previously in this section, the method using the data from the VN100 and the approximation seems to be more robust towards larger outliers than the vertical position measured by the extra IMU 1 itself. therefore the data from the VN100 and the short trigonometrical approximation $z_{SimpleTrigApprox}$ (equation 4.30) are used to gain the vertical positions of the altimeter probes, even for the times when data from the extra IMUs is available.

4.2 Calculation of the Water Surface Elevation and Wave Properties

4.2.1 Calculation of the Water Surface Elevation η

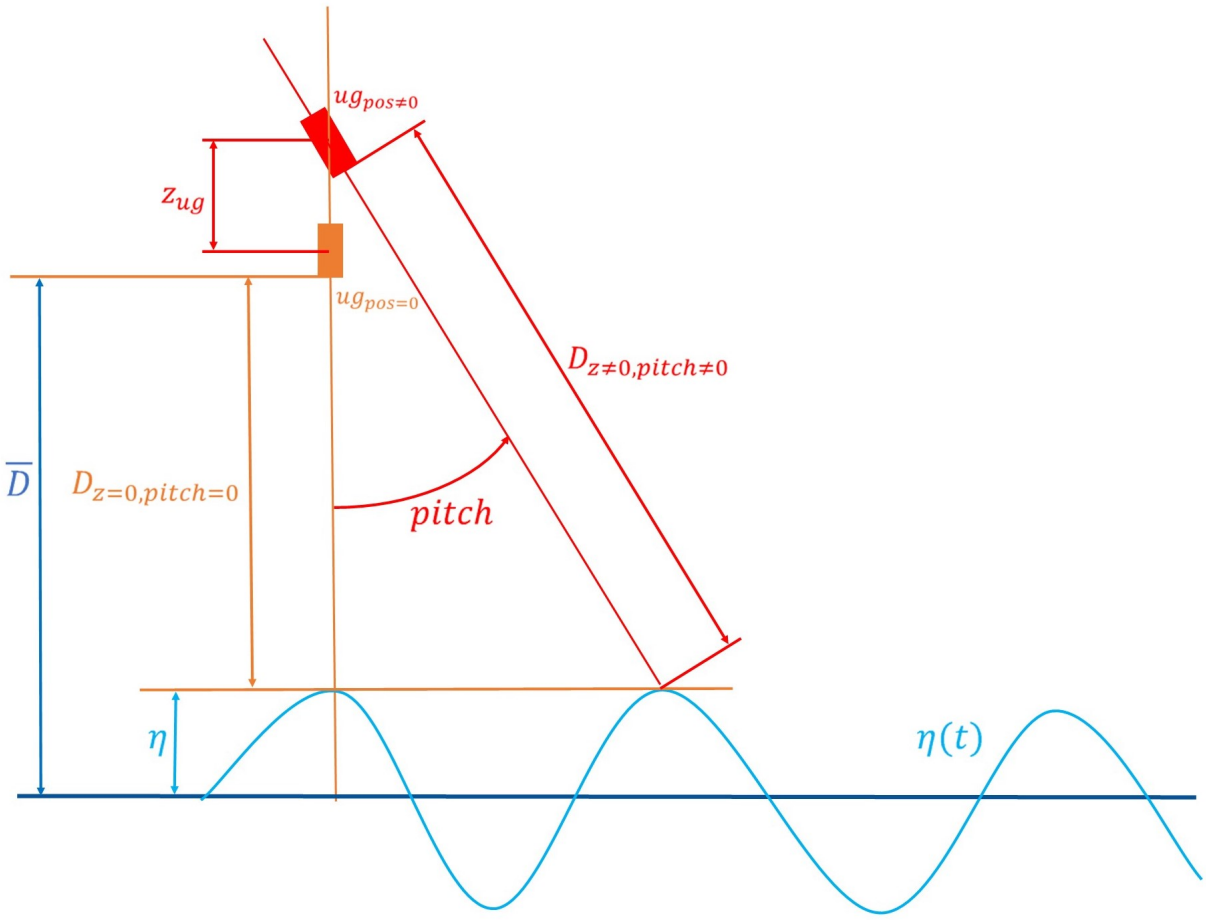

Figure 4.16: Schematics for the calculation of the water surface height by the example of an ultrasonic gauge (ug)

For a altimeter probe, the water surface height η over the time could be directly gained by subtraction of the measured distance between the gauge and the water surface $D_{pos=0}$, from the mean value of the distances measured over time $\overline{D}$ (see figure 4.16). This is the principle followed by Løken et al. (2021).

$$\eta = \overline{D} - D_{pos=0} \tag{4.32}$$

Alternatively, the position of the water surface height by means of a coordinate system not based on the water surface, but the location of the probe, $\eta_{ug=\vec{0}}$ is given by the measured distance from the probe and a sign change. The water surface elevation η can then be gained by subtracting the mean. This way is chosen by Christensen et al. (2013).

$$D_{pos=0} = -\eta_{ug=\vec{0}} \tag{4.33}$$

$$\eta = \eta_{ug=\vec{0}} - \overline{\eta_{ug=\vec{0}}} \tag{4.34}$$

Both definitions are exchangeable and by mathematical means identical as equation 4.33 substituted into equation 4.34 equals equation 4.32. A difference in both definitions occurs only if the time intervals over which the means are taken differ. While $\overline{D}$ is defined to be the distance at which the probe is mounted over a calm water surface, the mean over the signal $\overline{\eta_{ug=\vec{0}}}$ is taken over the length of one data file of 30 min. If the ship has a steady heel over the duration of a data file, due to its course to the wind, $-\overline{\eta_{ug=\vec{0}}}$ does not equal $\overline{D}$ anymore. Therefore the second definition, given by equation 4.33 and 4.34, is chosen for the computation of η, as this compensates for possible offsets and guarantees an oscillation of

the water surface height η around 0.

As the ship is subject to constant motion due to the influence of the waves on the hull, the position of the altimeter probe cannot be assumed to be steady. Therefore the influence on the measured distance $D_{pos\neq0}$, which results from the ship's motion and not from a change in the water surface height, must be compensated for. The three degrees of freedom which influence the distance, measured by the probe, are the vertical position in relation to its steady state z_{ug}, the pitch and the roll.
The vertical position of the probe is gained from the approximation of the vertical position of the extra IMU by the data from the VN100 and an additional term for the spatial distance between the extra IMU and the probe. As the ultrasonic gauge 1 is mounted midships approximately 0.5 m in front of the extra IMU 1 and at the same height, the additional term for the ultrasonic gauge 1 becomes:

$$z_{extraIMU1\rightarrow ug1} = 0.5\ m\ \cdot\ sin(-pitch) \tag{4.35}$$

As the radar probe and the ultrasonic gauge 2 are mounted approximately 0.5 m above the extra IMU 0 in the same horizontal position, the additional term for them becomes:

$$z_{extraIMU0\rightarrow ug2} = z_{extraIMU0\rightarrow radar} = 0.5\ m\ \cdot\ cos(pitch)cos(roll) \tag{4.36}$$

The vertical position of any of the altimeter probes is thus given as:

$$z_{probe} = z_{VN100} + z_{SimpleTrigApprox(probe)} + z_{extraIMU0\rightarrow probe} \tag{4.37}$$

Whereas $z_{SimpleTrigApprox}$ is defined by equation 4.30 and table 4.7 or table 4.8, depending on the probe (section 4.1.5).

As it can be seen in figure 4.16, the distance measured by the probe $D_{pos\neq0}$ is the hypotenuse of an orthogonal triangle. The hypothetical steady state distance $D_{pos=0}$ plus the vertical position of the probe z_{ug} is the side adjacent to the pitch angle. Figure 4.16 is a two dimensional illustration in the x-z-plane. The same triangle can be found in the y-z-plane with the roll instead of the pitch. The trigonometrical relations of the orthogonal triangle give:

$$\frac{D_{pos=0} + z_{ug}}{D_{pos\neq0}} = cos(pitch)cos(roll) \tag{4.38}$$

$$D_{pos=0} = -z_{ug} + D_{pos\neq0}cos(pitch)cos(roll) \tag{4.39}$$

Inserting the definitions from equation 4.33 and 4.34 for $D_{pos=0}$ gives:

$$\eta = z_{ug} - D_{pos\neq0}cos(pitch)cos(roll) - \overline{z_{ug} - D_{pos\neq0}cos(pitch)cos(roll)} \tag{4.40}$$

Equation 4.40 matches the definition given by Christensen et al. (2013). In the practical realisation, $D_{pos\neq0}$ is the distance measured by the probe, while pitch and roll are taken from the data measured by the VN100, as they are the same for all positions on the ship's geometry. An example for the relation between the vertical sensor position, the measured distance (here subtracted with the mean distance for better comparability) and the resulting water surface height η is shown in figure 4.17.

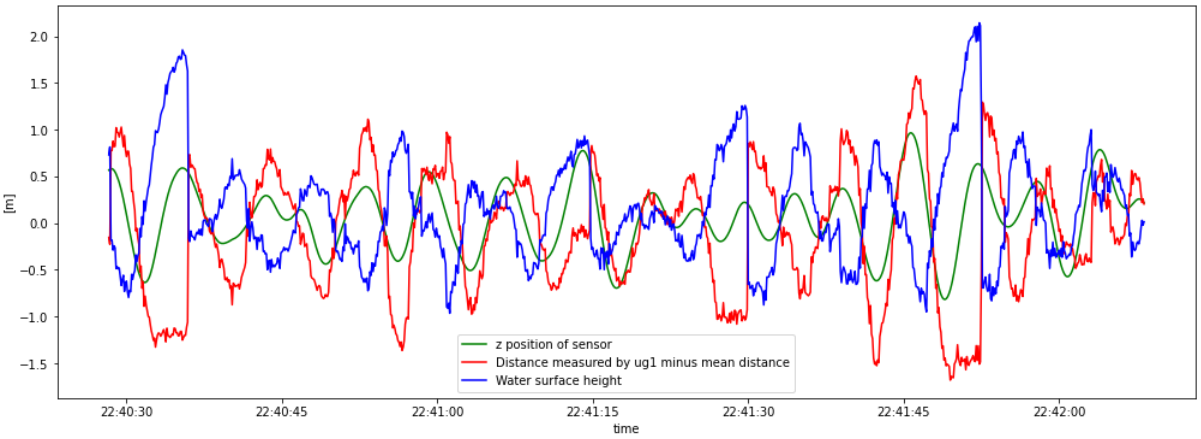

Figure 4.17: Example for water surface height η, vertical sensor position z and measured distance subtracted with the mean distance for the ultrasonic probe 1 from 10.11.2021.

4.2.2 Spectral Analysis of the Wave Signal

The spectral analysis of the wave signal, given by the time series of the water surface elevation η from section 4.2.1, is based on the Power Spectral Density (PSD) evaluation of the wave signal. The Power Spectral Density is obtained by Welch's method (Welch, 1967) and applied on the data files of 30 min length. The window function used for sampling the signal is a Hamming window. Segments are chosen with an overlap of 90 %. The segment size is by default chosen to be 180 s which corresponds to 1800 data points at the used sampling rate of 10 Hz.

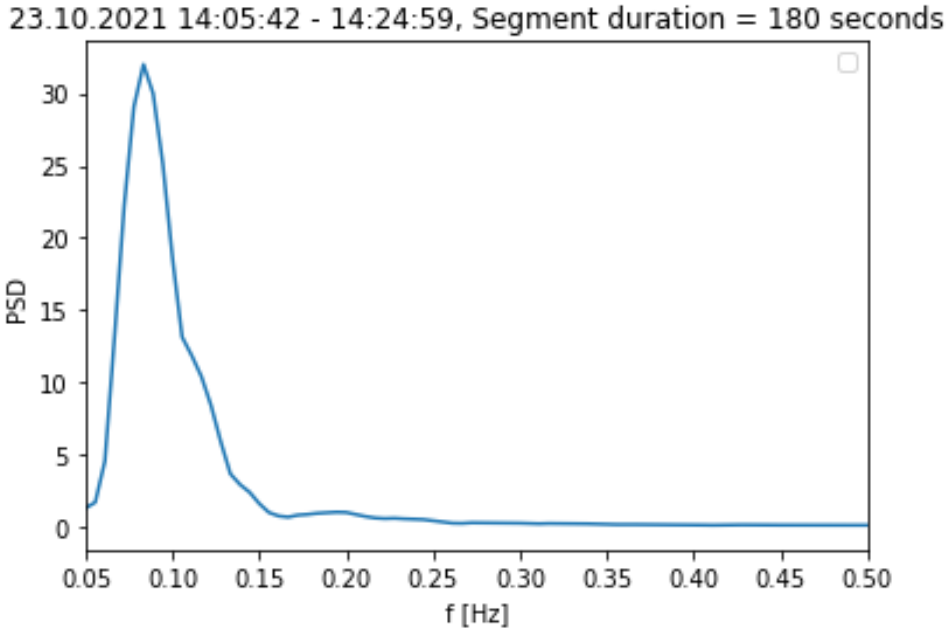

Figure 4.18: Example for a PSD from 23.10.2021 14:00

The peak period of the waves T_p follows the definition of Bidlot (2016) and is given by the reciprocal of the peak frequency, which is the frequency at the maximum of the PSD (see figure 4.18).

$$T_p = \frac{1}{f(max(PSD))} \tag{4.41}$$

From the PSD the spectral moments can be gained as in Løken et al. (2021):

$$m_j = \int_{f_{min}}^{f_{max}} f^j PSD(f) df \tag{4.42}$$

Like in Løken et al. (2021), a minimal frequency f_{min} and a maximal frequency f_{max} are defined to exclude higher frequency noise or lower frequency influence from drifts in the IMU data. The frequency interval is chosen to be $f_{min} = 0.05\ Hz$ and $f_{max} = 0.5\ Hz$, as this is the expected frequency of the waves, this study is interested in (Løken et al., 2021).
From the spectral moments m_j, other periods can be gained from the wave spectrum, like the energy mean wave period $T_{-1/0}$ (Bidlot, 2016) the mean period of the waves $T_{0/1}$ (Holthuijsen, 2007) and the mean zero crossing period $T_{0/2}$ (Holthuijsen, 2007).

$$T_{-1/0} = \frac{m_{-1}}{m_0} \tag{4.43}$$

$$T_{0/1} = \frac{m_0}{m_1} \tag{4.44}$$

$$T_{0/2} = \sqrt{\frac{m_0}{m_2}} \tag{4.45}$$

The spectral moment of zeroth order m_0 is further used in a definition of the significant wave height H_s in equation 4.47.
The definition for the mean zero crossing period given in equation 4.45 is an often used statistical alternative to the original definition. The original mean zero crossing period T_{zc} is defined as the mean of the time durations between two upward (or downward) crossings over zero of the water surface elevation signal η (Holthuijsen, 2007) (see figure 4.20). The original mean zero crossing period T_{zc}can be easily computed directly from the water surface elevation signal η.

4.2.3 The Significant Wave Height

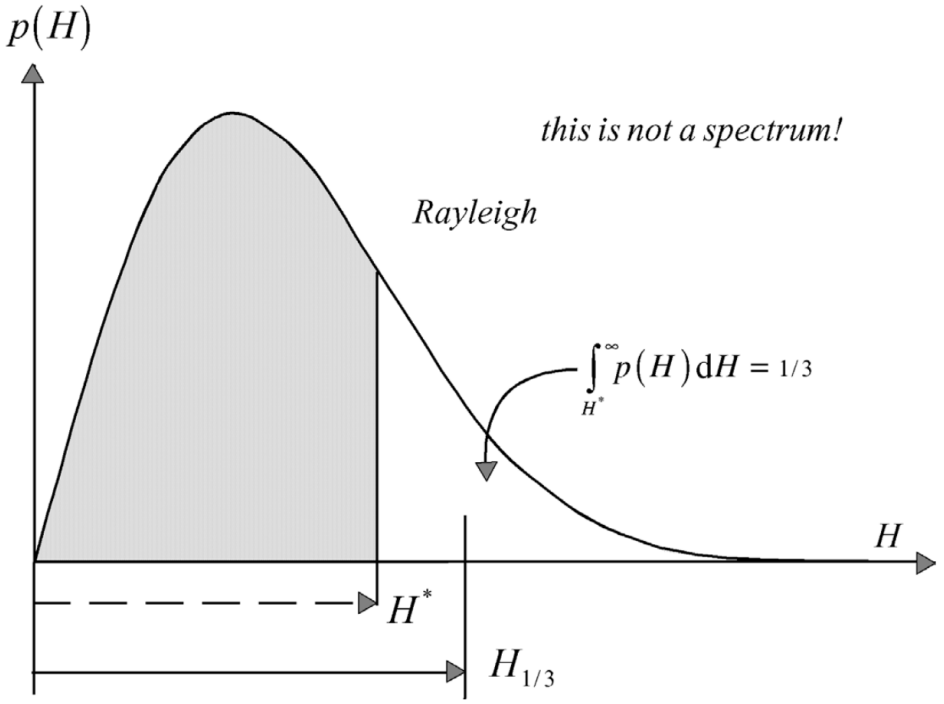

Figure 4.19: *The significant wave height in the Rayleigh probability density function* (Holthuijsen, 2007).

The significant wave height $H_{1/3}$ is defined as the mean of the highest third of wave heights occurring in the observed time period (Holthuijsen, 2007). As this exact definition can be hard to realise in a practical way, most often other definitions are used as a substitute. Under the assumption that the probability function of the occurring wave heights resembles a Rayleigh Distribution (see figure 4.19), approximations for the significant wave height $H_{1/3}$ can be found by usage of the root-mean-square wave height H_{rms} or the zeroth spectral moment m_0 (Holthuijsen, 2007). The latter can be gained from an analysis of the wave spectrum as it is described in section 4.2.2 and is defined by equation 4.42.
The significant wave height defined by the root-mean-square wave height is the one used by Christensen et al. (2013) (SWH), the WAM model described by Bidlot (2016) uses the definition based on the zeroth spectral moment H_s. Løken et al. (2021) refers to both definitions.
Following Løken et al. (2021)'s notation, the significant wave height given based on the root-mean-square $\sigma(\eta)$ shall be denoted as SWH, while the significant wave height based on the zeroth spectral moment is denoted as H_s

$$SWH = 4\sigma(\eta) = 4\sqrt{\frac{1}{N}\sum_{j=1}^{N}\eta_j^2} \tag{4.46}$$

$$H_s = 4\sqrt{m_0} \tag{4.47}$$

The original definition of the significant wave height $H_{1/3}$, as the mean of the highest third of the waves, shall also be computed. It is used as a comparison value for the case, that the assumption of Rayleigh

distributed wave heights might be wrong. The difficulty with this definition is to determine the wave heights. It has to be decided how a single wave height shall be determined in the data processing, as a wave might consist of multiple peaks. It is therefore decided, that one wave shall be determined by the interval between two zero-up-crossings, meaning between two events when the water surface elevation signal η switches sign from negative to positive.

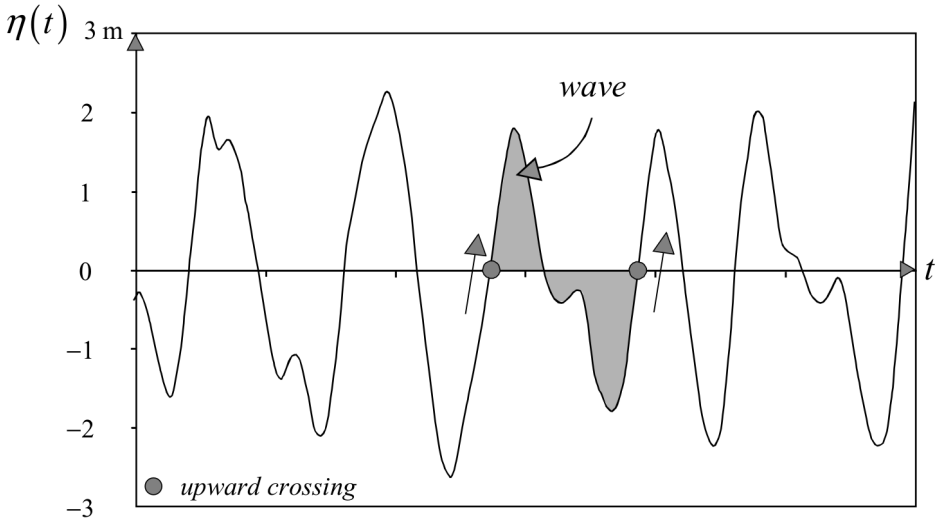

Figure 4.20: *The definition of a 'wave' in a time record of the surface elevation with upward zero-crossings* (Holthuijsen, 2007).

This definition of a wave, which is illustrated in figure 4.20, is taken from Holthuijsen (2007). The wave peak is found by the maximum of the water surface elevation signal of a wave and the trough by its minimum. The wave height is defined as $H_{wave} = \eta_{peak} - \eta_{trough}$. The wave heights found in a data file are sorted and the mean of the highest third is computed to get the significant wave height $H_{1/3}$.

4.3 Correction for the Doppler Effect

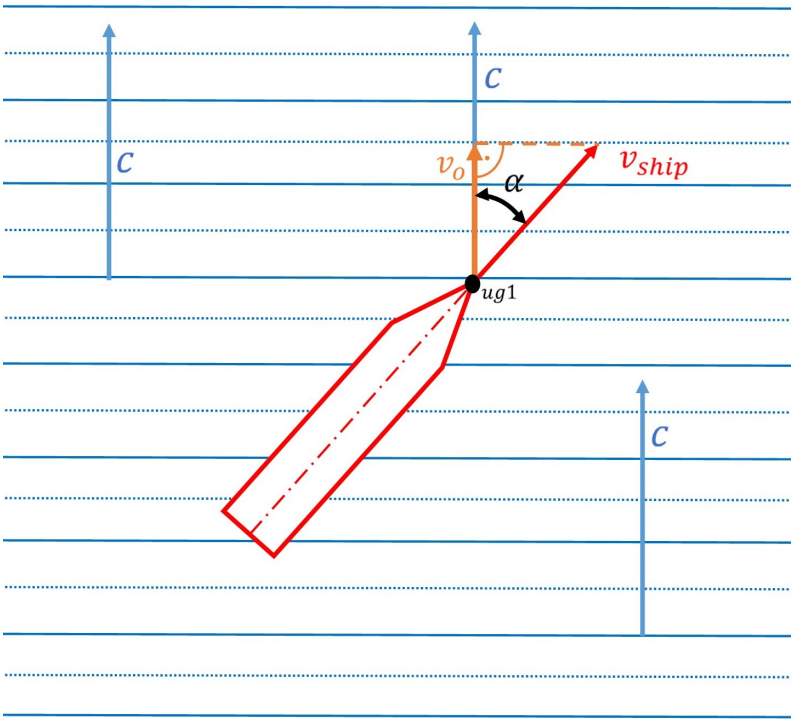

Figure 4.21: Schematic illustration of the velocity components causing the Doppler Effect on the measured wave data.

As the ship is not sailing perpendicular to the direction of the waves, the wave spectrum measured by the probes is subject to the Doppler Effect, caused by the ship's velocity component, along the waves' propagation direction (see figure 4.21). The PSD gained from the water surface elevation signal η in section 4.2.2 therefore doesn't resemble the real spectrum of the waves. To compensate for this , a correction for the influence of the Doppler Effect is needed.
For a sender, sending out a signal of a certain frequency and an observer, which both move in the same direction, the relation between the frequency registered by the observer and the frequency emitted by the sender is given as:

$$f_0 = f_s \left(\frac{c - v_o}{c - v_s} \right) \tag{4.48}$$

Hereby, f denotes the frequency, s the sender, o the observer, v the velocity and c the signal propagating velocity. As the waves travelling over the sea are not caused by a distinct sender, the velocity of the sender is set to zero $v_s = 0$ for the inspected case. The signal propagation velocity c is the phase velocity of the the surface gravity waves. As c is not known from measurements, it is assumed by usage of the dispersion relation for linear waves, defined in Newman (2018).

$$c = \frac{g}{\omega_s} \tag{4.49}$$

Hereby g denotes the gravitational constant and w_s is the angular frequency of the waves, which relates to the wave frequency $\omega_s = 2\pi f_s$. The dispersion relation for linear waves is used even though the measured waves might resemble Stokes waves, as the waves steepness needed to determine the phase velocity of Stokes waves (Newman, 2018) can hardly be evaluated from the measured water surface elevation signal η . Equation (4.48) can be rewritten to:

$$f_o = f_s \left(\frac{\frac{g}{2\pi f_s} - v_o}{\frac{g}{2\pi f_s}} \right) \tag{4.50}$$

The observed f_o is the one gained from the measurements and known. The frequency of the incoming waves f_s is the parameter that shall be determined. Equation 4.50 is therefore rearranged to f_s.

$$\begin{aligned} f_o &= f_s \left(1 - \frac{2\pi f_s v_o}{g}\right) \\ &= f_s - \frac{2\pi v_o}{g} f_s^2 \end{aligned} \tag{4.51}$$

$$f_s^2 - \frac{g}{2\pi v_o} f_s + \frac{g}{2\pi v_o} f_o = 0 \tag{4.52}$$

As f_o is known, two solutions can be gained for f_s from equation (4.52) by usage of the p-q-formula.

$$\begin{aligned} f_{s+,s-} &= \frac{g}{4\pi v_o} \pm \sqrt{\frac{g^2}{16\pi^2 v_o^2} - \frac{g}{2\pi v_o} f_o} \\ &= \frac{g}{4\pi v_o} \pm \sqrt{\frac{g}{2\pi v_o}\left(\frac{g}{8\pi v_o} - f_o\right)} \end{aligned} \tag{4.53}$$

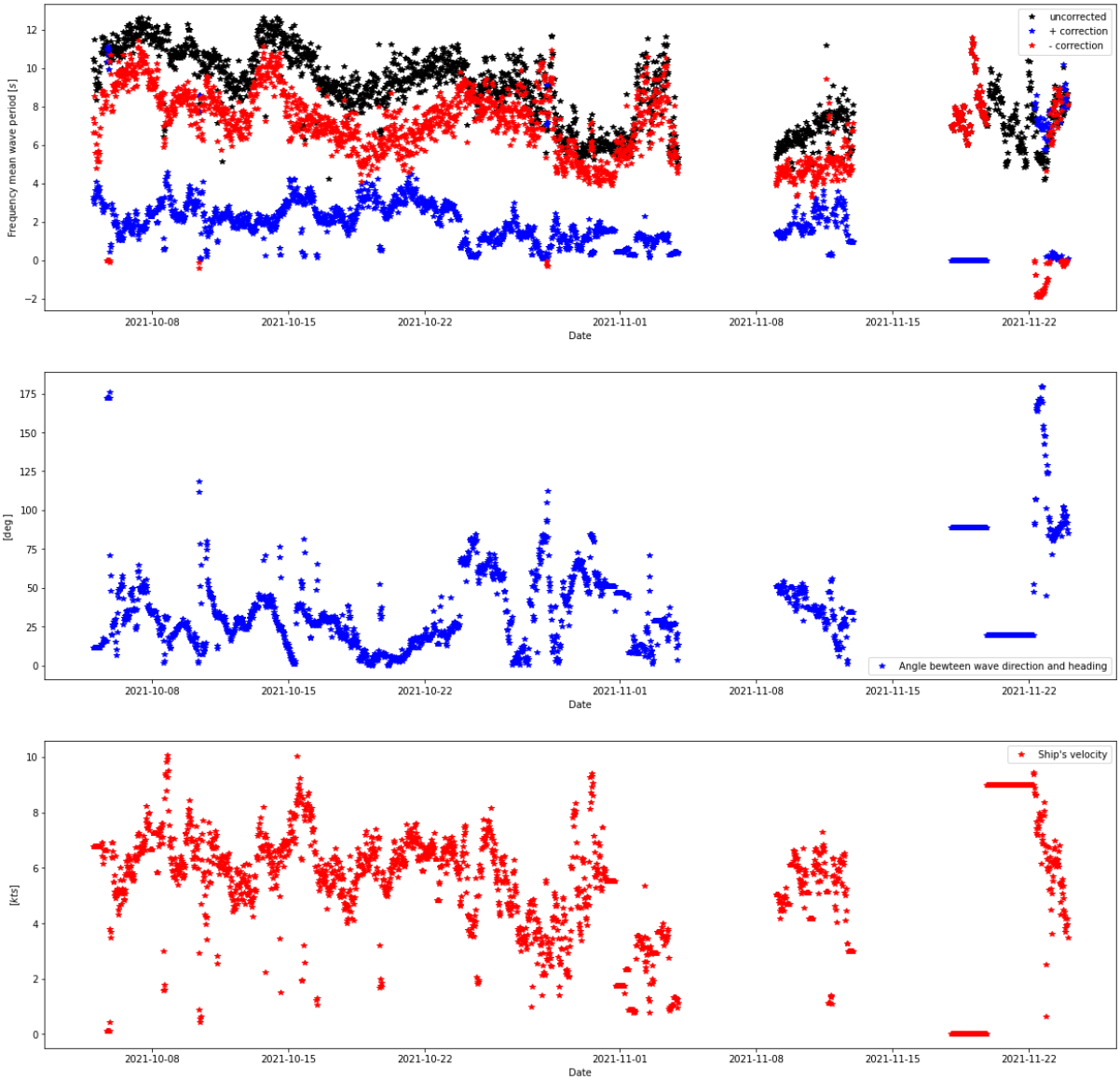

Figure 4.22: Comparison of the mean wave period $T_{0/1}$ as it was measured by ultrasonic probe 1 with the two possible Doppler Effect corrected mean wave periods $T_{0/1,+}$ and $T_{0/1,-}$ (top), the angle between the ship's heading and the wave direction α (middle) and the ship's velocity in knots (bottom).

It can be seen in equation (4.53), that two mathematical solutions are found for the frequency of the incoming waves f_s that can result to the frequency measured f_o. It shall therefore be examined whether both solutions are reasonable by physical means or if one can be neglected. Therefore the corresponding Doppler Effect corrected mean wave periods $T_{0/1,s+}$ and $T_{0/1,s-}$ are viewed upon and compared to the uncorrected mean wave period $T_{0/1,o}$ (see figure 4.22).
Figure 4.22, shows that the two solutions for the Doppler Effect corrected mean wave period $T_{0/1}$ result in two clearly distinguishable realms. While the negative solution dominates in the higher period realm and the positive solution dominates the lower realm, for some data points this relation switches, though the data points still fit into the observable trends. Therefore none of the two mathematical solutions can be clearly appointed to either of these realms.
As the lower period correction realm includes negative numbers on the right hand side of figure 4.22 and as further the visually estimated wave periods observed during the depicted period contradict the solutions of lower period duration, the realm with the higher period solution is assumed to be the one with the actual wave periods, while the lower solutions are neglected. As none of the two mathematical solutions can be appointed to either of this realms, both are computed and the solution corresponding to the higher period is used further.

It has to be noted that the value v_o in equation 4.53, even though it is the velocity of the observer, does not directly translate into the velocity of the ship. As v_o is the observer's velocity into the direction in which the waves are moving, it is gained from the ship's velocity scaled by the cosine of the direction of the incoming waves and the heading of the ship (see figure 4.21).

$$\alpha = wave\ direction\ -\ heading \tag{4.54}$$

$$v_o = v_{ship} \cdot cos(\alpha) \tag{4.55}$$

For the practical realisation of the Doppler Effect correction,the ship's velocity, heading and the wave direction are needed (see figure 4.22). As the wave direction has not been measured by any system of the ship and can not be gained from the measured water surface elevation signal η, it is taken from the ECWAM data, described in section 5.1.1.
The ship's velocity and heading are calculated from the ship's position from the One Ocean Data Exploration Portal of NORCE (2022). The ship's heading is gained from the vector between two positions of the ship. The ship's velocity is gained from the division of the vector norm by the time difference between the two positions.
Hereby it must be noted, that the position data used can not be regarded as clean. Longitudes and latitudes in the data show occasional jumps of 1 ° forth and back for some minutes, and furthermore the data is partially inconsistent and lacking for some periods. The jumps are filtered out in post processing, but the data lacks lead to falsification during the missing periods as the ship's velocity and heading are then an average over the closest available points. In most cases these position data lacks are of short duration and therefore not crucial, but one larger lack from 18.11.2021 to 22.11.2022 features values unusable for the Doppler Effect correction, as they result in a large amount of imaginary solutions in equation 4.53. This is caused by physically impossible combinations of the ships velocity, the angle between heading and wave direction and the frequencies measured. This lack can be seen in the constant values in figure 5.3
As the ship position and wave direction data are not available from 18.11.2021 to 22.11.2021, this time period is further excluded from the observation of values, that rely on the Doppler Effect correction.

From the Doppler Effect correction, the spectral analysis of the water surface elevation signal η, described in section 4.2.2, can be modified. The PSD shows the signal energy per frequency measured. As the measured frequencies are influenced by the Doppler Effect, the Doppler Effect correction, defined by equation (4.53), is applied to translate the observed frequency distribution of the PSD to the corresponding frequency distribution of the actual waves, by translation of the frequency array. An example for a Doppler Effect correction of a PSD is shown in figure 4.23.
From the Doppler Effect corrected PSD, the Doppler Effect corrected peak period T_p, as well as the Doppler Effect corrected spectral moments can be gained (section 4.2.2).

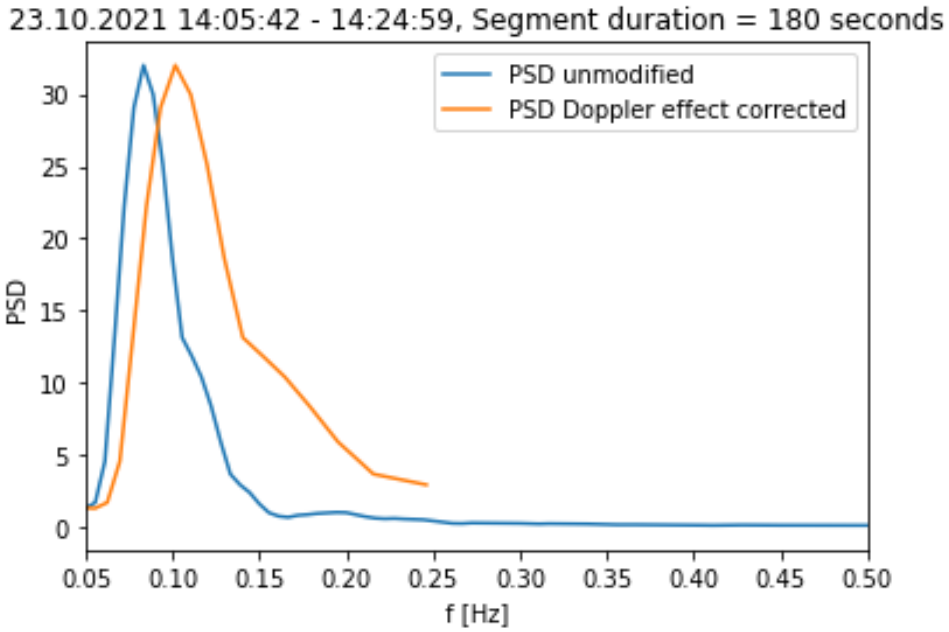

Figure 4.23: Comparison of the measured unmodified PSD from section 4.2.2 (blue) and the Doppler Effect corrected PSD (orange)

CHAPTER 5

Results

5.1 Comparison with Model and Satellite Data

The wave properties, gained from the wave sensor system, which shall be compared in this section, are based on the data measured by the ultrasonic probe 1 located at the bowsprit tip (see figure 2.1).

5.1.1 The Model Data

The model data used for comparison is taken from the high resolution WAM model included in the ECMWF's model, also referred to as ECWAM (ECMWF, 2016). The model output data is co-located with the ship's trajectory, from NORCE (2022). The used co-location constraints are $\pm 30\ min$ from hourly ship position's and a maximum of 50 km distance to the given trajectory (P. Bohlinger, personal communication, March 2022). The parameters used for comparison are the significant wave height $H_{s,model}$ and the peak period $T_{p,model}$. Furthermore, the simulated mean wave direction is used for a practical implementation of the Doppler Effect correction (section 4.3).

The significant wave height in the ECWAM model is gained from the modeled zeroth spectral moment, as in equation 4.47.

$$H_{s,model} = 4\sqrt{m_{0,model}} \tag{5.1}$$

The significant wave height given out by the model is often used in literature, to validate the model's accuracy in certain regions. Detailed evaluation of significant wave height accuracy of several WAM models can be found in Gusdal et al. (2011) for the northern Atlantic during the time period from 1999 to 2010. For the years from 2011 to 2013 another detailed analysis has been undertaken for the North Atlantic, including the specific ECWAM model by (Gusdal and Carrasco, 2012; Carrasco and Gusdal, 2014). For the European Atlantic Coast, the North American East Cost and the Gulf of Mexico, a study from 2002 can be found by Bidlot et al. (2002) which also includes the ECWAM model in particular. The most recent of these validations shows, that the RMSE of the significant wave height in the ECWAM changes seasonally from 0.2 m in the summer to 0.4 m in the winter for the domain of the northern Atlantic, and that the bias is around 0 m (Carrasco and Gusdal, 2014).

The peak period in the ECWAM model is defined as the reciprocal of the peak frequency in the wave spectrum (Bidlot, 2016) and thus analogue to equation 4.41.

$$T_{p,model} = \frac{1}{f(max(PSD_{model}))} \tag{5.2}$$

The peak period of the ECWAM is less frequently referred to in literature than the significant wave height. An evaluation of its accuracy is given by Bidlot et al. (2002) for the European Atlantic Coast, the North American East Cost and the Gulf of Mexico. It shows, that the peak period, given by the WAM model, is far less accurate than the significant wave height, with and average RMSE of 2.19 s (Bidlot et al., 2002).

An evaluation of the mean wave direction, in the ECWAM can be found in Ponce de León and Guedes Soares (2012) for the Norwegian coast. Though the report was published in 2012, the used data dates back to 1991/92.

5.1.2 The Satellite Data

The satellite based significant wave height $H_{s,satellite}$ is taken from 6 different satellites. The satellite data is co-located with the ship's trajectory from NORCE (2022) (see table 5.2). The used co-location

constraints are ± 30 *min* from hourly ship position's and a maximum of 50 *km* distance to the given trajectory (P. Bohlinger, personal communication, March 2022). As the data is gained from several different satellites, the data accuracy and the sensor footprint varies between the individual data sets (see table 5.1). All satellites use altimeters to determine the significant wave height. The data measured by these satellites is not used in the ECWAM model (P. Bohlinger, personal communication, March 2022). Therefore, the satellite data and model data (section 5.1.1) are completely independent.

Satellite Name	Accuracy	Resolution (along-track × across-track)	Documentation
Sentinel-3A&B	4 % NRT, 1 % STC	300 m × 1.64 km	(ESA, 2022b) (ESA, 2022c) (ESA, 2022d)
Jason-3	10 % or 0.5 m	11 km × 5 km	(NOAA, 2022)
Cryosat-2	5 %	250 m × 5 km	(ESA, 2022a) (Abdalla et al., 2018)
SARAL/AltiKa	0.15 m RSME	$2-7$ km diameter	(Kumar et al., 2015) (Li et al., 2021)
CFOSAT	8.2 %	25 km diameter	(Wang et al., 2021)

Table 5.1: Statistics of the different satellite retrievals of the significant wave height $H_{s,satellite}$.

Satellite Name	Date of Passing	Time Resolution
Sentinel-3A	12.10.2021 23:54:01 - 23:54:13	1 s
	07.11.2021 02:26:45 - 02:26:46	
Sentinel-3B	08.10.2021 23:20:04 - 23:20:12	1 s
	15.10.2021 12:33:07 - 12:33:14	
Jason-3	07.10.2021 17:48:49 - 17:49:04	1.018709 s
	02.11.2021 15:59:14 - 15:59:26	
	11.11.2021 03:26:57 - 03:27:13	
Cryosat-2	08.10.2021 15:09:21 - 15:09:28	0.943437 s
	18.10.2021 04:05:33 - 04:05:39	
SARAL/AltiKa	08.10.2021 19:39:42 - 19:39:54	1.033825 s
	24.11.2021 11:10:36 - 11:10:39	
CFOSAT	23.10.2021 10:59:15 - 10:59:22	1 s
	02.11.2021 11:42:40 - 11:42:51	
	08.11.2021 11:49:34 - 11:49:46	
	23.11.2021 12:52:47 - 12:52:55	

Table 5.2: Satellite passings over the trajectory of Statsraad Lehmkuhl from 05.11.2021 to 28.11.2021.

5.1.3 Significant Wave Height Comparison

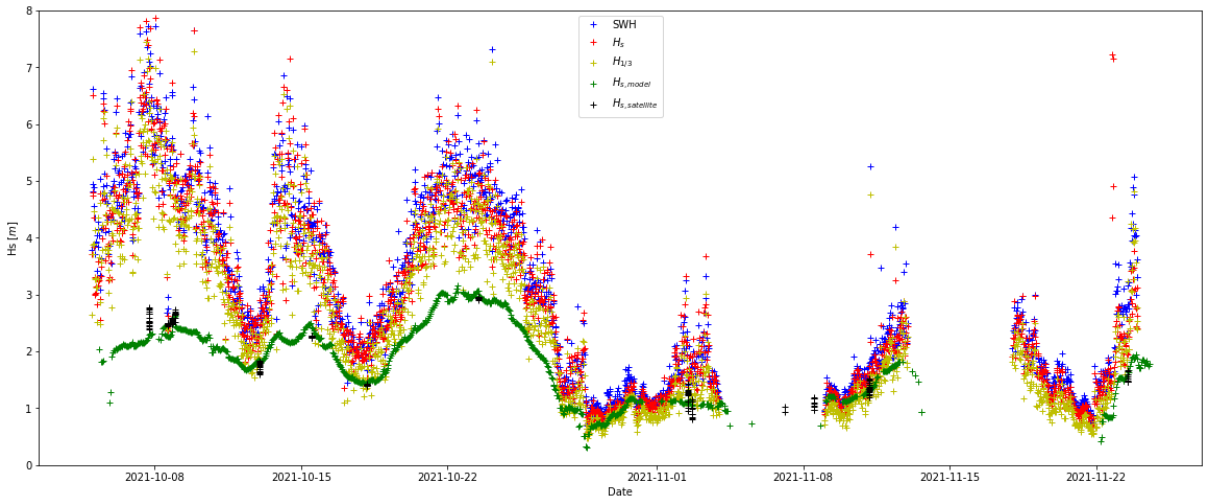

Figure 5.1: Comparison of the statistical significant wave height SWH given by equation 4.46 (blue), the statistical significant wave height H_s given by equation 4.47 (red), the significant wave height $H_{1/3}$ (yellow), $H_{s,model}$ from model data (green) and $H_{s,satellite}$ form satellite data (black) for the time period from 05.10.2021 to 24.11.2021.

Figure 5.1 shows the statistical significant wave heights measured by the system SWH (equation 4.46) and H_s (equation 4.47) compared to the significant wave height computed from the original definition $H_{1/3}$ (section 4.2.3) , the significant wave height simulated by the ECWAM model $H_{s,model}$ (section 5.1.1) and the significant wave height from the satellite measurements $H_{s,satellite}$ (section 5.1.2) for the period from 05.10.2021 to 24.11.2021. The data from 04.11.2021 to 08.11.2021 and from 13.11.2021 to 17.11.2021 is not shown, as the ship then was in harbour. The single data points of SWH, H_s and $H_{1/3}$ are obtained by a single 30 min data file each.
It can be seen in figure 5.1, that both statistical definitions for the significant wave height, SWH and H_s, give very similar results, while the significant wave height by the original definition $H_{1/3}$ gives slightly smaller values. The significant wave heights gained from satellite measurements $H_{s,satellite}$ are fitting the values predicted by the model $H_{s,model}$ well.
Over all, two periods with different characteristics can be seen in figure 5.1. The first period, from 05.10.2021 until approximately the 27.10.2021, shows a large discrepancy between the significant wave heights measured by the system (SWH, H_s and $H_{1/3}$) and the significant wave heights from model and satellite data. Hereby the significant wave heights computed from the systems measurements are generally higher than the model and satellite data. The significant wave heights measured by the system show a large deviation during this period. It is noticeable, that both the discrepancy and the deviation are larger for larger significant wave heights. The significant wave heights during the first period are overall larger than the ones of the second period. Comparison with figure 3.3 shows, that this first period corresponds to the crossing of the Atlantic until entering the Caribbean Sea.
The second period, from approximately 28.10.2021 to 24.11.2021 shows no large discrepancy. Furthermore, the deviation of the significant wave heights measured by the system (SWH, H_s and $H_{1/3}$) is far smaller, than in the first period and the significant wave heights are generally smaller. Comparison with figure 3.3 shows, that this second period corresponds to the sail through the Caribbean Sea.

5.1.4 Wave Period Comparison

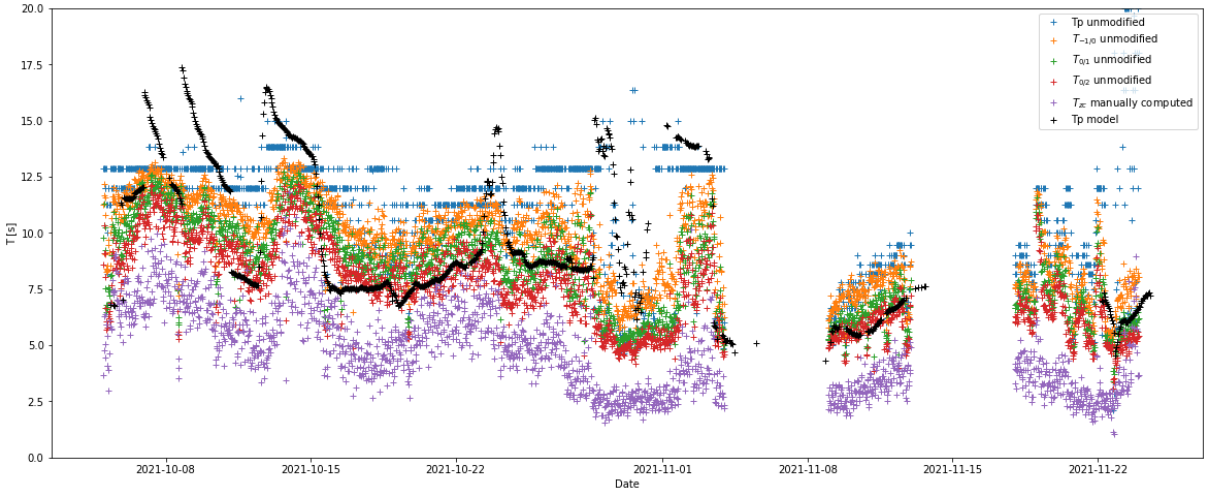

Figure 5.2: Comparison of the peak period T_p given by equation 4.41 (blue), the energy mean period $T_{-1/0}$ given by equation 4.43 (orange), the mean wave period $T_{0/1}$ given by equation 4.44 (green), the mean zero crossing period $T_{0/2}$ given by equation 4.45 (red), the manually acquired mean zero crossing period T_{zc} (purple) and the peak period from the model data $T_{p,model}$ for the time period from 05.10.2021 to 24.11.2021.

Figure 5.2 shows the values obtained by the different periods discussed in section 4.2.2 ,with no Doppler Effect correction applied, in comparison to the peak period gained from the model $T_{p,model}$ for the period from 05.10.2021 to 24.11.2021. The data from 04.11.2021 to 08.11.2021 and from 13.11.2021 to 17.11.2021 is not shown, as the ship then was in harbour. The single data points of the measured periods result from a single 30 *min* data file each.
All the periods gained from spectral moments and the manually computed mean zero crossing period follow the same temporal trend, only differing by their amplitudes. The peak period given by the model data $T_{p,model}$ partially follows the same trend, as the other periods, but occasionally jumps to very high values and descends again. In contrast, the peak period measured by the system T_p is constant over certain time spans and jumps between distinct values. A large discrepancy can be seen between the manually computed mean zero crossing period T_{zc} and the statistically defined mean zero crossing period $T_{0/2}$.

The measured periods in figure 5.2 result from PSDs, which are not corrected for the Doppler Effect (section 4.3). The peak period computed from Doppler Effect corrected PSDs $T_{p,corrected}$ is compared to the peak period from uncorrected PSDs $T_{p,unmodified}$ and the peak period given by model data $T_{p,model}$ in figure 5.3, to investigate the impact of the Doppler effect correction.

It can be seen in figure 5.3, that while the measured peak period $T_{p,unmodified}$ is constant over some time intervals, the Doppler Effect corrected peak period $T_{p,corrected}$ follows a trend which is similar to the peak period predicted by the model $T_{p,model}$. While the behaviour of the uncorrected peak period $T_{p,corrected}$ does not fit the expected behaviour of ocean waves, the Doppler Effect corrected peak period $T_{p,corrected}$ looks realistic. Under the assumption, that the Doppler Effect corrected peak period $T_{p,corrected}$ fits to the peak period of the actual waves, the behaviour of the uncorrected peak period $T_{p,unmodified}$ cannot origin from a measurement error, but must be a result of the Doppler Effect. It could be considered if the temporal constant unmodified peak periods by the ship's perspective are caused by the physical relation between the waves and the ship's velocity.
Over all figure 5.3 shows, that the Doppler Effect seems to have a large influence on the measured wave spectrum and the spectral analysis. Uncorrected peak periods seem to be untrustworthy and are thus not used further.

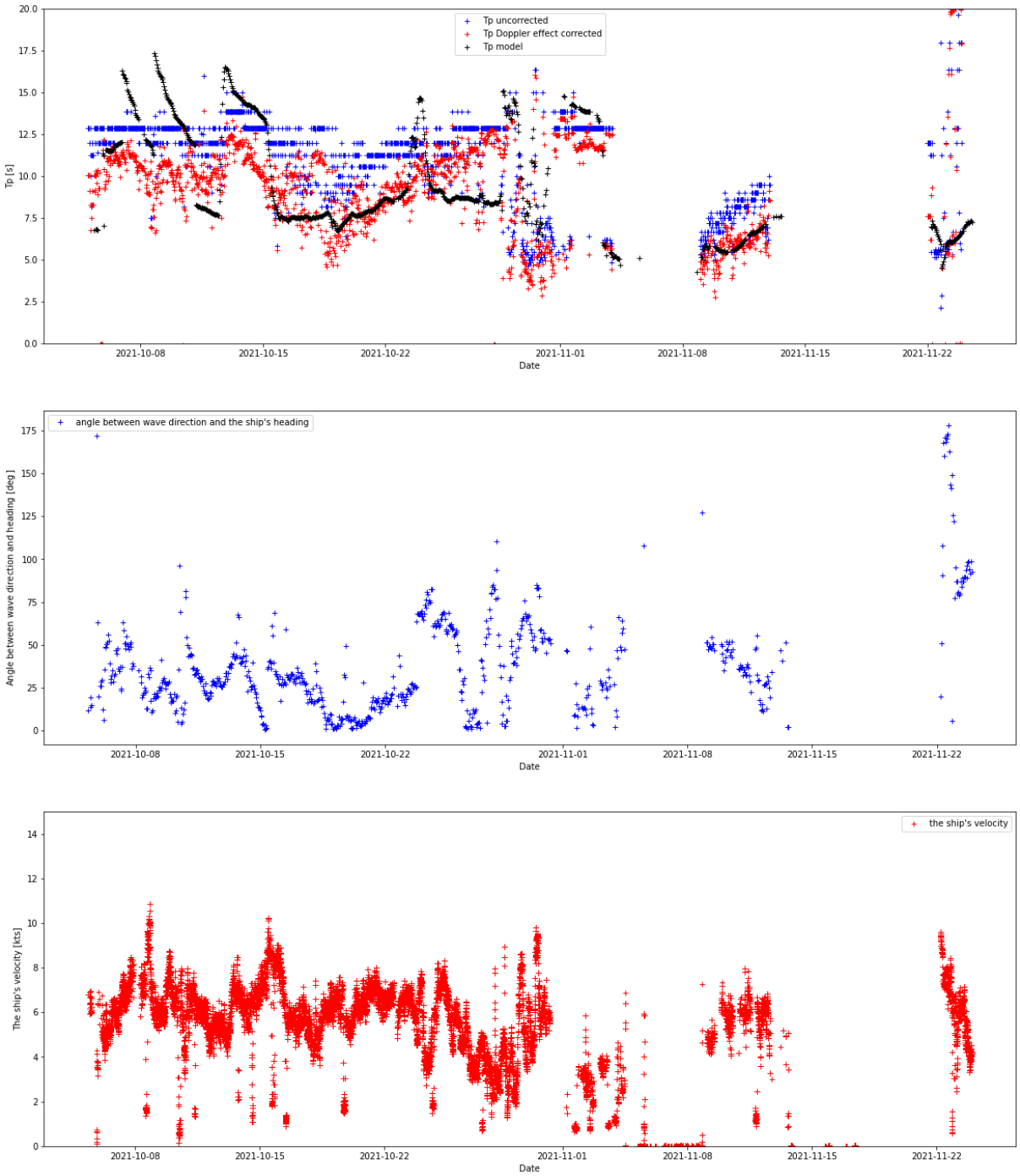

Figure 5.3: Comparison of the measured unmodified peak period $T_{p,unmodified}$ (blue), the Doppler Effect corrected peak period $T_{p,corrected}$ (red) and the peak period given by model data $T_{p,model}$ (black) (top), the angle between heading and wave direction α (middle) and the ship's velocity in knots (bottom).

5.2 Comparison of the Data from the Different Altimeter Probes

The data measured with the different probes is compared for the significant wave height SWH and the Doppler Effect corrected peak period $T_{p,corrected}$. The differences between the probes are the different location of the two identical ultrasonic probes and the different measurement technology of the radar probe compared to the ultrasonic probe in the same location. For all probes the motion correction of the measured distances uses the VN100 measurements, as described in section 4.2.1. The single data points of the values computed from the systems measurements, result from a single 30 min data file each.

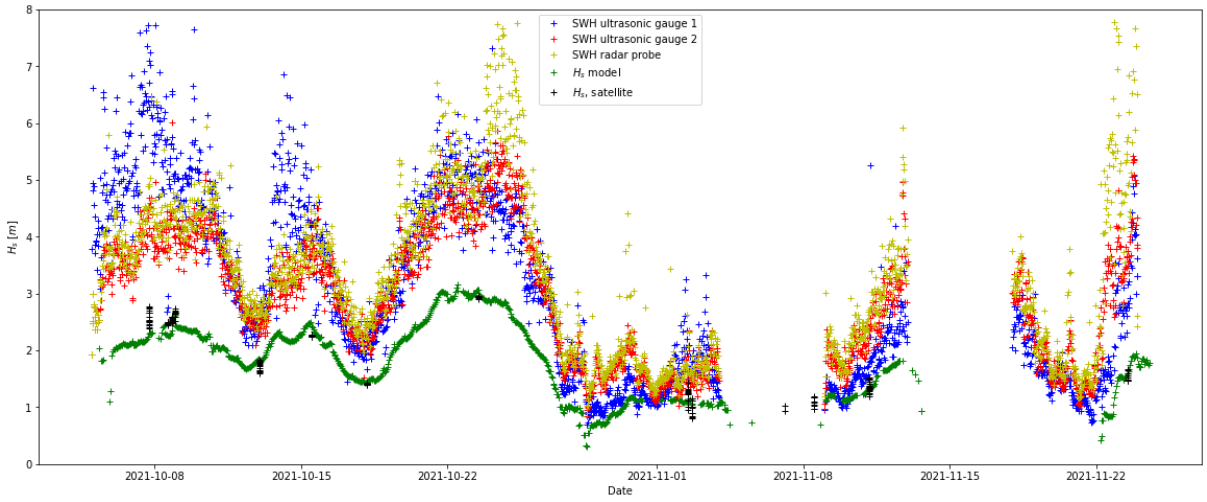

Figure 5.4: Comparison the the significant wave heights SWH gained from the different probes, the significant wave height from model data $H_{s,model}$ (section 5.1.1) and the significant wave height from satellite data $H_{s,satellite}$ (section 5.1.2).

Figure 5.4 shows, that the radar probe produces a slightly higher significant wave height than the ultrasonic probe 2 in the same location. Furthermore, the significant wave heights gained from the ultrasonic gauge 2 and the radar probe on the starboard side of the bow are smaller than the significant wave heights gained from the ultrasonic gauge 1 at the bowsprit in high waves in the left side of figure 5.4,but they are comparably higher in the lower waves on the right side. Also, the scatter of the significant wave heights in higher waves is lower for the ultrasonic probe 2, than for the radar probe and ultrasonic gauge 1.

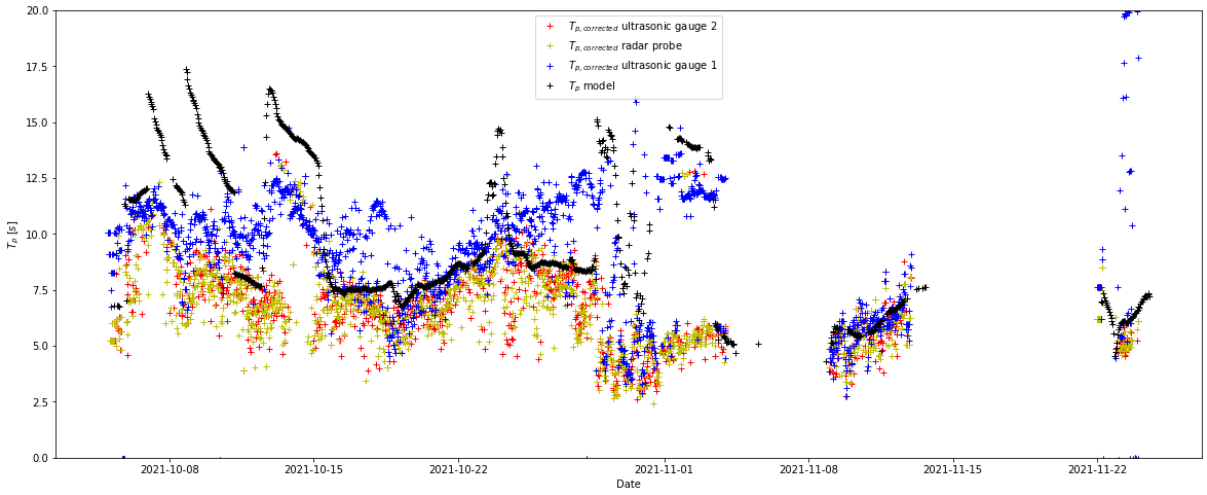

Figure 5.5: Comparison between the Doppler Effect corrected peak periods T_p gained from the different probes and the peak periods given by model data $T_{p,model}$.

In figure 5.5 peak periods gained from the different probes are compared to the peak period from model data $T_{p,model}$ after correction for the Doppler Effect was applied (section 4.3), because of the findings in section 5.1.4.
Figure 5.5 shows a good fit between the peak periods gained from the ultrasonic probe 2 and the radar probe. However, large discrepancies can be observed between the peak periods gained from the sensors at the starboard side of the bow and the ultrasonic probe 1 at the bowsprit tip.
The ultrasonic probe 2 and the radar probe are measuring the distance to the water surface directly downwards, but they are located rather close to the ship's hull. If waves interact with the hull, before they reach the sensors at the bow, their frequency might have been changed. Also reflected waves might cause a too high frequency in the measured data. Due to its position, the waves passing under the ultrasonic gauge 1 at the bowsprit are far less endangered in regard to falsification by the ship's hull.
To examine, whether the difference in the peak periods measured by the bow probes and the bowsprit probe is caused by the influence of the ship's hull, the difference between the peak period gained from ultrasonic gauge 1 and the one gained from ultrasonic probe 2 is observed in relation to the angle of the incoming waves, with midships as 0°, portside as negative angles and starboard as positive angles.

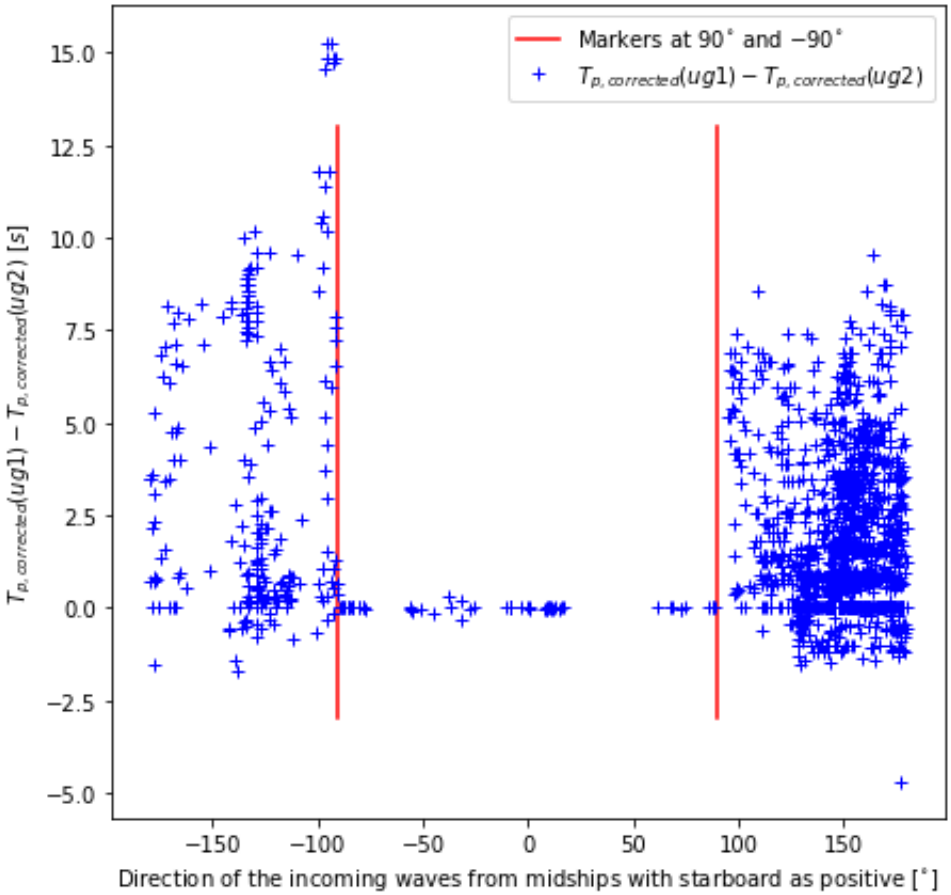

Figure 5.6: Scatter-plot of the difference in peak period between the two ultrasonic probes over the angle of the incoming waves in relation to midships.

Figure 5.6 shows, that the difference in the peak periods determined by the ultrasonic sensors depends on the angle of the incoming waves in relation to midships. While waves coming from ahead result in the same peak period for both sensors, waves coming from astern result in different peak periods. The hypothesis that this is caused by the positioning of the ultrasonic probe 2 close to the ship's hull, is supported by the observation of a small asymmetry regarding starboard and portside in figure 5.6. While for waves coming from portside, differences in the peak period can already by observed at values up from 90°, for waves coming from the starboard side a difference in the peak periods does not occur at 90°, but only further astern. This effect might originate from the positioning of the ultrasonic probe 2 on the starboard side of the bow, allowing waves from starboard to pass under the sensor unfalsified at a higher

angle towards astern, than for waves from portside.
As an influence by the ship's hull can be excluded for the ultrasonic sensor 1 at the bowsprit, only peak periods gained by this probe can be regarded as trustworthy.

5.3 Investigation of the Discrepancy between the Measured Significant Wave Height and the Model Data

5.3.1 Investigation of possible error causes

The comparison between the measured significant wave height SWH and the model and satellite data in section 5.1.3 showed, that the system tends to overestimate the significant wave height in higher waves (figure 5.1). It shall be inspected which circumstances the error depends on, to find a possible cause for it. The data used for this investigation was measured by the ultrasonic probe 1 (see figure 2.1) from 05.10.2021 to 24.11.2021, excluding harbour days. Wave properties are computed for a single 30 min data file each.

It has been observed in section 5.1.4, that the Doppler Effect has a significant impact on the measured peak period T_p. As it can be seen in figure 5.3 and further be derived from the equations 4.48 and 4.55, the influence of the Doppler Effect strongly depends on the angle between the ship's heading and the wave direction. To observe whether the direction of the waves, relative to the ship's heading ,influences the discrepancy between the measured significant wave height and the significant wave height from the model data, a correlation factor ρ between these two parameters is determined by usage of a Spearman Correlation.

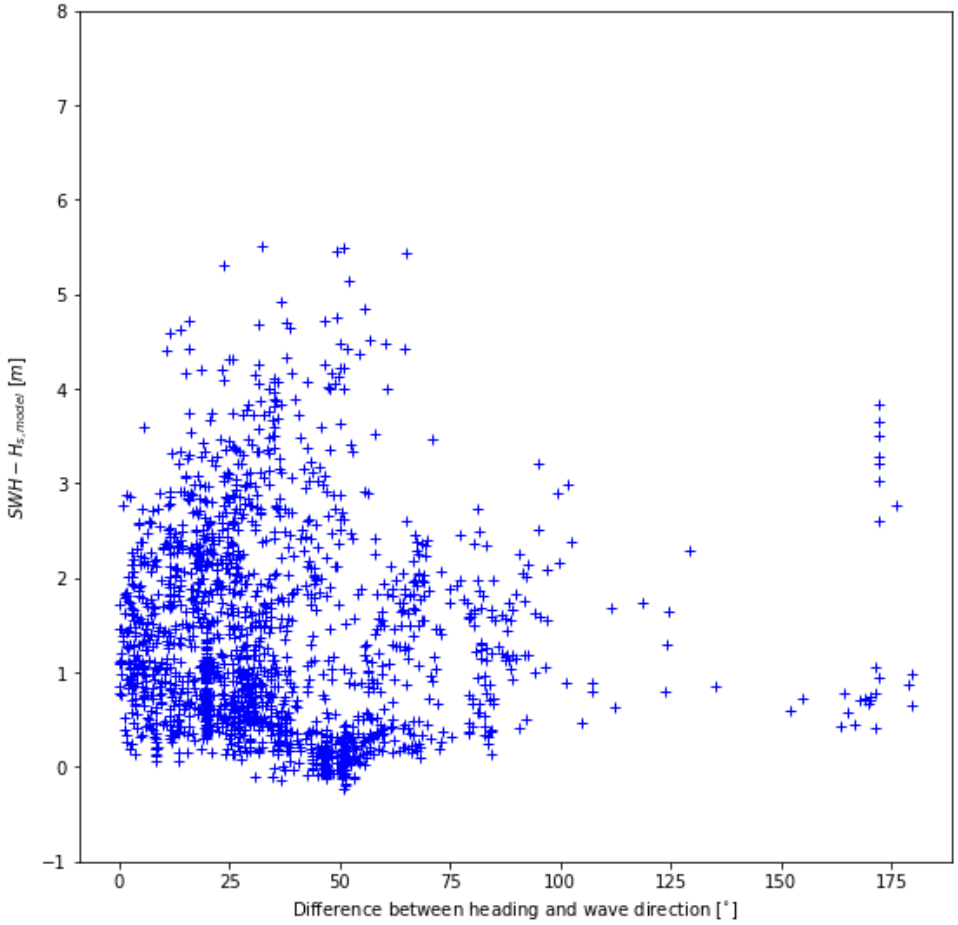

Figure 5.7: Scatterplot of the discrepancy between SWH and $H_{s,model}$ to the angle between the ship's heading and the wave direction.

From figure 5.7 and the computed correlation coefficient $\rho = 0.16$ can be concluded, that the discrepancy between the measured SWH and $H_{s,model}$ is not related to the wave direction relative to the ship's heading.

As the footprint of the ultrasonic probes can extend to a maximum diameter of 4.89 m at the maximal measurable distance of 15.2 m (section 2.2.1), it shall be determined, whether the size of the footprint might cause errors, if the wave length is too short. Therefore the discrepancy between the measured SWH and $H_{s,model}$ is correlated with the peak period T_p. with a Spearman correlation. The peak period T_p is hereby given by the Doppler Effect corrected peak period $T_{p,corrected}$ (section 4.3, 5.1.4).

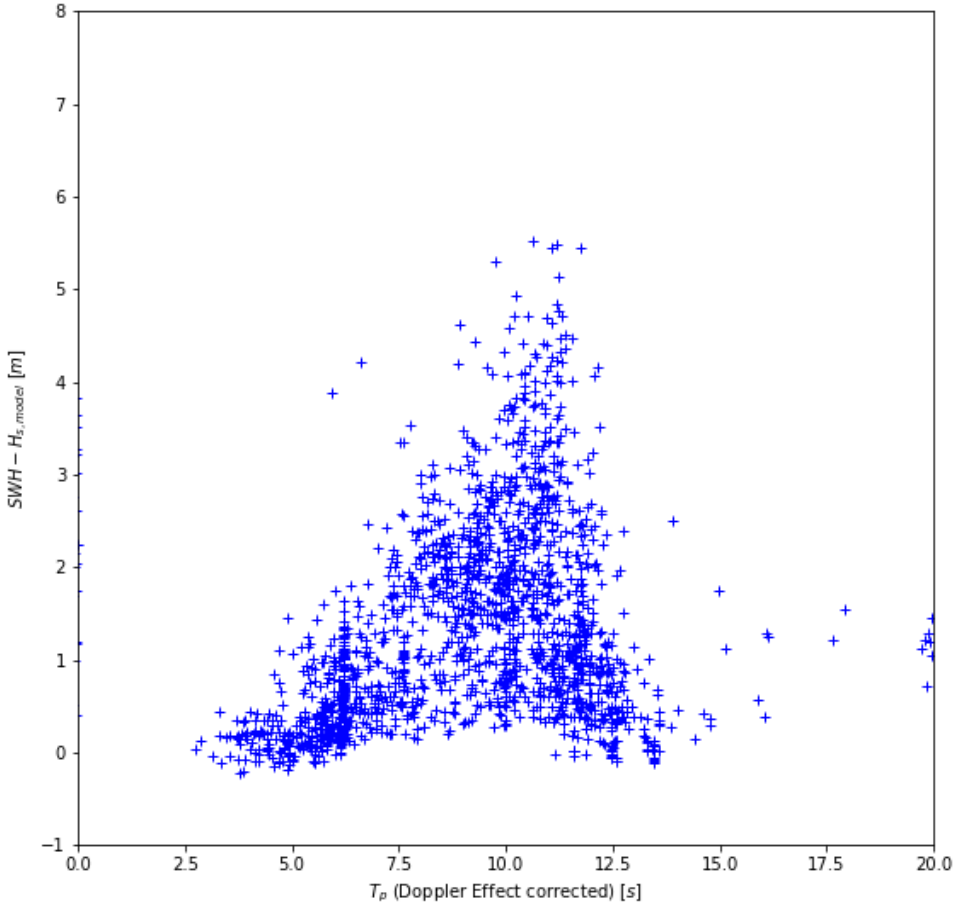

Figure 5.8: Scatterplot of the discrepancy between SWH and $H_{s,model}$ to the Doppler Effect corrected peak period $T_{p,corrected}$.

As figure 5.8 shows smaller discrepancies for short period waves, and as the computed correlation coefficient of $\rho = 0.25$ is small, it is concluded, that the ultrasonic sensor's footprint is not causing an error for shorter waves.
It can however be seen in figure 5.8, that higher discrepancies can only appear at higher peak periods, but higher peak period must not automatically result in a higher discrepancy. This phenomenon might be explained by the the peak period T_p influencing the ship's and the sensor's motion. Shorter periods have little influence on the ship's motion at any wave height and therefore result in a small discrepancy. Longer wave periods might result in a strong or weak motion of the ship, depending on the wave height, and thus also in a high or low discrepancy.
To test this hypothesis the discrepancy between the measured significant wave height SWH and $H_{s,model}$ is correlated with the significant amplitude of the vertical oscillation of the ultrasonic probe 1 $Z_s(ug1)$, given by equation (4.24).

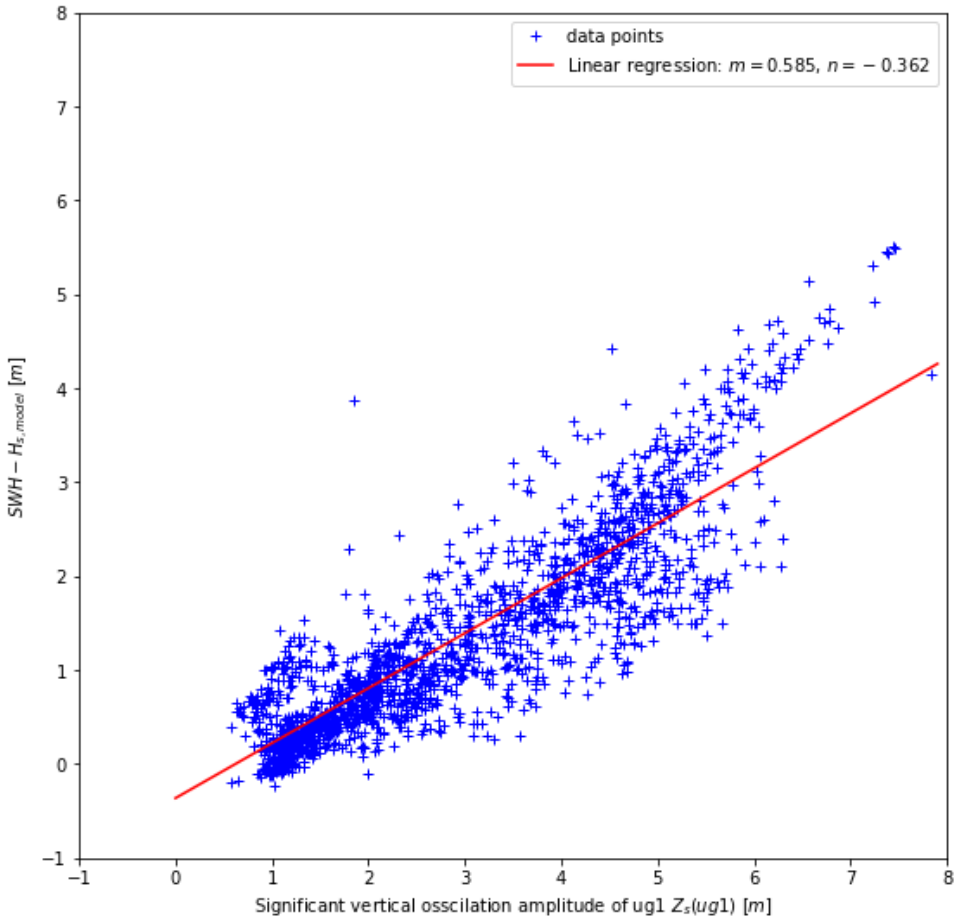

Figure 5.9: Scatterplot of the discrepancy between SWH and $H_{s,model}$ to the significant amplitude of the vertical oscillation of the ultrasonic probe 1 $Z_s(ug1)$, defined by equation (4.24).

Figure 5.9 and the computed correlation coefficient $\rho = 0.87$ suggest a dependency of the discrepancy between measured and modeled significant wave height on the significant amplitude of the sensor's oscillation and thus on the intensity of the ship's motion. The linear regression seen in figure 5.9 is based on the fit of a linear function on the depicted data points. The coefficients incline m and displacement n are found by a quadratic error sum approach. Therefore, the large number of data points on the left side of the scatter plot has the larger impact on the linear regression. Alternatively a steeper linear regression could be suggested, to fit better to the right hand side points of the scatter plot.

The main conclusion from the investigation of possible error sources is, that the discrepancy between the measured significant wave height SWH and $H_{s,model}$ is most likely caused by the influence of the ship's motion on the measured data. Even though the ship's motion is theoretically compensated for in section 4.2.1, it seems as if practically the influence is not eradicated entirely.

The position time series of the probes is gained form the data measured by the VN100 plus the approximations determined in section 4.1.5. As the motion correction seems to be the major error source for the significant wave height, it must be considered which effect the distance between the VN100 and the probes has on the result after all. Therefore the significant wave height SWH, computed with the sensor position gained from the VN100 and the approximation, is compared to the significant wave height SWH, computed with the sensor position gained from the extra IMUs. Since the extra IMU 1 had initial failures (section 3) a major data lack exists for the position data the ultrasonic probe 1. Therefore, the data of ultrasonic probe 2 and extra IMU 0 is also viewed upon, even though they are located way closer to the VN100.

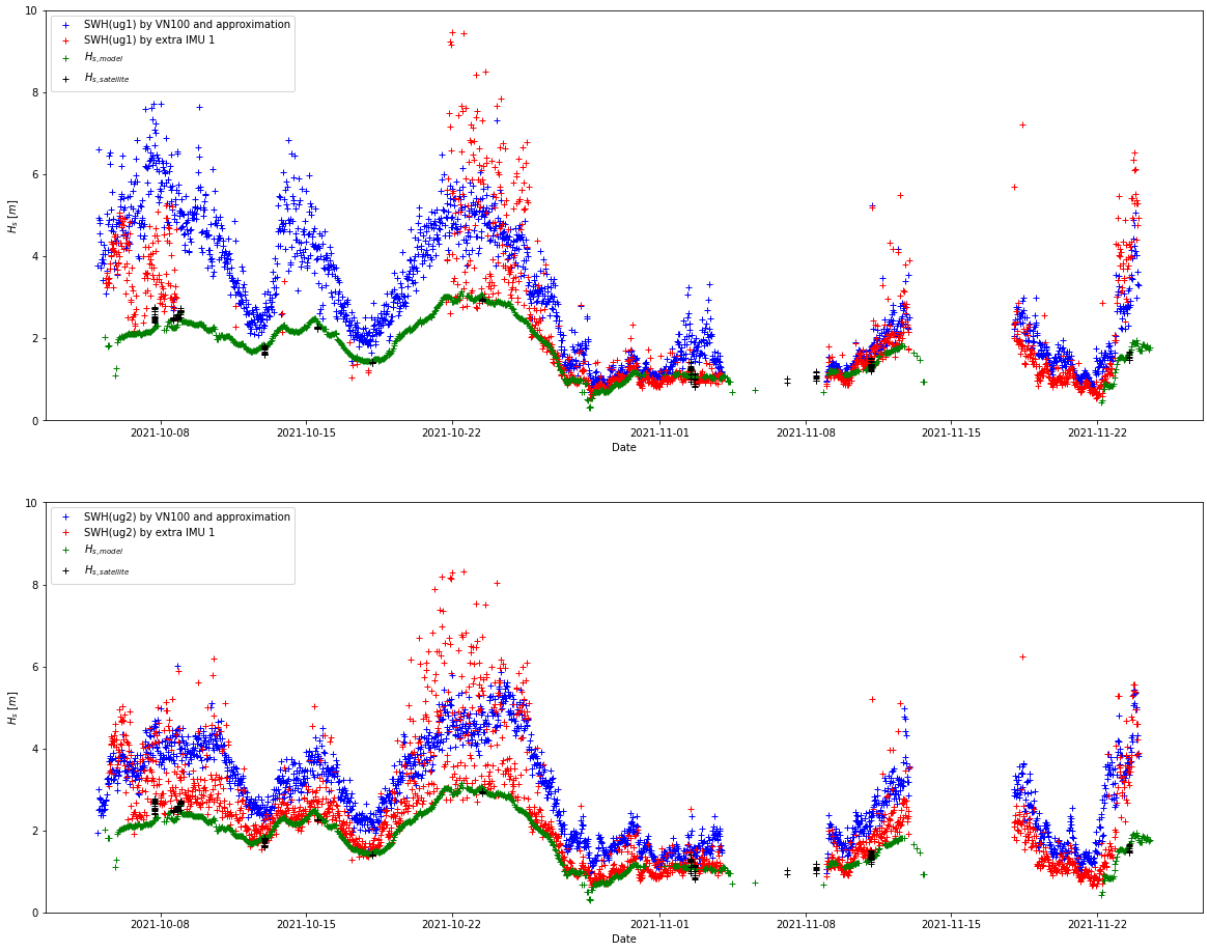

Figure 5.10: Comparison of the significant wave height computed by the sensors position data gained from the VN100 and the position approximation (section 4.1.5), to the significant wave height computed with the sensor position data from extra IMU 1 for ug1 (top) and extra IMU 0 for ug2 (bottom).

Figure 5.10 shows, that the significant wave heights computed by the extra IMUs directly at the probes, seem to fit the trend of the model and satellite significant wave heights $H_{s,model}$ and $H_{s,satellite}$ better, especially for ultrasonic gauge 2 and extra IMU 0. However, figure 5.10 also shows, that especially for higher waves, when the discrepancy between the significant wave height based on the VN100 and the model data is largest, the significant wave heights based on the extra IMUs are subject to a wide scatter, which, in some cases, is twice as large as the discrepancy itself.

5.3.2 Attempts to Compensate for the Discrepancy

As the discrepancy between the measured significant wave height SWH and the significant wave heights gained from model data $H_{s,model}$ and satellite data $H_{s,satellite}$ seems to be a systematic error of the measured data (section 5.3.1), an attempt shall be made to compensate for this error by finding a post processing method, that minimises it.

Re-scaling by Introduction of a Scaling Coefficient

Both significant wave heights SWH and H_s measured by the system are significantly higher in larger waves than the significant wave heights given by model and satellite data $H_{s,model}$ and $H_{s,sat}$. The impact of several scaling coefficients on both wave heights SWH and H_s shall be evaluated. Scaling coefficients S are hereby multiplied with either the variance of the water surface elevation signal η for SWH or the PSD for H_s

$$SWH_{scaled} = 4\sqrt{S \cdot var(\eta)} = \sqrt{S} \cdot 4\sigma(\eta) \tag{5.3}$$

$$H_{s,scaled} = 4\sqrt{m_{0,scaled}} \tag{5.4}$$

$$m_{0,scaled} = \int_{f_{min}}^{f_{max}} S \cdot PSD(f) df \tag{5.5}$$

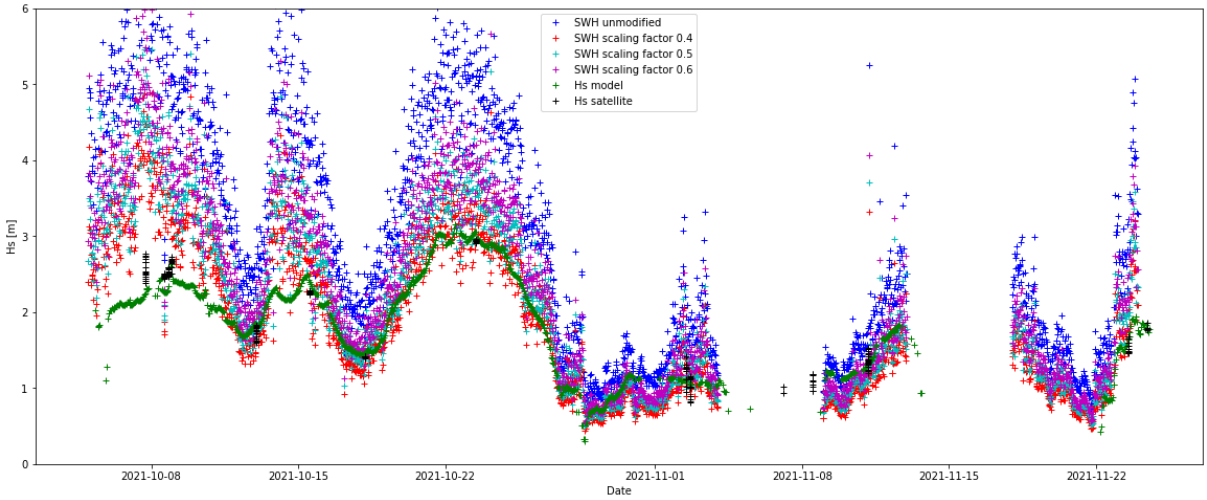

Figure 5.11: Comparison of significant wave heights SWH with different scaling coefficients S applied by equation 5.3, to the significant wave heights given by model and satellite data $H_{s,model}$ and $H_{s,satellite}$.

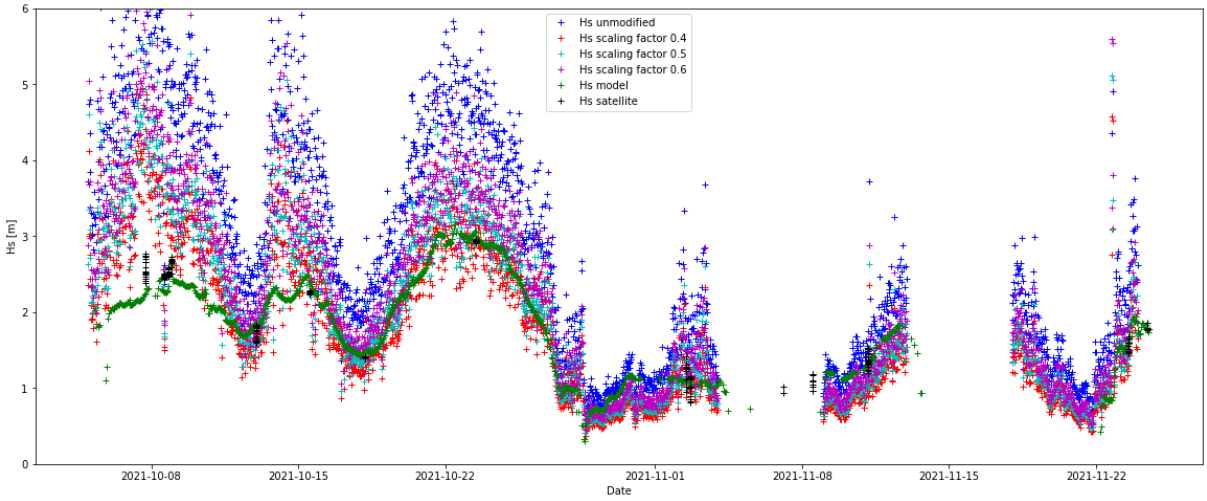

Figure 5.12: Comparison of significant wave heights H_s with different scaling coefficients S applied by equation 5.4 and 5.5, to the significant wave heights given by model and satellite data $H_{s,model}$ and $H_{s,satellite}$.

It can be seen in figure 5.11 and 5.12, that for both significant wave height definitions SWH and H_s scaling coefficients of $S = 0.4$ can be chosen, to minimise the discrepancy to $H_{s,model}$ and $H_{s,satellite}$ in the high wave areas. However, this scaling coefficient of $S = 0.4$ results in the largest negative bias for lower waves. The scaling coefficient of $S = 0.4$ corresponds to a multiplication of the unscaled significant wave heights with $\sqrt{0.4} \approx 0.63$.

For a better visualisation, the significant wave heights SWH_{scaled} and $H_{s,scaled}$, scaled with a coefficient of $S = 0.4$, are compared to the unscaled significant wave heights SWH and H_s and the significant wave heights given by model and satellite data $H_{s,model}$ and $H_{s,satellite}$ in figure 5.13 and 5.14, without the other scalings being depicted.

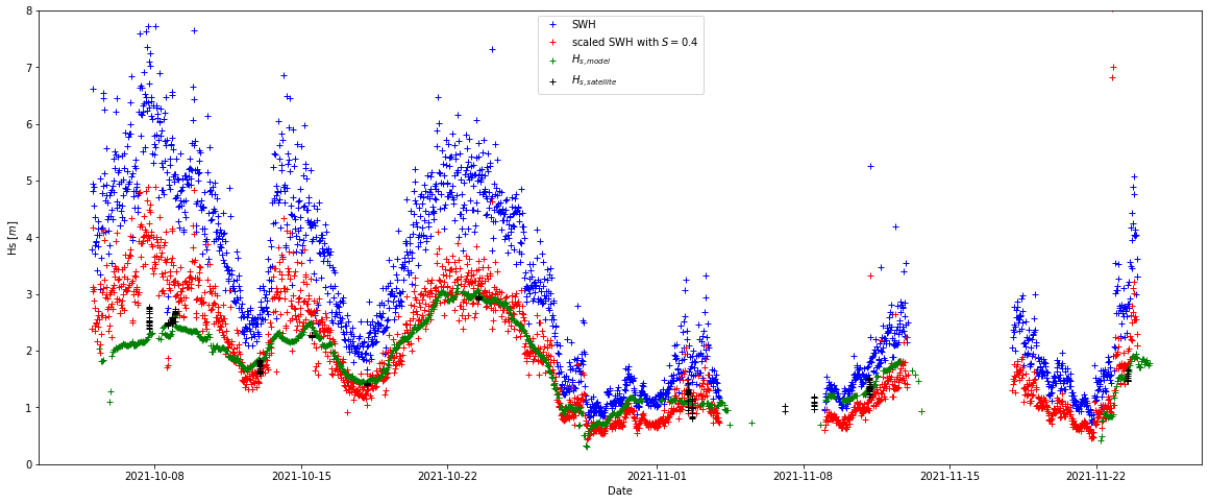

Figure 5.13: Comparison of the significant wave height SWH_{scaled} scaled with $S = 0.4$ by equation 5.3, to the unscaled significant wave height SWH and to the significant wave heights given by model and satellite data $H_{s,model}$ and $H_{s,satellite}$.

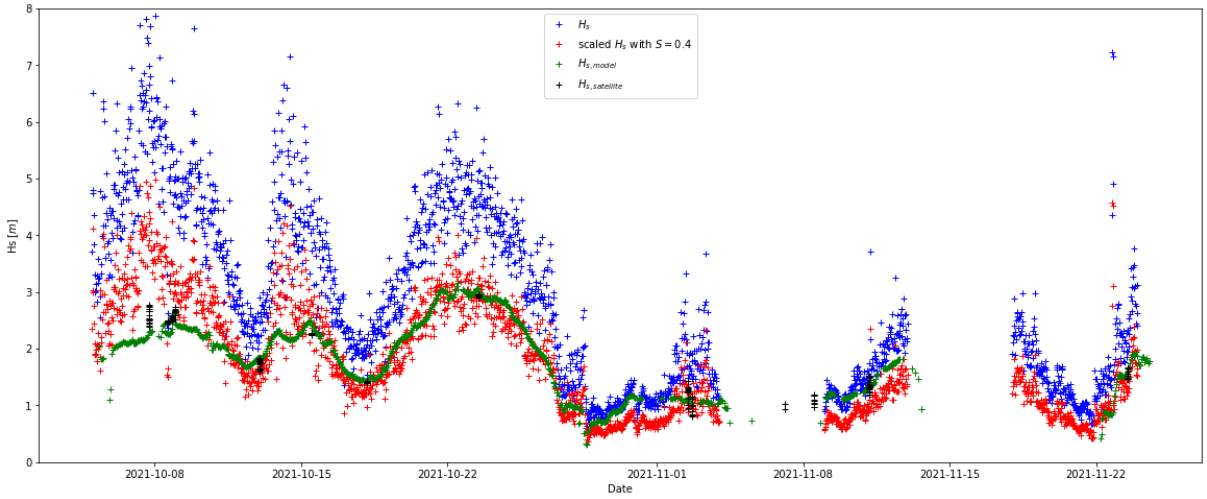

Figure 5.14: Comparison of the significant wave height $H_{s,scaled}$ scaled with $S = 0.4$ by equation 5.4 and 5.5, to the unscaled significant wave height H_s and to the significant wave heights given by model and satellite data $H_{s,model}$ and $H_{s,satellite}$.

It can be seen in figure 5.13 and 5.14, that the scaling does not perfectly fit the significant wave heights, measured by the system, to the simulated values $H_{s,model}$. However the scaling does eradicate most of the discrepancy between the measured significant wave heights and the satellite data $H_{s,satellite}$. An exemption of this are the earliest satellite measurements shown in figure 5.13 and 5.14.
Figure 5.4 shows, that for this area the ultrasonic probe 2 measured far lower significant wave heights SWH, than the ultrasonic probe 1. Therefore the effect of applying the scaling coefficient $S = 0.4$ on the significant wave height SWH measured by ultrasonic probe 2 is evaluated in figure 5.15.

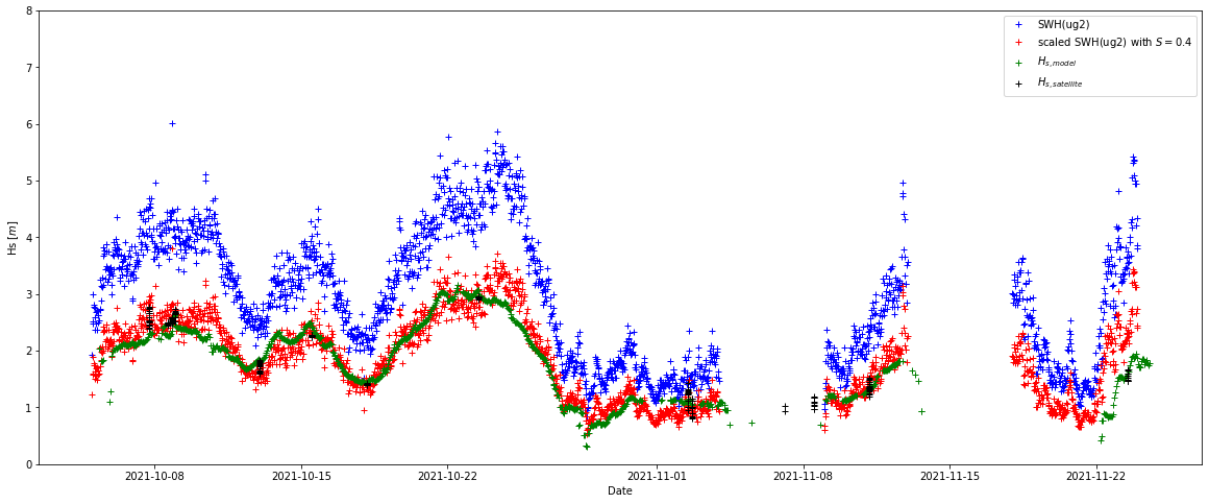

Figure 5.15: Comparison of the significant wave height $SWH_{scaled}(ug2)$ scaled with $S = 0.4$ by equation 5.3, to the unscaled significant wave height $SWH(ug2)$ and to the significant wave heights given by model and satellite data $H_{s,model}$ and $H_{s,satellite}$.

Figure 5.15 shows, that discrepancy between the scaled significant wave height, gained from the ultrasonic probe 2, $SWH_{scaled}(ug2)$ and the significant wave heights given by model and satellite data $H_{s,model}$ and $H_{s,satellite}$ is smaller than for the scaled significant wave height, gained from ultrasonic probe 1, $SWH_{scaled}(ug1)$. The significant wave height gained from the ultrasonic probe 2 and scaled with a coefficient 0.4 gives thereby the best fit to the significant wave heights given by model and satellite data.

Band-pass Filtration of the Water Surface Elevation Signal

Single 30 min data files, are inspected for dates with a large discrepancy between the significant wave height measured by the system SWH and and the significant wave heights given by model and satellite data $H_{s,model}$ and $H_{s.satellite}$. It is found, that in the selected files, unrealistic downward spikes occur occasionally in the water surface elevation signal η (see figure 5.16). These downward spikes do not resemble the physical behaviour of wave troughs and must therefore be measurement errors.

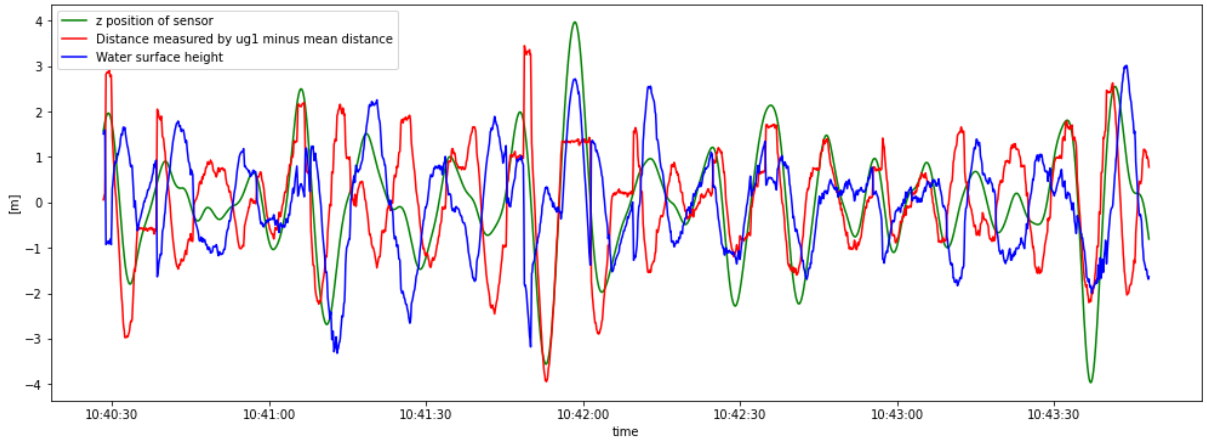

Figure 5.16: Water surface elevation signal η for the 23.10.2021 at around 10:40.

This date and time shown in figure 5.16 are chosen in particular as here a large discrepancy between the significant wave heights can be found and furthermore satellite data is available for 10:59. The significant wave height measured by the satellite is $H_{s,satellite} = 2.9\ m$ while the significant wave height received from the measured data of ultrasonic gauge 1 is $SWH = 4.99\ m$. In figure 5.16 a period with the mentioned downwards spikes can be seen, as well as a period with smoother oscillation.
It is investigated, whether the discrepancy between the significant wave heights from the probe and the

satellite measurements can be reduced, by filtering the water surface elevation signal η. Therefore, a Butter bandpass algorithm of fifth order is applied on the water surface elevation signal η. The lowcut threshold is set to 0.05 Hz and the highcut threshold is set to 0.5 Hz.

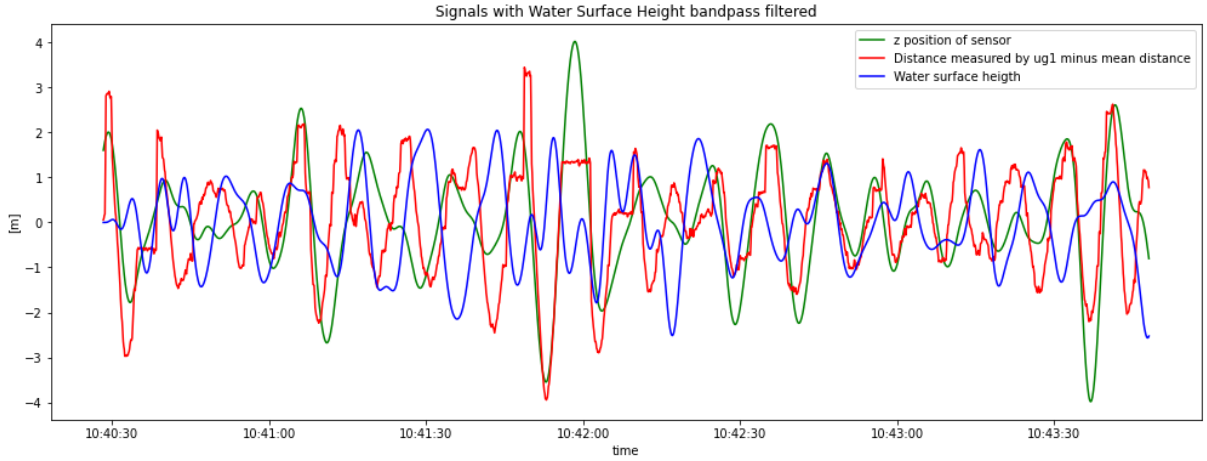

Figure 5.17: Water surface elevation signal filtered with a Butter bandpass η_{Butter} for the 23.10.2021 at around 10:40.

Figure 5.17 shows a clear improvement regarding the downward spikes seen in figure 5.16. The significant wave height gained from the filtered signal is computed to $SWH_{Butter} = 4.7\ m$, which is smaller than the significant wave height of the unfiltered signal $SWH = 4.99\ m$, but still far larger than the significant wave height gained from the satellite data $SWH_{satellite} = 2.9\ m$.
To determine, whether the small impact of the signal filtration on the significant wave height SWH_{Butter} is coincidental, the filtered water surface elevation signal η_{Butter} is produced for all the data files from 05.10.2021 to 24.10.2021 and compared with the significant wave height of the unfiltered signal SWH.

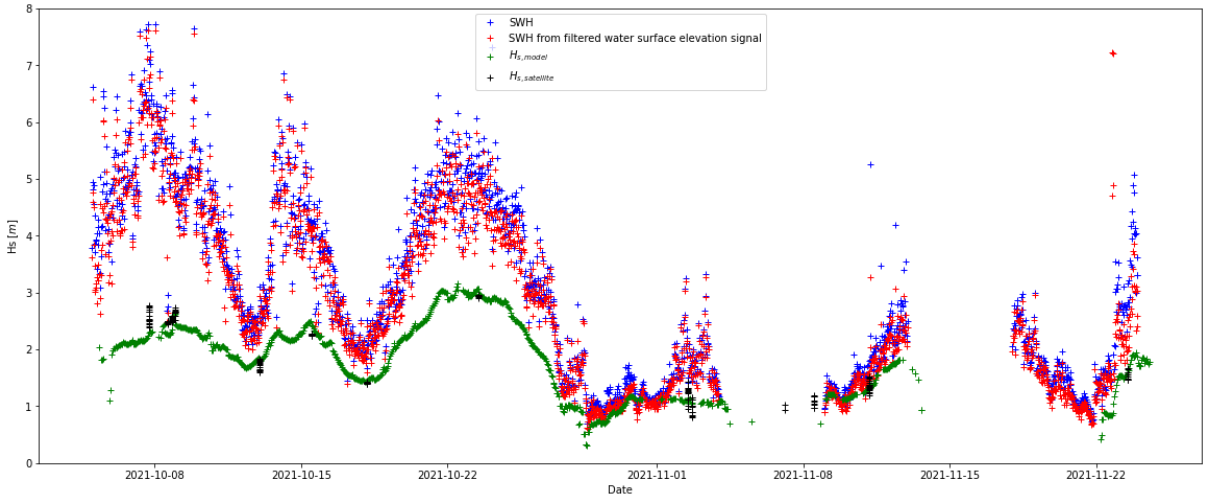

Figure 5.18: Comparison of the significant wave height gained from the bandpass filtered water surface elevation signal SWH_{Butter} (red), to the significant wave height of the unfiltered signal SWH (blue), the significant wave height of the model data $H_{s,model}$ (green) and the significant wave height from satellite measurements $H_{s,satellite}$ (black).

Figure 5.18 shows that, the Butter bandpass filtering of the water surface elevation signal has little effect on the computed significant wave height and by no means eradicates the discrepancy between the significant wave height obtained from the system's measured data and the significant wave height given by the model and satellite data.

Significant Wave Height from the Positive Water Surface Elevation

As inspection of the water surface elevation signal η showed curious downward spikes in figure 5.16, it shall be tested whether the discrepancy between the significant wave height gained from the probes and the significant wave height from model and satellite data is mainly based on the negative domain of the water surface elevation η.
The water surface elevation η should be oscillating symmetrically around 0, as the calm water surface is defined at zero by equation 4.40. By this symmetry, the relation $\eta_+ = -\eta_-$ is found. Therefore it should not matter whether the entire signal is used to determine the significant wave height SWH, or if only the positive side of the signal is used, as the water surface elevation is squared in equation 4.46.

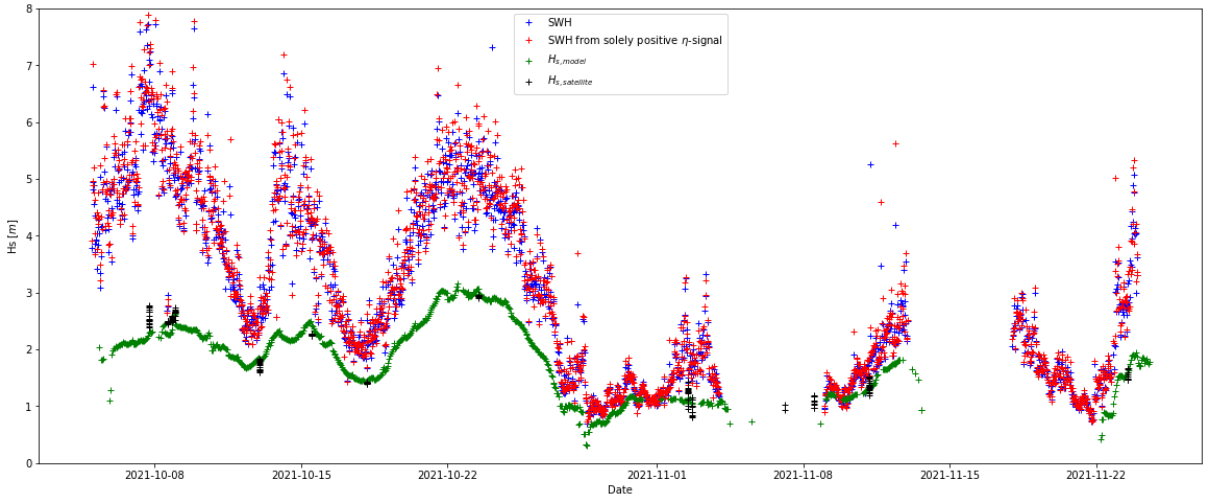

Figure 5.19: Significant wave height SWH of the entire water surface elevation signal η compared to the significant wave height computed from only the positive part of the signal η_+ and to model and satellite date $H_{s,model}$ and $H_{s,satellite}$

Figure 5.19 shows, that it does in fact make no significant difference whether the entire water surface elevation signal or just its positive region is used to determine the significant wave height SWH. The idea, that the discrepancy between the significant wave height gained from the system and the significant wave heights from model and satellite data might originate from a falsified negative side of the water surface elevation signal η is thus proven wrong.

5.4 Inspecting the Data for Different Swell Types

It shall be inspected, whether the spectral analysis of the measured water surface elevation signal η, allows to draw conclusions about the type of swell that resulted in the measured water surface elevation signal η. Therefore the PSDs of multiple successive data files are compared and set in context with the significant wave heights and Doppler Effect corrected peak periods. The specific dates and times are selected by the notes of visual wave observations (section 3) and by manual search through the data and serve as representative examples for different wave types. The data used was measured by ultrasonic probe 1 at the bowsprit (see figure 2.1).

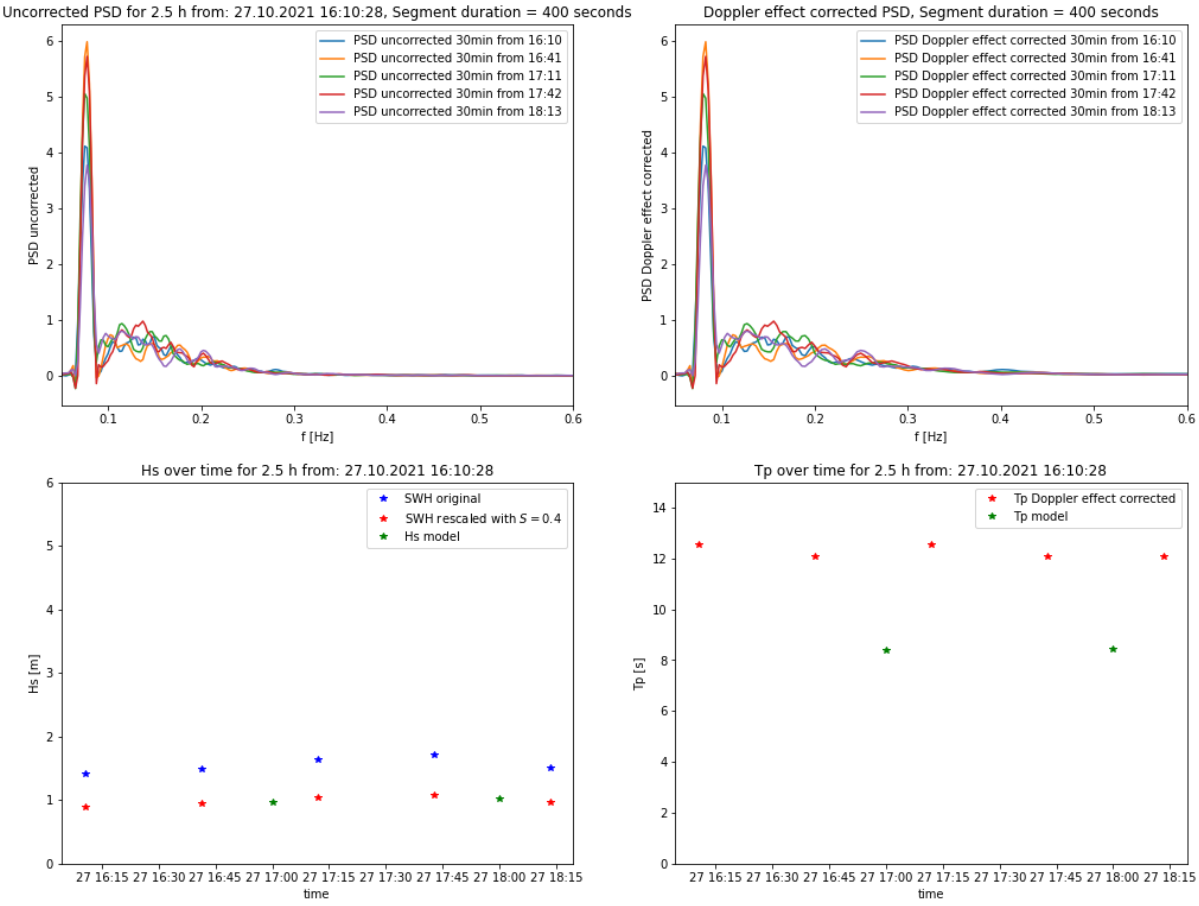

Figure 5.20: Wave properties over 2.5 hours from 27.10.2021 16:10 computed from single 30 *min* data files: *Top left:* Uncorrected PSDs *Top right:* Doppler Effect corrected PSDs *Bottom left:* measured significant wave height SWH, the rescaling SWH_{scaled}, $S = 0.4$ (section 5.3.2) and the model data significant wave height $H_{s,model}$ *Bottom right*: Doppler Effect corrected peak Period $T_{p,corrected}$ and peak period from model data $T_{p,model}$.

The spectrum shown in figure 5.20 has a distinct peak on a lower frequency. This is typical for long travelling swells (Ochi, 1998). The chaotic energy distribution on the higher frequencies, which changes slightly over time and overall resembles a Rayleigh distribution, indicates an influence by the local wind shear (Ochi, 1998). It can be seen, that the energy of the long travelling swell is far higher than the one of the local wind swell. The significant wave height is rather low, while the peak period is quite long. The wave type, that can be seen in this data are therefore waves of long wavelength and low wave height, probably resembling linear wave profiles, caused by the long travelling swell, with small ripples and wavelets disturbing the water surface, which are caused by the local wind.

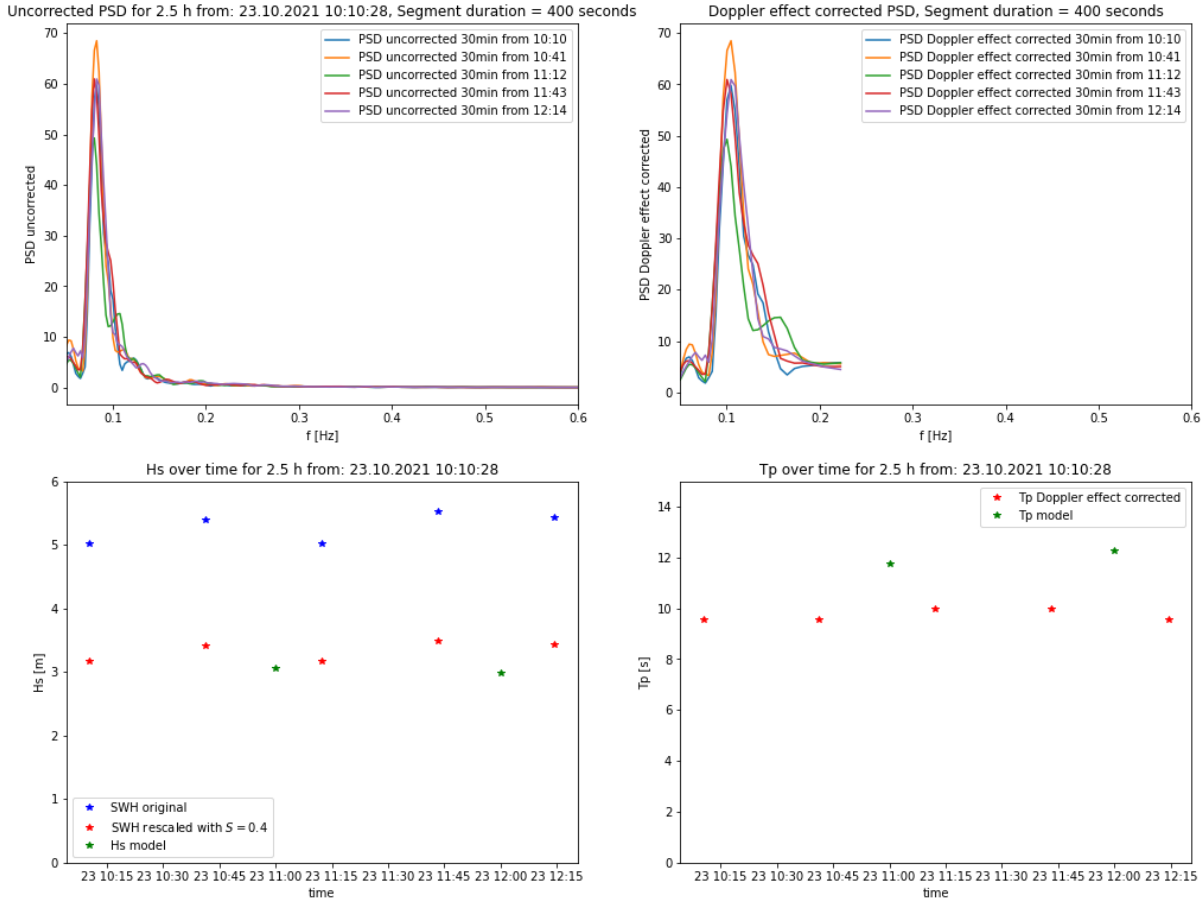

Figure 5.21: Wave properties over 2.5 hours from 23.10.2021 10:10 computed from single 30 *min* data files: *Top left:* Uncorrected PSDs *Top right:* Doppler Effect corrected PSDs *Bottom left:* measured significant wave height SWH, the rescaling SWH_{scaled}, $S = 0.4$ (section 5.3.2) and the model data significant wave height $H_{s,model}$ *Bottom right*: Doppler Effect corrected peak Period $T_{p,corrected}$ and peak period from model data $T_{p,model}$.

In figure 5.21, a single distinct peak can be seen in the wave spectrum, even though it is distributed over a wider range of frequencies than in figure 5.20, especially in the Doppler Effect corrected spectrum. Furthermore, the wave energy is higher, which is also shown by the relatively high significant wave heights. The wave period is long as well, but shorter than in the figure 5.20. The wave type, one could assume by this data, are large waves, with wavelengths of medium length compared to their height, resulting in steep peaks. The disturbance on the right side of the PSDs indicates a breaking of the waves (Ochi, 1998), further indicting an influence of the local wind. It might also explain, why the peak in figure 5.21 is wider, than in figure 5.20.

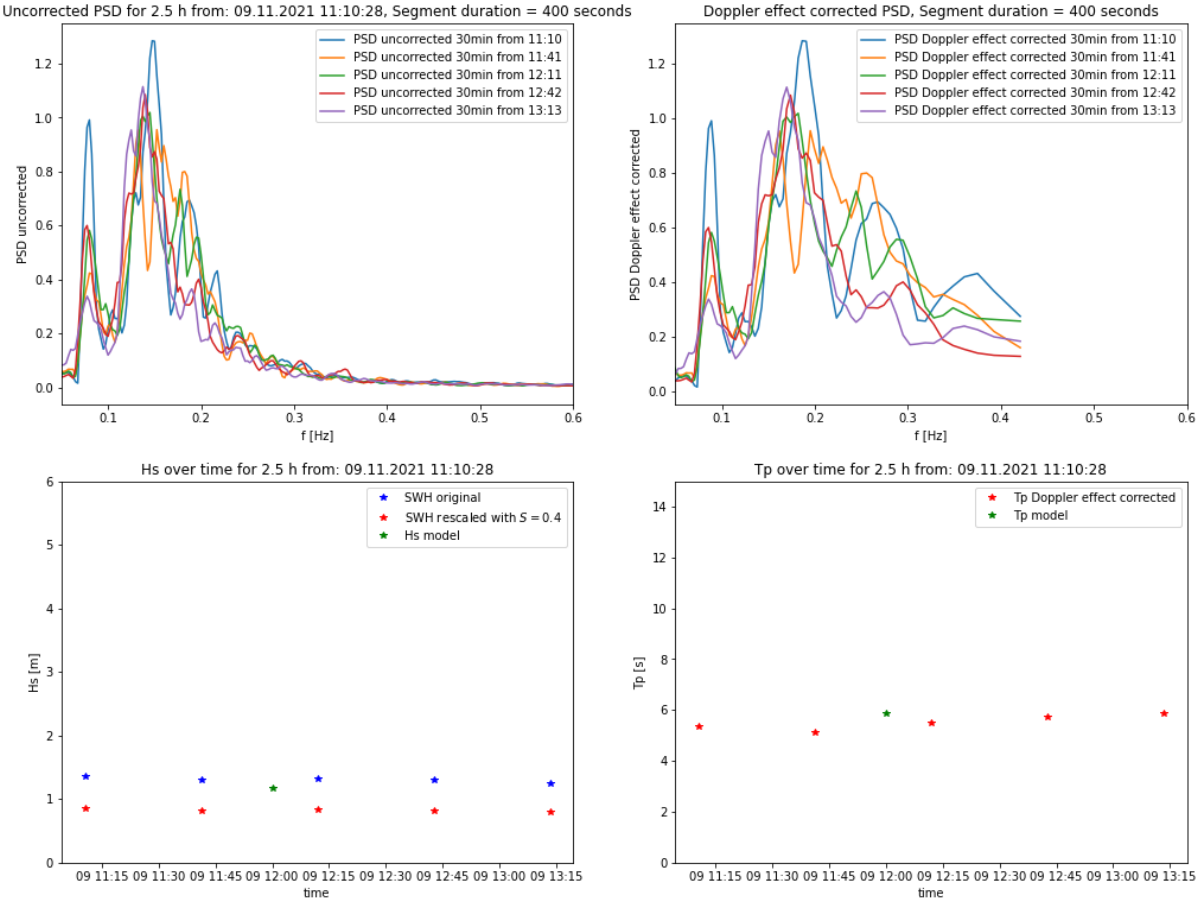

Figure 5.22: Wave properties over 2.5 hours from 09.11.2021 11:10 computed from single 30 *min* data files: *Top left:* Uncorrected PSDs *Top right:* Doppler Effect corrected PSDs *Bottom left:* measured significant wave height SWH, the rescaling SWH_{scaled}, $S = 0.4$ (section 5.3.2) and the model data significant wave height $H_{s,model}$ *Bottom right*: Doppler Effect corrected peak Period $T_{p,corrected}$ and peak period from model data $T_{p,model}$.

The spectrum in figure 5.22 shows two peaks. The peak on the lower frequencies is distinct, but has less energy, than the chaotic distribution on the higher frequencies. The waves depicted here might mainly be influenced, by the local wind, which creates the waves, and results in the chaotic distribution over the higher frequencies in the wave spectrum, while a latent swell is present, but with far less energy. The low energy of the swell is not only shown in the low height of the distinct peak in the PSD, but also in the low significant wave height. Due to the high influence of the local wind on the created waves, the peak periods of the waves are quite short, as the maximum of the PSD is found in the wind induced region.

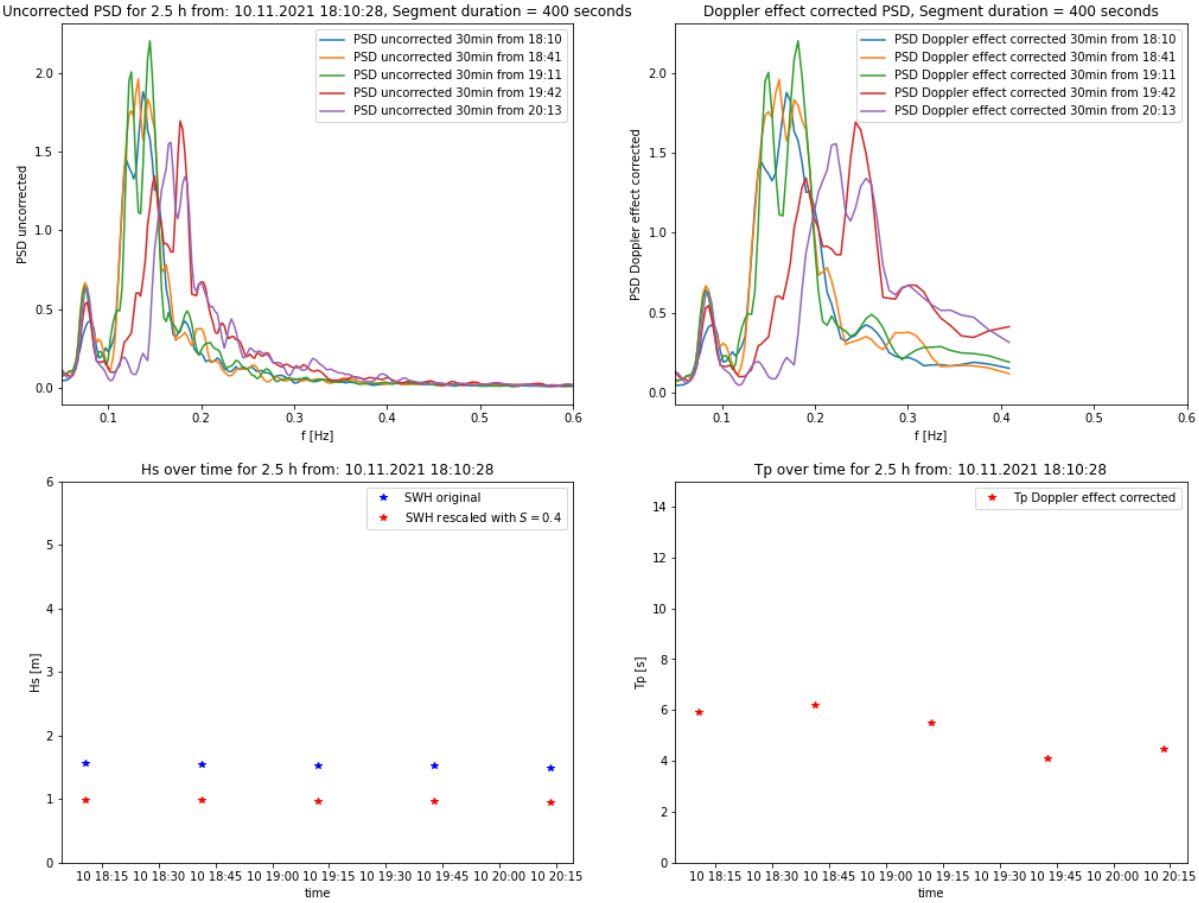

Figure 5.23: Wave properties from 10.11.2021 18:10 computed from single 30 *min* data files: *Top left:* Uncorrected PSDs *Top right:* Doppler Effect corrected PSDs *Bottom left:* measured significant wave height SWH and the rescaling SWH_{scaled}, $S = 0.4$ (section 5.3.2) *Bottom right*: Doppler Effect corrected peak Period $T_{p,corrected}$. Model data is not available for the depicted time interval.

Figure 5.23 shows a situation similar to figure 5.22, but with even more energy from the local wind and almost no influence by the swell. The wind could therefore be assumed to be generally stronger in figure 5.23 than in figure 5.22, resulting in slightly higher significant wave heights. The major changes in the peak period over time indicate a change in the wind conditions, as the wind sheer is the main driving force of the wave spectrum. This shift over time can be also seen in the PSDs.

5.5 Inspecting the Data for Freak Wave Occurrences

The data collected since the start of the One Ocean Expedition on the 20.08.2021 in Arendal is examined for possible occurrences of freak waves. Freak waves are waves that stand out of the wave spectrum, by being at least twice as high as the significant wave height.

$$H_{freak} \geq 2 \cdot H_{1/3} \approx 2 \cdot SWH \tag{5.6}$$

The main concern for the practical realisation of the search for freak waves in the measured data, are outliers. It shows that these often occur in a narrow time interval (figure 5.24).

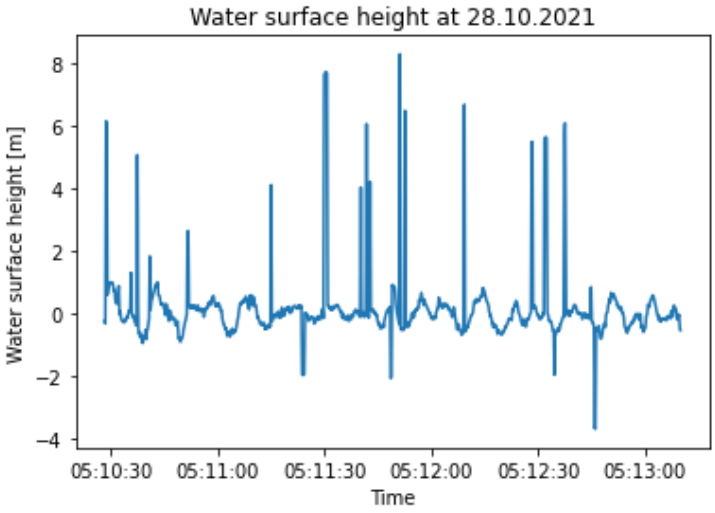

Figure 5.24: Water surface elevation signal of outliers, which have been mistaken for freak waves.

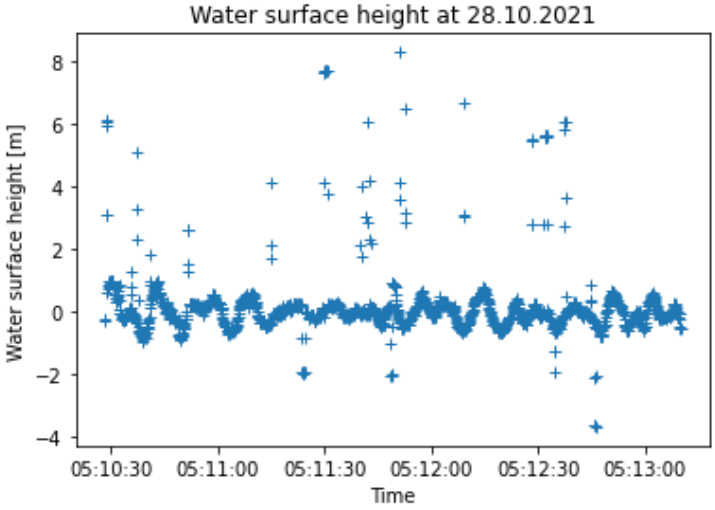

Figure 5.25: Water surface elevation data points of outliers, which have been mistaken for freak waves.

The peaks shown in figure 5.24 and 5.25 are falsely identified as freak waves by the custom made searching algorithm, as the water surface elevation is higher than twice the significant wave height. They can be easily identified as outliers as they only consist of an insignificant number of points in each peak. They are excluded by an adapted searching algorithm, that demands multiple adjacent data points, to be over a certain height. Even with outlier filtering, peaks found by the algorithm are arguable regarding their origin in waves.

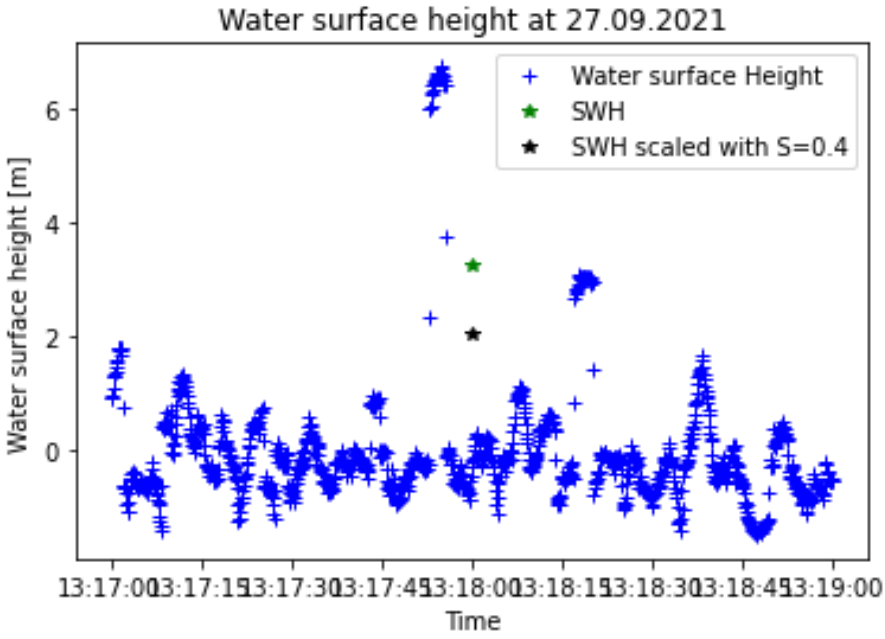

Figure 5.26: Possible freak wave recorded on 27.09.2021, water surface elevation data points compared to the significant wave height SWH and $SWH_{scaled}, S = 0.4$ (section 5.3.2).

The peak shown in figure 5.26 is exemplary for its kind. With the searching algorithm filtering out single outliers, several peaks of this form and amplitude can be found in the data set. They can not be regarded as random outliers as they consist of a significant number of data points and show the same shape as a wave. Nonetheless their short duration and, especially, the lack of data points on the ascending and descending sides raise doubts regarding their authenticity. For further investigation, the predominant signals contributing to the water surface elevation signal shall be looked upon. These are the vertical position of the sensor z and the distance measured by it.

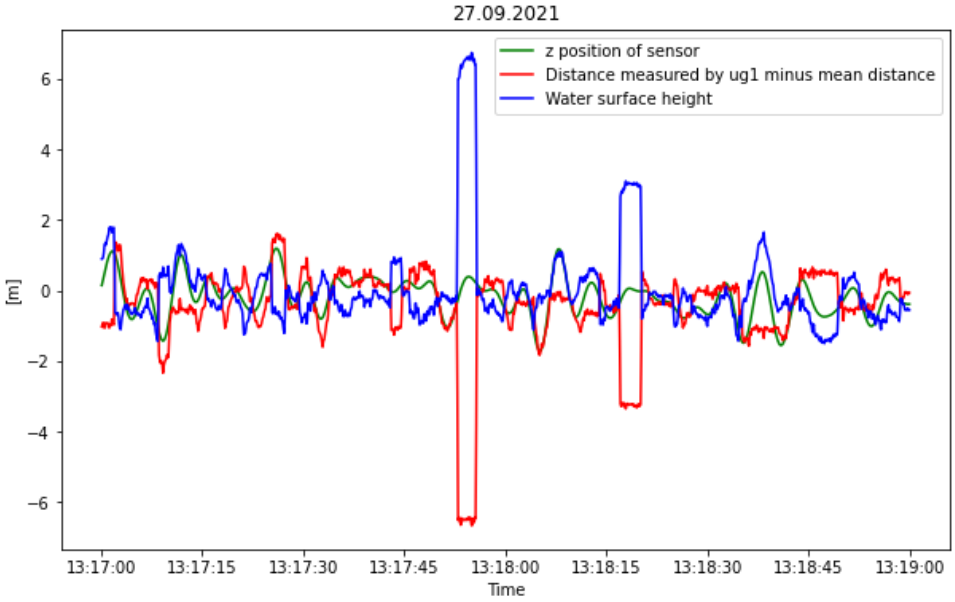

Figure 5.27: Possible freak wave recorded on 27.09.2021, signals contributing to the water surface elevation.

Figure 5.27 shows, that the distance measured by the ultrasonic gauge is the major cause of the peak in the water surface elevation. The sudden drop in the measured distance looks rather strange as it is contrary to the residual pattern in the signal. Furthermore, a relationship between the vertical position of

the sensor and the measured distance can be seen for the rest of the signal, which does not fit with the sudden drop.
It shows that all of the peaks identified by the custom made searching algorithm as freak waves, result from drops in the measured distance, similar to the one in figure 5.27. For all these peaks, the missing interaction between the peak and the vertical position of the ultrasonic probe raises doubt regarding their authenticity. Possible other explanations for these drops in the measured distance, would be objects passing under the ultrasonic sensor, like birds or flying fish.

By coincidence one wave is found in the data, which does not fully meet the definition of a freak wave, as it is defined by equation 5.6, but resembles something close to a freak wave, by its wave height being far higher, than the waves a few minutes before and after (figure 5.28).

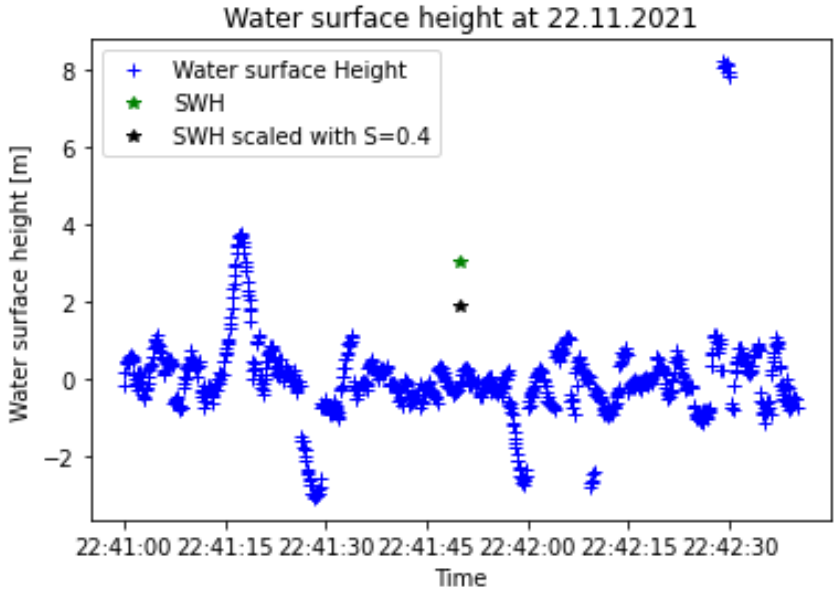

Figure 5.28: Freak-wave-like wave recorded on 22.11.2021, water surface elevation data points compared to the significant wave height SWH and $SWH_{scaled}, S = 0.4$ (section 5.3.2).

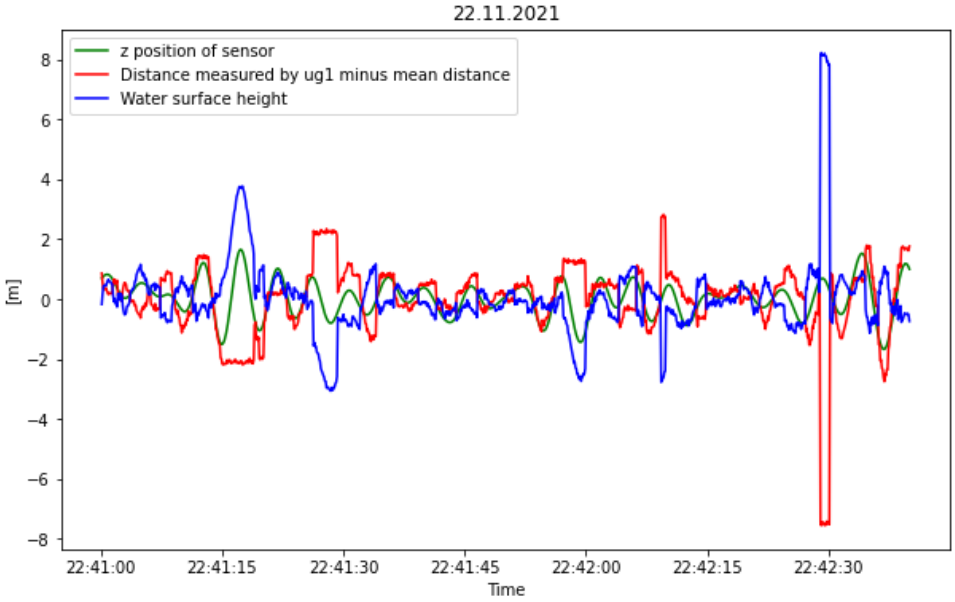

Figure 5.29: Freak-wave-like wave recorded on 22.11.2021, signals contributing to the water surface elevation.

The peak found by the algorithm can be seen on the right hand side of figure 5.29 and 5.28. Again this peak looks strange, regarding the sudden drop in the measured distance. The wave on the left hand side of figure 5.28 however results from a measured signal, that does not seem unrealistic. Its water surface elevation peak and trough are exceptional considering the significant wave height. The wave would count as a freak wave, if its wave height would be from the peak to the shortly following low trough. However as the wave height H_{wave} has been defined by upward zero-crossings in section 4.2.3, the high peak and the trough do not count as the same wave.
This example shows though, that with a searching algorithm tuned to outlier filtration, passing freak waves could be found in the data measured by the system. However, found peaks must be evaluated manually , which is non-problematic, as the with a good filtration only 4 to 5 peaks are found in a data set of over three month.

CHAPTER 6

Discussion

The goal of the project was to develop, build and test a cheap and reliable system for measuring the waves as a water surface elevation time series. Therefore, multiple sensors and IMUs of different price classes were used. The processing unit consisting of the Raspberry Pi and the Arduino Board proved to be reliable and durable, even in the case of other system components failing. Regarding the low cost of these components, it can be said that the main processing unit matched its requirements to the fullest.
All the altimeters used, the two ultrasonic gauges and the radar probe, performed flawlessly. As no major advantage of the radar probe over the ultrasonic gauges could be seen (figure 5.4), it is arguable, whether one probe can be recommended over the other. At least in the case of this specific system, the radar probe cost way more than the ultrasonic gauges. It must be noted though that, the system was set to operate at the maximal frequency of the ultrasonic gauges at 10 Hz (section 2.2.1). A system solely using a radar probe could operate at a far higher frequency which could be beneficial regarding the resolution of the measurements. Prices for parts vary depending on the distributor and individual market situation, which is why no explicit prices shall be named. The general price comparisons, as they were the case for this project, shall be noted nonetheless, to give an orientation.
Regarding the IMUs, the VN100 cost significantly more, than both extra IMUs combined. However, it follows from figure 4.15 and figure 5.10 that the recordings made by the extra IMUs are subject to more errors, than the VN100's, especially when the intensity of motion is high and the IMUs role is the most crucial. Therefore, the choice of an expensive high quality IMU, like the VN100, is highly advisable.
Regarding the positioning of the IMUs, it follows from figure 5.10, that the IMUs should be positioned as close to the probes as possible, as the distance between IMU and probe has turned out to be a significant error source. The installation problems of the extra IMU 1 and its final destruction caused by severe weather shows, that positioning the IMUs close to the probes can represent a major challenge. However, the durability of the altimeter probes shows, that even in these exposed positions, reliability can be achieved by sturdy casing and mounting.
The question of the best position for the altimeter probes cannot be answered clearly. On one hand, the peak period measured by the altimeters on the starboard bow shows falsification by the influence of the ship's hull, depending on the angle of the incoming waves (see figure 5.6). This results in temporal discrepancies in the peak periods, measured by the ultrasonic probe 1 at the bowsprit and ultrasonic probe 2 at the bow (see figure 5.5). On the other hand, the significant wave heights gained from the altimeters on the starboard bow show assumingly better quality than the ones gained from the ultrasonic probe 1 at the bowsprit tip. A narrower scatter and better agreement with the satellite and model data, when scaled (figure 5.15), or computed with the probe position measured by extra IMU 0 (figure 5.10), can be seen. This is most likely the case because the ultrasonic probe 1 at the bowsprit is subject to more motion, than the probes on the starboard side of the bow. The optimal positions for altimeter probes onboard Statsraad Lehmkuhl are assumed to be further back on the bowsprit, where the waves passing under the sensor cannot interact with the ship's hull, but the magnitude of motion is smaller than on the bowsprit tip.

Regarding the question about the realisability of the installation and operation of a wave sensor system on board a ship not designed for research purposes, it can be concluded, that the project was a success. With three altimeters and tree IMUs installed and the processing unit running flawlessly it is shown, that altimeter based wave measurements on board a non-research ship can be realised cheaply by a small team.
Concerning the reliability and durability of the system in various sailing conditions, lessons were learned from the destruction of extra IMU 1 and the durability of the ultrasonic probe 1 in the same position. It shows, that reliability can be achieved and the systems components can be designed to withstand severe

weather conditions. As the extra IMU 1 was from the beginning on only meant to survive temporarily, its destruction in the mentioned cyclone cannot be regarded as a failure itself.

The post processing showed, that the exact orientation of the IMUs in a horizontal plane, and the alignment of the IMUs x-axes with midships is not important. Both the horizontal tilt and the orientation of the IMUs can be gained from the data measured by the IMUs without problem.
The emulation of the IMUs' relative position from the VN100's data and a fitted function proved to be impractical. Neither can the geometrical distances be gained in section 4.1.5, nor can a function be found, that serves the emulation perfectly in section 4.1.5. The best fits are approximations, which give a good equivalent to the position measured by the extra IMU itself most of the time (figure 4.13), but due to the direct impact of the time series of the sensors position on the water surface elevation signal η in equation (4.40), a simple approximation of the sensors position is a relevant possible error source. Another cause for not finding an exact relationship between the VN100 and the extra IMUs could be the precision of the extra IMUs. In total, post processing cannot account for the motion of the altimeter probes in this system, with a satisfactory accuracy.
The calculation of the water surface elevation signal, as well as the significant wave height and the wave spectrum pose no challenge in the post processing. All three definitions of the significant wave height $H_{1/3}$, SWH and H_s can be easily gained from the data. The wave spectra computed from the measured data are assumed reasonable, as well as the different types of mean wave periods based on them. If data for the ship's speed and angle to the waves is accessible, the entire wave spectra can be successfully corrected for the influence of the Doppler Effect on the measured data.

Regarding the quality of the gained parameters, two major conclusions can be made. Firstly, the system overestimates the significant wave height SWH in comparison to model and satellite data, relatively to the wave height (figure 5.1). Though both model and satellite data have uncertainties, they agree during the periods with available satellite data and are thus assumed to be suitable as reference. The overestimation of the significant wave height SWH is present in the data of all probes (figure 5.4) and can be determined as approximately $\frac{1}{\sqrt{0.4}} \approx 1.58$ of the actual significant wave height (figure 5.13, 5.15). It can be found that the overestimation is neither related to the wave period nor the direction of the incoming waves, but stands in direct relation to the magnitude of the probe's motion (section 5.3.1). It can therefore be concluded, that a more precise measurement of the probes' motion could significantly improve the computed significant wave height. It seems that the measurement of the ship's motion directly at the probes, leads to significant wave heights without the general overestimation (figure 5.10). But as the extra IMUs used in this wave sensor system are not precise enough (figure 4.15), a huge random error is found for higher waves (figure 5.10). Therefore, usage of the extra IMUs data does not pose a considerable alternative, as it is more promising to scale the significant wave height computed from the VN100's data accordingly, than to imply an unknown random error. The findings regarding the importance of the IMU positioning are therefore more relevant for future projects, than for the data measured by this wave sensor system.
The second major observation, is that the Doppler Effect must be compensated to gain a realistic peak period (figure 5.3). Although the measured peak period cannot be validated directly, as other measured data is not available, it is found that the uncorrected peak period shows an unrealistic behaviour, by remaining constant over longer time periods at distinct values. The Doppler Effect corrected peak period, however, was found to be reasonable and, in addition, follows the same trend as simulated by model data. This implies, that the measured wave spectra must also be corrected for the Doppler Effect, in order to resemble the spectra of the actual waves. Generally, the spectra appear reasonable, as they resemble the shapes typical for open ocean waves and show peaks where they would be expected (section 5.4). From the importance of the Doppler Effect for the computation of the real wave spectra follows a need for precise data regarding the ship's velocity and direction to the incoming waves. It can be seen, that only the data measured by the ultrasonic probe 1 at the bowsprit can be used for analysis of the wave spectra, as the peak periods gained from the probes at the bow seem to be falsified, by the influence of the ship's hull, when the waves come from astern (figure 5.5, 5.6).

Regarding the usability of the data measured by the system, section 5.4 shows, that the spectra gained from the measured data allow a profound analysis of the underlying swells. From section 5.5 can be concluded, that the data measured by the system is suited for the search for freak waves, under the condition, that outliers are filtered and the searching algorithm is fine tuned for the rare occurrence of artifacts, which have been caused by other things than waves, like objects passing under the sensor.

Concerning the overestimation of the significant wave height, it generally seems to be correctable by scaling and thus can be used for further analysis. However, the modification of the data by scaling should be kept in in mind, when comparing with data from other sources. Also further investigation of the scaling coefficient impact, with new data accessible from the wave sensor, system should be considered.

The aspects learned about the wave sensor system give great potential for further improvement. An optimisation regarding the motion measurement is needed. Therefore, IMUs of high quality should be mounted directly at the altimeter probe locations in future systems. The design of sturdy and waterproof casings and mounts for the IMUs are the most crucial key-point for the realisation of this improvement. Regarding the altimeter placing, the direction of the incoming waves and the resulting effects of the ship's hull must be considered. At a large sailing ship like the Statsraad Lehmkuhl, the bowsprit gives mounting options with undisturbed waves, however this is no possibility for non-sailing ship types. Alternative mounting constructions, serving the same effect as the bowsprit could be considered. Alternatively, several altimeters could be positioned around the hull, or the altimeters could be angled to move the measurement point further away from the ship's hull. However, the later could proof challenging, regarding the reflection of the emitted signals.
A further need for improvement lies in the measurement of ship speed, heading and the wave direction for the Doppler Effect correction. While the ship's speed and heading can be read from the ship's system and stored together with the other measured values, the measurement of the wave direction poses a challenge to the design of an improved wave sensor system to be mounted on ships.

CHAPTER 7

Conclusion

The concept of a ship borne wave sensor systems based on altimeters and motion correction, brought up by Christensen et al. (2013), is a practical and comparably cheap method for the measurement of ocean waves. The design and production of custom wave sensor systems is realisable with small funds and a small team.
Attention must be payed to the placing of the altimeters to avoid falsifications of the wave spectra by the ship hull. The inertial measurement units (IMUs) should always be placed as close to the altimeter probes as possible. The quality of the IMUs is hereby crucial for the precision of the system. Sensor placement at exposed locations for less influence of the ship's body must not be feared, as the design of casings and mounts able to withstand harsh weather conditions is of less difficulty, than the correction of effects caused by non-ideal altimeter or IMU positions during post processing.
It must be considered, that corrections for nonalignment of the IMU with midships, or a tilt of the IMU, rely on a significant amount of data measured by the IMU. Therefore post processing is best advisable to start, after enough data for this analysis is available. Once the spatial orientation of the IMU has been determined, further data can be evaluated on the run.
A correction for the Doppler Effect, caused by the ships speed through the water, must be performed for the spectra computed from the measured data. Therefore, the ship's velocity and the angle of the waves to midships are needed. These values should therefore be recorded and saved together with the measurements of the altimeters and IMUs.
The wave spectra obtained from the systems measurements are of good quality and allow not only the computation of different types of wave periods, but also give insight on the particular swell types present. The significant wave height computed from the systems measurement shows a relative overestimation of approximately 1.58 times the actual significant wave height. This phenomenon can be traced back to an unsatisfactory precision in the correction for the motion of the altimeter probe, based on the IMU measurements. The overestimation can be compensated by scaling, to a certain degree.
In sum, the ship mounted wave sensor system based, on altimeters and IMUs, proves to be a good alternative to the usual wave sensor buoys and shows great potential for application and further development.

Bibliography

Saleh Abdalla, Salvatore Dinardo, Jérôme Benveniste, and Peter Janssen. Assessment of CryoSat-2 SAR mode wind and wave data. *Advances in Space Research*, 62, 02 2018. doi:10.1016/j.asr.2018.01.044.

Adafruit. Adafruit ISM330DHCX + LIS3MDL FeatherWing - High Precision 9-DoF IMU Product Website, 2022. URL https://www.adafruit.com/product/4569. Accessed: 2022-04-04.

APG. *True Echo TM Pulse Radar Level Transmitter User Manual: Series PRL for Liquids and Series PRS for Solids*. Automation Products Group, Inc., 1025 W 1700 N Logan, UT 84321, United States of America, January 2019a. URL https://www.apgsensors.com/sites/default/files/manuals/PRL-PRS-manual.pdf.

APG. *IRU Series Ultrasonic Sensors User Manual: IRU-2000's, IRU-3430's, IRU-5000's, IRU-6420's, IRU-9420's*. 1025 W 1700 N Logan, UT 84321, United States of America, April 2019b. URL https://www.apgsensors.com/sites/default/files/manuals/IRU-manual.pdf.

Arduino. Arduino Due Product Website, 2022. URL https://www.arduino.cc/en/Main/arduinoBoardDue. Accessed: 2022-04-04.

Jean-Raymond Bidlot. *Ocean wave model output parameters*. ECMWF, jean.bidlot@ecmwf.int, June 2016. URL https://confluence.ecmwf.int/download/attachments/59774192/wave_parameters.pdf?version=1.

Jean-Raymond Bidlot, Damian J. Holmes, Paul A. Wittmann, Roop Lalbeharry, and Hsuan S. Chen. Intercomparison of the Performance of Operational Ocean Wave Forecasting Systems with Buoy Data. *Weather and Forecasting*, 17(2):287 – 310, 2002. doi:10.1175/1520-0434(2002)017<0287:IOTPOO>2.0.CO;2. URL https://journals.ametsoc.org/view/journals/wefo/17/2/1520-0434_2002_017_0287_iotpoo_2_0_co_2.xml.

Ana Carrasco and Yvonne Gusdal. Validation of the operational wave model WAM for the years 2012 and 2013. Technical Report 21/2014, Norwegian Meteorological Institute, 2014. URL https://www.met.no/publikasjoner/met-report/met-report-2014/_/attachment/download/3f47d6ea-43ab-4271-a1e9-9a55653940d9:206f28dd030756e10717d4967b456ca7ce86762b/MET-report-21-2014.pdf.

Kai Christensen, Johannes Röhrs, Brian Ward, Ilker Fer, Göran Broström, Øyvind Saetra, and Oyvind Breivik. Surface wave measurements using ship mounted ultrasonic altimeter. *Methods in Oceanography*, 6:1–15, July 2013. doi:10.1016/j.mio.2013.07.002.

ECMWF. *IFS Documentation CY43R1 - Part VII: ECMWF Wave Model*. Number 7 in IFS Documentation. ECMWF, 2016. doi:10.21957/18mel2ooj. URL https://www.ecmwf.int/node/17120.

ESA. Cryosat Mission Background, 2022a. URL https://earth.esa.int/eogateway/missions/cryosat/description. Accessed: 2022-04-25.

ESA. Sentinel-3 Altimetry User Guide, 2022b. URL https://sentinels.copernicus.eu/web/sentinel/user-guides/sentinel-3-altimetry. Accessed: 2022-04-25.

ESA. Sentinel-3 Geophysical Measurements, 2022c. URL https://sentinels.copernicus.eu/web/sentinel/user-guides/sentinel-3-altimetry/overview/geophysical-measurements. Accessed: 2022-04-25.

ESA. Sentinel-3 Resolution Cells, 2022d. URL https://sentinels.copernicus.eu/web/sentinel/user-guides/sentinel-3-altimetry/resolutions/resolution-cells. Accessed: 2022-04-25.

Yvonne Gusdal and Ana Carrasco. Validation of the Operational Wave Models - Report 2011. Technical Report 21/2012, Norwegian Meteorological Institute, December 2012. URL https://www.met.no/publikasjoner/met-report/met-report-2012/_/attachment/download/c7812738-6ff7-42cb-9304-16e8b71f66db:9258ba17832f5e235c0c7ea873592e3a2f4e21d7/MET-report-23-2012.pdf. ISSN: 1503-8025.

Yvonne Gusdal, Ana Carrasco, Birgitte R. Furevik, Øyvind, and Sætra. Validation of the Operational Wave Model WAM at met.no - Report 2010. Technical Report 14/2011, December 2011. URL https://www.met.no/publikasjoner/met-report/met-report-2011/_/attachment/download/177aecbe-cca1-41a0-846d-12944024bfd0:8f0da00ff7f91bb97a1bf22574c4670ebdc635d5/MET-report-14-2011.pdf. ISSN: 1503-8025.

Leo H. Holthuijsen. *Waves in Oceanic and Coastal Waters*. Cambridge University Press, 2007. doi:10.1017/CBO9780511618536.

U. Mahesh Kumar, D. Swain, S.K. Sasamal, N. Narendra Reddy, and T. Ramanjappa. Validation of SARAL/AltiKa significant wave height and wind speed observations over the North Indian Ocean. *Journal of Atmospheric and Solar-Terrestrial Physics*, 135:174–180, 2015. ISSN 1364-6826. doi:https://doi.org/10.1016/j.jastp.2015.11.003. URL https://www.sciencedirect.com/science/article/pii/S1364682615300869.

Xinba Li, Panagiotis Mitsopoulos, Yue Yin, and Malaquias Peña. SARAL-AltiKa Wind and Significant Wave Height for Offshore Wind Energy Applications in the New England Region. *Remote Sensing*, 13 (1), 2021. ISSN 2072-4292. URL https://www.mdpi.com/2072-4292/13/1/57.

Trygve Løken, Jean Rabault, Atle Jensen, Graig Sutherland, Kai Christensen, and Malte Müller. Wave measurements from ship mounted sensors in the Arctic marginal ice zone. *Cold Regions Science and Technology*, 182:103207, February 2021. doi:10.1016/j.coldregions.2020.103207.

J. N Newman. *Marine Hydrodynamics*. The MIT Press, Cambridge, 2018. ISBN 0-262-53482-7.

NOAA. Jason Significant Wave Height Quick Guide, 2022. URL https://cimss.ssec.wisc.edu/goes/OCLOFactSheetPDFs/JPSS_QuickGuide_JasonSignificantWaveHeight.pdf. Accessed: 2022-04-25.

NORCE. One Ocen Data Exploration Portal by Norce, 2022. URL https://oneocean.web.norce.cloud. Accessed: 2022-04-21.

Michel K Ochi. *Ocean Waves: The Stochastic Approach*. 1998. ISBN 9780521563789.

One-Ocean-Expedition-website. One Ocean Expedition Website, 2022. URL https://oneoceanexpedition.com/one-ocean-expedition-circumnavigation-statsraad-lehmkuhl. Accessed: 2022-05-06.

S. Ponce de León and C. Guedes Soares. Distribution of winter wave spectral peaks in the seas around Norway. *Ocean Engineering*, 50:63–71, 2012. ISSN 0029-8018. doi:https://doi.org/10.1016/j.oceaneng.2012.05.005. URL https://www.sciencedirect.com/science/article/pii/S0029801812001667.

Raspberry-Pi. *Raspberry Pi 4 Computer: Model B*. Raspberry Pi Trading Ltd, Maurice Wilkes Building, Cowley Rd, Cambridge CB4 0DS, United Kingdom, January 2021. URL https://datasheets.raspberrypi.com/rpi4/raspberry-pi-4-product-brief.pdf.

SFE. SparkFun RedBoard Artemis Product Website, 2022. URL https://www.sparkfun.com/products/15444. Accessed: 2022-04-04.

Harold A. Underhill. Training Ship "Grossherzog Friedrich August" (Later "Statsraad Lehmkuhl") - Sail and Rigging Plan and Hull Details, n.d. URL https://www.skipper.co.uk/catalogue/item/training-ship-grossherzog-friedrich-august-later-statsraad-lehmkuhl-sail-and-rigging-plan-and-hull-details. Accessed: 2022-09-08.

VectorNav. *VN-100 User Manual*. VectorNav Technologies, 10501 Markison Road Dallas, Texas 75238, United States of America, 2017. URL https://usermanual.wiki/Pdf/vn100usermanualum001.1739962267/html. Document Revision 2.23.

VectorNav. VectorNav VN100 Product Website, 2022. URL https://www.vectornav.com/products/detail/vn-100. Accessed: 2022-03-31.

J. K. Wang, L. Aouf, A. Dalphinet, Y. G. Zhang, Y. Xu, D. Hauser, and J. Q. Liu. The Wide Swath Significant Wave Height: An Innovative Reconstruction of Significant Wave Heights From CFOSAT's SWIM and Scatterometer Using Deep Learning. *Geophysical Research Letters*, 48(6), 2021. doi:https://doi.org/10.1029/2020GL091276. URL https://agupubs.onlinelibrary.wiley.com/doi/abs/10.1029/2020GL091276.

P. Welch. The use of fast fourier transform for the estimation of power spectra: A method based on time averaging over short, modified periodograms. *IEEE Transactions on Audio and Electroacoustics*, 15(2): 70–73, 1967. doi:10.1109/TAU.1967.1161901.

Appendix: Illustrations of the Systems Components

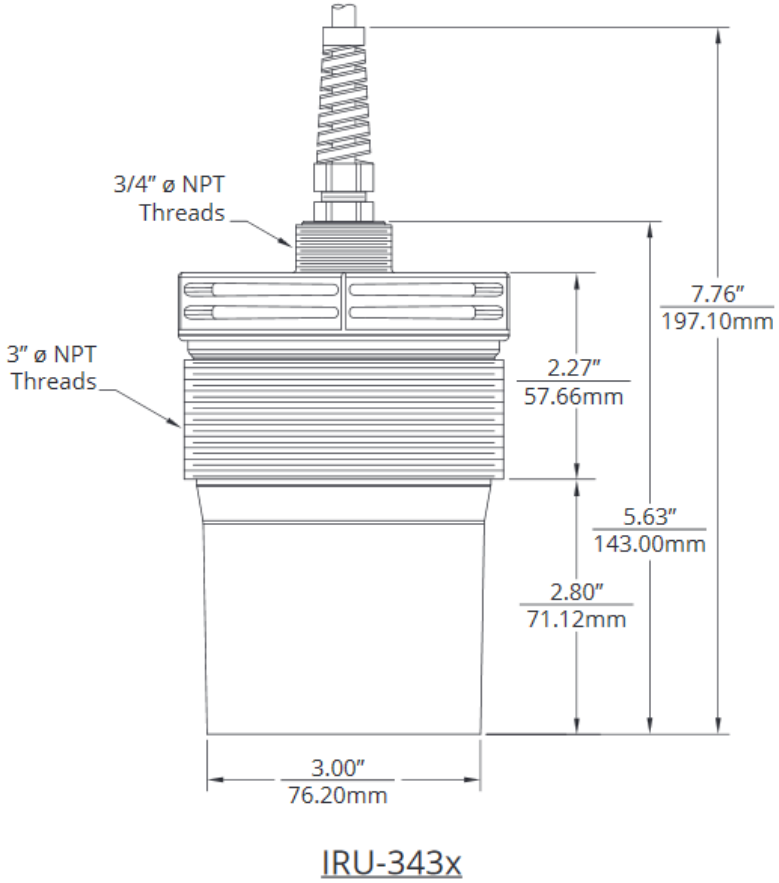

Figure 1: Dimensions of the ultrasonic probes IRU-3433-C60 by Automation Products Group Inc (APG, 2019b).

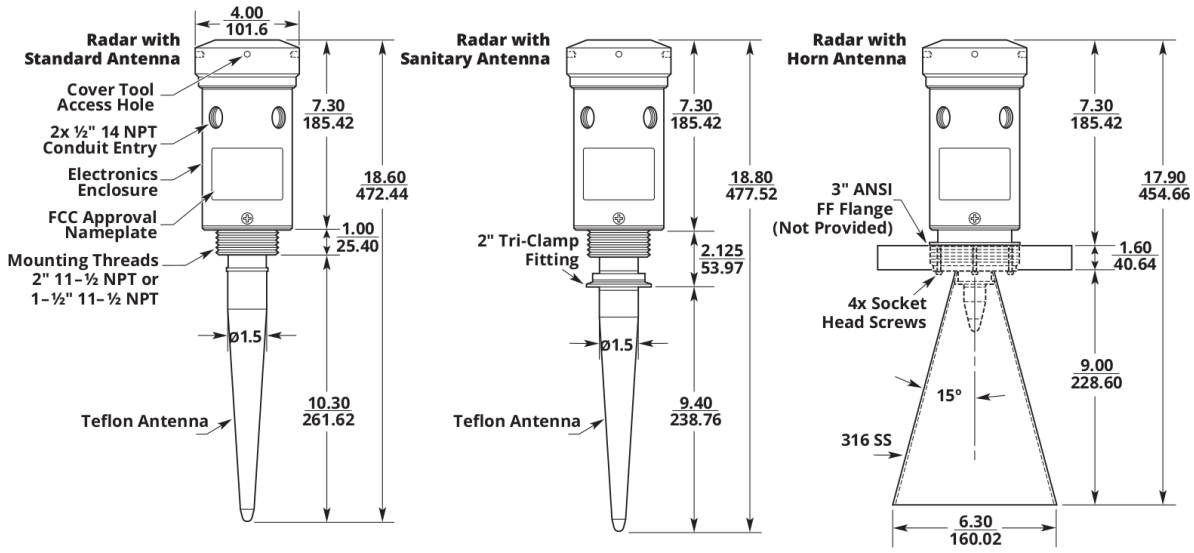

Figure 2: Dimensions of the radar probe with horn antenna RL-050-V024-C4-SS-S6-BF-F by Products Group Inc. (APG, 2019a).

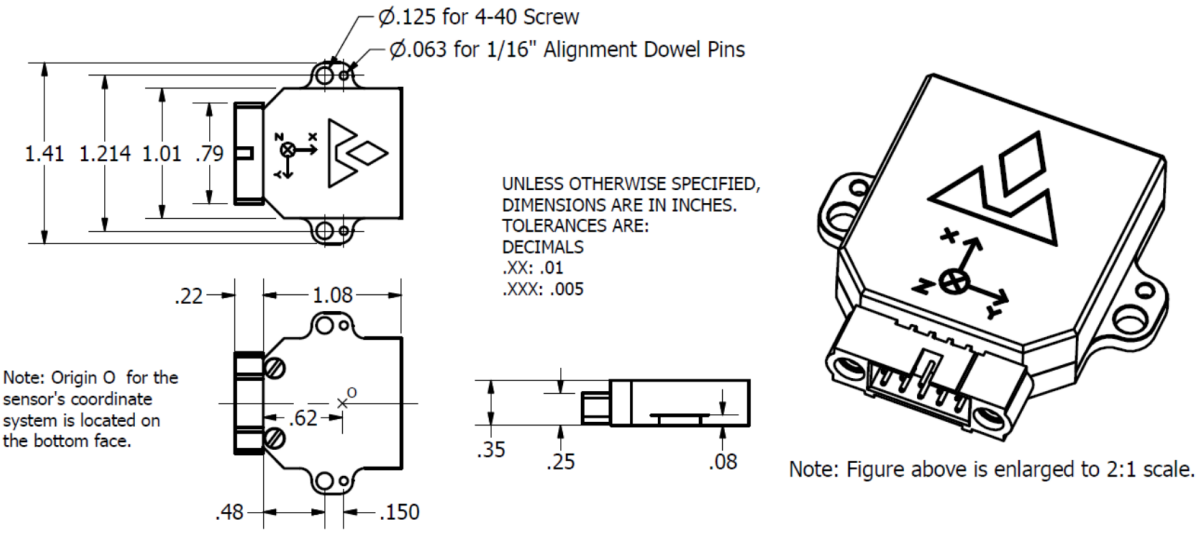

Figure 3: Dimensions of the main IMU VN100 by VectorNav Technologies (VectorNav, 2017).

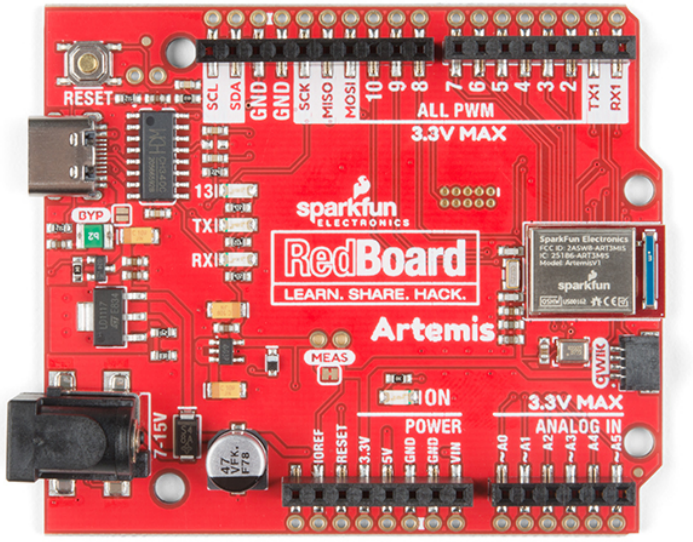

Figure 4: The RedBoard Artemis by SparkFun Electronics (SFE, 2022).

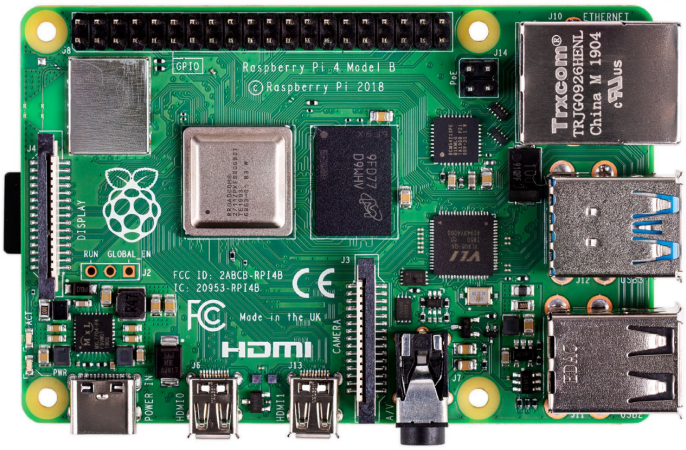

Figure 5: The Raspberry Pi 4 Computer Model B (Raspberry-Pi, 2021).

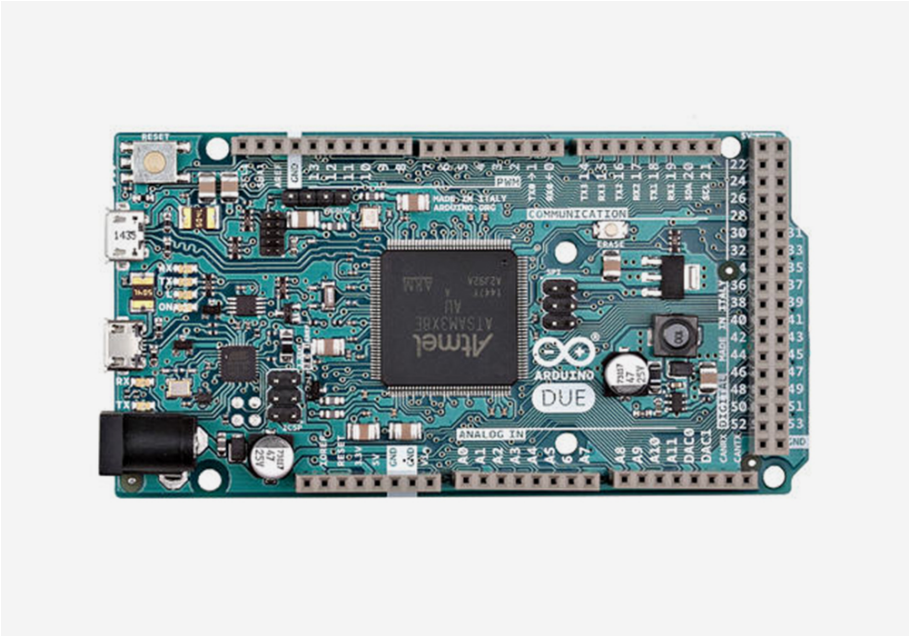

Figure 6: The Arduino Due Board (Arduino, 2022).

Figure 7: The ultrasonic probe 1 mounted under the bowsprit tip.

Figure 8: The radar probe mounted on the starboard side of the bow.

Figure 9: The radar probe mounted on the starboard side of the bow, with the empty slot for ultrasonic probe 2.